STATISTICAL PROPERTIES OF THE SEA SCATTERED RADAR RETURN

Ryan Reed
Department of Electrical and Computer Engineering
Ph.D. Degree, December, 1995

ABSTRACT

To investigate the scattering of microwave radiation from the wind roughened sea a unique ultra wide-band radar system was constructed. The radar was deployed for 6 months during the Yscat94 experiment conducted on Lake Ontario from May to November, 1994. The site was the WAVES research tower operated by the Canada Centre for Inland Waters (CCIW). Over 3500 hours of data were collected at 2, 3.05, 5.3, 10.02, and 14 GHz and at a variety of wind speeds, relative azimuth, and incidence angles.

A simple model based on the current composite model is developed and incorporated into a simulation scheme which is used to evaluate the validity of the composite model in regards to mid-incidence angle microwave scattering. The power distributions are parameterized by fitting log-normal distributions to the empirical histograms and using the log-variance and log-mean to describe the distribution. The results are compared to the predicted parameter values of simulations. It is found that the composite model accurately predicts the qualitative behavior of the radar return for incidence angles between 30 and 50 degrees, but that other scattering mechanisms influence the return at 20 and 60 degrees.

The velocity statistics of the empirical data are calculated and compared to results obtained from the simulation. The simulated data is found to agree with the empirical data for 20-40 degree incidence angles. At higher incidence angles the simulation under-predicts the true velocities. The average cross section velocity profiles generated by the simulation and the relationship between the H-pol and V-pol velocities also agree under most circumstances.

The implication of these results is that the postulated "missing" scatterers (scatterers not included in the composite model) do not contribute significantly to the total radar cross section for incidence angles from 30 to 50 degrees. This indicates that further progress on theoretically based geo-physical model functions must include a deeper understanding of the development of Bragg scattering mechanisms.

STATISTICAL PROPERTIES OF THE SEA SCATTERED RADAR RETURN

A Dissertation
Submitted to the
Department of Electrical and Computer Engineering
Brigham Young University

In Partial Fulfillment
of the Requirements for the Degree
Doctor of Philosophy

by
Ryan Reed
December, 1995

This dissertation by Ryan Reed is accepted in its present form by the Department of Electrical and Computer Engineering of Brigham Young University as satisfying the dissertation requirement for the degree of Doctor of Philosophy.

David G. Long, Committee Chairman

David V. Arnold, Committee Member

Brian Jeffs, Committee Member

Mike Jensen, Committee Member

A. Lee Swidlehurst, Committee Member

Date

Wynn C. Stirling, Graduate Coordinator

Contents

List of Tables

List of Figures

Chapter 1

INTRODUCTION

1.1 Introduction

The mathematical representation of the relationship between the environmental and physical parameters of the air-sea interface and the observed radar cross section is referred to as the geo-physical model function (GMF). The mathematical derivation of this function remains a poorly understood problem in the combined fields of oceanography, fluid dynamics, and electromagnetics. A good understanding of this model function is necessary in order to effectively utilize microwave radars as remote sensing devices to probe the air-sea interface. In particular, the physical mechanisms involved in scattering the microwave radiation must be known in order to interpret the scatterometer data.

Many applications of microwave remote sensing have been demonstrated in the past few decades. One of the most important of these applications is in the field of microwave anemometry. Microwave scatterometry remains the only proven technique for making global oceanic wind measurements. Many experiments in support of this application have been performed utilizing radar observations of the sea surface using synthetic aperture radar (SAR), single and multi-frequency scatterometers, real aperture radar (RAR), and altimeters. Interpreting the data collected in these experiments, and applying them to the spaceborne anemometry problem, relies completely on our understanding of the GMF.

Theory-based models of ocean scattering mechanisms have had very little success in predicting characteristics the radar return. Because of this shortcoming, all spaceborne scatterometers used for wind retrieval have utilized empirical model functions developed using ground truth data to interpret their results (Long, 1994). Since these models are not based on the physical processes involved, their accuracy and precision is difficult to determine.

The recent boom in spaceborne microwave remote sensing projects such as the European Space Agency's Earth Remote Sensing satellites (ERS-1 and ERS-2), Japan's Advanced Earth Observing Satellite (ADEOS), and NASA's Earth Observing System (EOS), underscores the increasing necessity of developing a good GMF. Thus, enhancing our understanding of the processes involved in ocean surface scattering is an important and timely subject of research.

A scatterometer probes the air-sea interface by scattering coherent microwave radiation from the interface and recording the returned signal. Since the return is a very complex function of many unknown variables, it is reasonable to model it as a stochastic process. Each physical process involved in the GMF manifests itself in the radar return by causing fluctuations of the received power and frequency in a way that is characteristic of that process. Therefore, the statistics of the radar return carry information about what physical processes are involved in the scattering.

To date the statistic which has received the most attention has been the mean radar cross section, σ, of the radar return. This is not surprising since it is σ that is the desirable quantity required for most practical applications of space based

scatterometry. However, knowing σ doesn't say much about the scattering process unless one knows the physical mechanisms involved.

Other statistics which can be extracted from the radar return can give much more insight into the scattering process. For example, the mean Doppler shift gives the average velocity of the scatterers involved. Doppler bandwidth gives information about the variety of velocities being observed. This distribution of the observed radar cross section can also give information on what is being observed.

Unfortunately, previous experiments have been limited in either time or operating parameters. To rectify this situation, an ultra-wide band radar system was developed that is capable of collecting the various measurements necessary to properly study the statistics of the sea scattered radar return. This radar was deployed on the Canada Centre for Inland Waters (CCIW) WAVES research platform on Lake Ontario from May through November, 1994. This experiment is known as the Yscat94 experiment.

The results presented here are an analysis of the statistics of the radar return scattered from a wind roughened water surface, based on the Yscat94 data. Both theoretical and empirical results are used to study the relationship between the water's surface and microwave radar.

Current scattering models seem to under-predict the observed radar cross section by 3 dB or more. There seems to be two possible explanations for this phenomena. First, it is possible that the model includes the right scattering mechanisms, just in the wrong way. Second, it is possible that the actual scatter is due to other mechanisms not included in the standard model. Mechanisms which have been proposed include breaking waves, wedge scattering, and microbreaking.

The approach taken here is to look at statistics other than the mean to determine if the composite model describes them valid or if other scattering mechanisms are influencing the return. Both power and velocity distributions are analyzed for signs of additional scatterers.

The general result is that these distributions do not show signs of large contributions from these other scatterers, however small contributions appear to occur for high wind speeds, incidence angles, and frequencies.

Contributions of this research to the current body of knowledge on this topic include:

- Designing and building a unique, wide band radar system capable of operating unattended on a remote site, while collecting data under a variety of environmental and radar parameters
- Developing and conducting a six month long international experiment with CCIW in order to collect a large enough data set to study the radar distributions
- Presenting a simple scattering model which predicts log-normal power distributions
- Outlining a simple simulation technique for comparison with empirical data
- Calculating cross section distributions from empirical data to show development with environmental and radar parameters
- Comparing empirical distributions with various analytical distributions and showing that the log-normal is a good fit

- Parameterizing distributions using log-variance and log-mean to show dependence on environmental conditions and radar parameters
- Presenting a simple model for determining the composite model velocity qualities.
- Computing Doppler distributions from experimental and simulated data
- Presenting and validating a parameterization method for empirical Doppler distributions
- Comparing empirical velocity distributions to model distributions to determine validity of composite model
- Measuring and presenting velocity modulation of the radar return and comparing this to simulation.

The net result of this work is an increased understanding of the mechanisms involved in radar scattering from the sea surface and the validity of the composite model.

The format of the rest of this dissertation is as follows: Chapter Two gives a history and primer on the subject of wind-wave interaction theory and modeling, electro-magnetic scattering, and the current literature on scattering models and mechanisms. Chapter Three describes the Yscat radar and the Yscat94 experiment including instrumentation, environmental conditions, and data collection schemes. Chapter Four discusses the distribution of the measured radar cross section from the point of view of scattering mechanisms and Chapter Five looks and the velocity of the surface scatterers in the same light. Chapter Six summarizes the conclusions and suggests directions for further research.

Chapter 2

BACKGROUND

The study of microwave remote sensing began in the 1960's with the advent of space exploration. The obvious importance and usefulness of being able to make global wind vector measurements has stimulated a great deal of research on the subject. Still, despite over 30 years of intense study, many questions are still outstanding. This chapter is devoted to presenting some previous results which make up the current state–of–the–art in this field. Additional information is provided in succeeding chapters as needed.

The first section is devoted to the behavior of the sea surface in response to the wind. I will first present a qualitative picture of the development of a wind driven wave field. The mathematical formalism and models which have been developed in order to handle the problems of the sea scattered radar return will be outlined. Finally, the EM theory and its application to the main subjects of sea scattering will be presented.

2.1 The Wind–Wave Connection

The air-sea interface is a very complex coupled thermo-dynamical system. It is the boundary between two geophysical fluids and is highly nonlinear where the response of one fluid to the forcing of the other causes a change in the entire system. Studying and modeling this system quickly leads to intractable (although well posed) questions. Although there is still disagreement over what is the exact

form of the response of the surface to the wind, the qualitative response described below is generally accepted.

2.1.1 Qualitative Picture

When the wind begins to blow over a flat, undisturbed water surface, wave growth is initiated by random turbulent eddies in the surface wind (Phillips, 1977). Once wave growth has begun, further growth is dominated by two mechanisms: energy input directly from the wind and nonlinear transfer of energy to different wavelengths via multi-wave mixing processes. The smallest waves (capillary waves) are in dynamic equilibrium with the surface wind. Because of this, they are the first to grow once wind input to the system has been established, and they quickly reach equilibrium (Plant, 1982). The mechanism for equilibrium is the dissipation of energy to other wavelengths through nonlinear interaction.

As energy input to the small waves continues, more and more energy is transfered to other wavelengths and a continuous spectrum of waves begins to grow. At this initial stage of growth, the primary energy dissipation mechanisms are viscous dissipation and surface tension (Donelan and Pierson, 1987). However, these dissipative effects are small compared to the wind input so the energy stored in the surface waves continues to increase. This increase in energy is manifested through the increasing amplitude of the long wavelength swell (gravity waves).

The height of the surface waves continues to grow until the waves become so steep that the structure of the wave becomes unstable and it breaks. This breaking occurs on many scales and once it begins, becomes the dominant means of energy dissipation (Melville, 1991). As energy continues to move into the system, waves continue to grow and wave breaking increases in frequency and vigor. This process

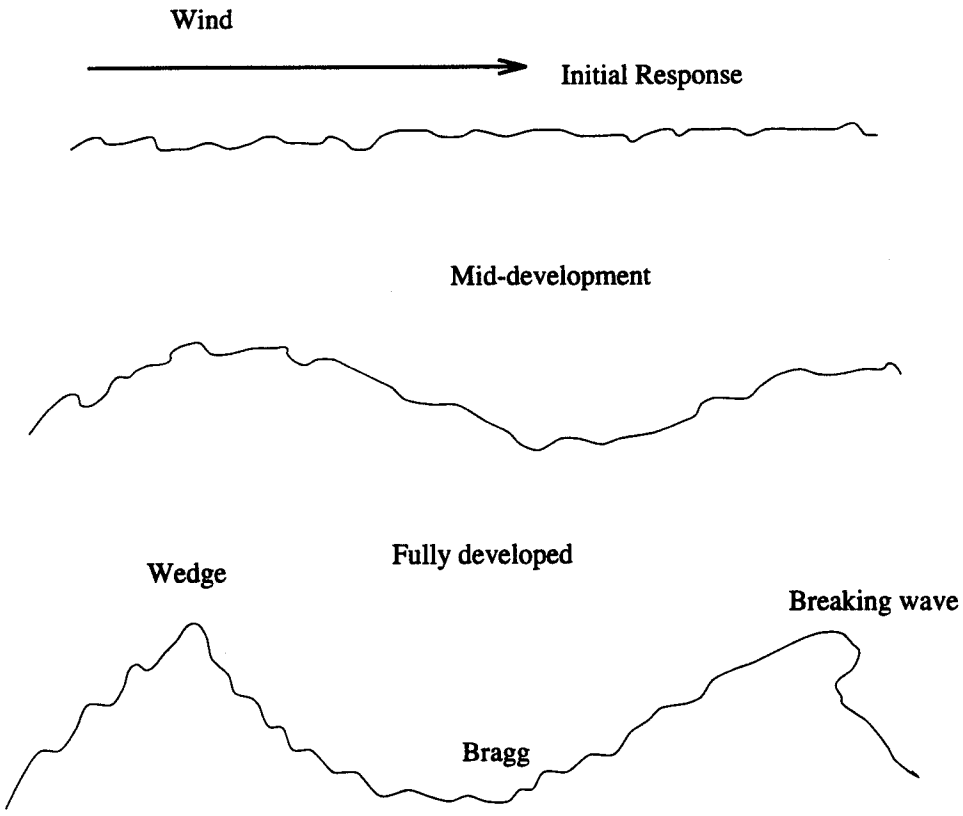

Figure 2.1: Cross section of ocean surface at different stages of growth.

continues until the rate of energy dissipated from the waves by the combined effects of surface tension, viscous dissipation, and wave breaking matches the rate of energy input from the wind and evolution of the surface waves cease. This steady state condition is called a fully developed sea (Phillips, 1977).

2.1.2 Mathematical Models of Wind-Wave Interaction

Although most researchers in the area of ocean wave dynamics would agree with the qualitative description above, they would have differing opinions on what the precise mathematical description of the process should be. There is, however, a formalism used in describing wind driven sea surfaces. This section presents this

formalism and then describes the different mathematical models which are most important to microwave scattering.

Characterization of the Sea Surface

Surface waves are the product of very complex and unpredictable processes. Therefore, it is reasonable to model them as stochastic processes. Naturally then, the language used in describing various aspects of the surface is the language of statistical theory. In order to characterize the system, one generally uses the Fourier transform of the surface displacement autocorrelation as a function of time and space, the "frequency and wave number power spectrum" of the surface. Although it is generally understood the surface is non-Gaussian (the wave slopes tend to be skewed in the upwind direction) and that higher order spectra are need to completely characterize the surface, these spectra are not generally used because of the intractability of the problem. A notable exception is the recent use of an empirical bispectrum model to explain the upwind–downwind asymmetry (Chen et al., 1993). Fortunately, power spectra seem to adequately describe the sea surface under steady state conditions .

The wave field is generally spatially homogeneous and slowly varying when considered over large areas. Therefore, ergodic theory may be applied if the time associated with the measurements is small compared to the rate of evolution. The auto-covariance function, $\rho(\mathbf{r}, t)$, of the surface displacement, z is given by

$$\rho(\mathbf{r}, t) = E\{z(\mathbf{x}, t_0) z(\mathbf{x} + \mathbf{r}, t_0 + t)\} \tag{2.1}$$

where E denotes an expectation. By the Wiener-Kinchin theorem (Proakis et al., 1992), the 3-D power spectrum, $S(\mathbf{k}, \omega)$, of the surface is given by the Fourier transform of the covariance

$$S(\mathbf{k}, \omega) = \frac{1}{(2\pi)^3} \int \int \rho(\mathbf{r}, t) e^{i(\mathbf{k}\cdot\mathbf{x} - \omega t)} d\mathbf{r} dt \tag{2.2}$$

Since the true ocean surface varies in time and space simultaneously, Eq. (2.2) is necessary to completely describe the system. However, measurement of this spectrum is a rather difficult process requiring wave staff arrays and intensive data processing (Donelan et al., 1985). In practice, this is rarely done.

For radar scattering applications, the two dimensional wavenumber spectra can usually be used to give an adequate characterization of the surface since the electromagnetic interaction between the surface and the incident field tend to depend on wave number rather than frequency (Wright, 1966). Therefore, knowledge of the frequency portion of the spectrum is not necessary. The two dimensional wave number spectrum, $\Psi(\mathbf{k})$, is related to the three dimensional spectrum by

$$\Psi(\mathbf{k}) = \int S(\mathbf{k}, \omega) d\omega. \tag{2.3}$$

It can also be derived from the surface correlation function by fixing the time coordinate. If $\rho(\mathbf{r}) = \rho(\mathbf{r}, 0)$ then

$$\Psi(\mathbf{k}) = \frac{1}{(2\pi)^2} \int \rho(\mathbf{r}) e^{i(\mathbf{k}\cdot\mathbf{r})} d\mathbf{k}. \tag{2.4}$$

The ocean spectrum covers such a large range of wavenumbers that the array of sensors necessary to measure it adequately is rather prohibitive. Newer remote sensing techniques such as stereo-photography or laser techniques can be used to measure this spectrum, however, these are still experimental and so are rarely done in connection with large remote sensing experiments.

The easiest and most widely performed measurement of the ocean surface is a time series of the wave height at a fixed point. This allows one to determine the frequency spectrum of the surface. The frequency spectrum, $\Phi(\omega)$, of the surface can be derived from a time series of single point wave height data, $z(t)$, using

$$\Phi(\omega) = \frac{1}{2\pi} \int E z^*(t_0) z(t_0 + t) dt. \tag{2.5}$$

and from Eq. (2.2) by integrating over all wave numbers

$$\Phi(\omega) = \int S(\mathbf{k}, \omega) d\mathbf{k}. \tag{2.6}$$

This spectrum provides useful information about significant wave height and peak frequency, as well as other factors. With estimates of wave direction obtained from other means, the full 3-d power spectrum is sometimes estimated using a dispersion relation although this is generally considered dubious.

All of the above characterizations of the random sea surface have been used in microwave scattering theories. In general, though, the two dimensional wavenumber spectrum, $\Psi(\mathbf{k})$, is most often encountered. Because of this many techniques for measuring $\Psi(\mathbf{k})$ have been tried. Despite this it is still a very difficult measurement to make. For this reason most theoretical scattering models usually rely on a combination of empirical and theoretical mathematical models for the wave height spectrum.

Mathematical Models of $\Psi(\mathbf{k})$

It is generally agreed that interaction of electromagnetic waves with the sea surface depends on wavenumber rather than frequency. Also, if we limit our studies to the simpler case of a fully developed sea, rather than including the poorly understood

developing sea, the wave height spectrum is not a function of time. Therefore, it is sufficient to consider models for $\Psi(\mathbf{k})$.

The general method of dealing with stochastic fluid dynamic problems, such as the wind-sea interaction, is radiative (or Boltzmann) transport theory (Smith and Jensen, 1989). Using the techniques of this field, one can describe the evolution of the ocean spectra by applying certain conservation laws.

In most cases, conservation of energy principles cannot easily be applied to wave spectra problems (Phillips, 1977). In the presence of underlying currents and general flow, the waves can exchange energy with the current severely complicating the energy conservation equations. A more useful approach is to apply conservation of wave action in a reference frame that is moving with any underlying flow. Wave action density spectrum, $N(k)$ is defined by the relation

$$E(k) = N(k)\omega = \rho g \Psi(k). \tag{2.7}$$

Where $E(k)$ is the energy density spectrum, ρ is the density of water, g is the acceleration of gravity, and ω is the intrinsic frequency of the wave.

Using similar arguments to conservation of energy approaches the wave action (or more appropriately action density) is governed by

$$\frac{\partial N(k,x,t)}{\partial t} + \frac{d\mathbf{k}}{dt} \cdot \frac{\partial N(k,x,t)}{\partial \mathbf{k}} + \frac{d\mathbf{x}}{dt} \cdot \frac{\partial N(k,x,t)}{\partial \mathbf{x}} = \frac{1}{\omega_o}(Q_i + Q_{nl} + Q_d). \tag{2.8}$$

The right hand terms represent action input from the wind, nonlinear interaction, and viscous dissipation, respectively.

The exact forms for the input terms, $(Q's)$, of Eq. (2.8) are still the subject of some debate; however, there some accepted theoretical forms that have been used in various models. Energy is transferred to the water from the wind mainly through

frictional forces at the boundary. The shear stress imparted to the water is given by

$$\tau = \rho C_d U^2 \tag{2.9}$$

where τ is the stress, ρ is the density of the air, C_d is a drag coefficient and U is the wind speed. The drag coefficient depends strongly on the surface roughness, the stability of the surface boundary layer, and the topography over which the airflow occurs. The product $\sqrt{C_d U^2}$ is sometimes called the friction velocity and is denoted by u_*. Using the friction velocity allows one to compare measurements taken at different locations which may have different air flow characteristics.

Wave growth due to wind input has been found to follow a relaxation relation given by:

$$Q_i = \beta(\mathbf{k})\Psi(\mathbf{k}). \tag{2.10}$$

where $\beta(\mathbf{k})$ is the growth rate.

The exact form of $\beta(\mathbf{k})$ has been the subject of much study. Fitting empirical data yields the form (Plant, 1982):

$$\frac{\beta}{\omega} = .04\left(\frac{u_*}{c}\right)^2 \cos\phi \tag{2.11}$$

where c is the phase velocity of the wave and u_* is the friction velocity. Other forms of β/ω are in terms of wind speed at a fixed height above the surface or the wind speed at some height depending on wavelength (Donelan and Pierson, 1987).

The nonlinear term, Q_{nl}, is due to the transfer of energy between wavenumbers because of the nonlinear nature of water as a wave medium. The dominant effect of the nonlinearity is four-wave mixing, where the waves involved satisfy the phase matching condition

$$\mathbf{k}_1 + \mathbf{k}_2 = \mathbf{k}_3 + \mathbf{k}_4 \tag{2.12}$$

and a frequency matching condition

$$\omega_1 + \omega_2 = \omega_3 + \omega_4. \tag{2.13}$$

Since the wavenumber spectrum is continuous, the redistribution of energy due to nonlinear mixing propagates through the entire spectrum. In general, this leads to a very complicated system which can generally only be evaluated numerically. In the case of a fully developed sea though, one may assume that the nonlinear dissipation term balances the input from the other terms so that

$$Q_{nl} = -(Q_d + Q_i) \tag{2.14}$$

The dissipative term, Q_d, in Eq. (2.8) describes the loss in the system due to viscous damping, wave breaking, and other parasitic effects. Because of the complicated and elusive nature of the nonlinear and dissipative terms, some researchers lump them into a single term (Plant, 1986). Doing this, on qualitative arguments it can be found that

$$\frac{Q_{nl} + Q_d}{\omega_0} = -\frac{\omega k u}{A\rho c} < N > . \tag{2.15}$$

This simplified expression assumes that $k^4\Psi(k)$ is small and that a relaxation time model can be used to describe the decay of the spectrum due to dissipation.

2.1.3 Expressions for the Wave Spectrum

Using these expressions for the source terms in Eq. (2.8), one can solve for the action and, hence, the displacement spectrum explicitly. However, the form of the solution is sensitive to what approximations are used for the different terms. Following are several of the most important solutions of Eq. (2.8) in microwave scatterometry.

The Phillips Model

The original Phillips model is based on the assumption that the waves would continue in height until some "saturation range" is reached at which point the spectrum ceases grow. Any additional input to the system will result only in more wave breaking. It is postulated that the small wavelengths saturate first, followed by the longer waves as the wind speed increased. The form of this model is

$$\Psi(\mathbf{k}) = Bk^{-4} \tag{2.16}$$

where k is the wavenumber and B is a function at most of the angle between the wind vector and the wave propagation. Obviously, Eq. (2.16) cannot apply exactly since it implies infinitely long waves exist with large amplitudes. This is remedied by stipulating that there is some cutoff wavenumber below which no waves will grow at a given wind speed.

It is clear that if the saturation range exists, it is well above any normally observed wind speed since the radar cross section continues to increase even at very high wind speeds (Phillips, 1985).

The modified Phillips model accounts for this increase in the small wave portion of the spectrum by allowing for different "degrees of saturation" where the spectrum is given by

$$\Psi(\mathbf{k}) = B(k, \phi, u_*)k^{-4} \tag{2.17}$$

and the degree of saturation is $B(k, \phi, u_*) = \beta \cos(\theta)^p (u_*/c)$, where u_* is the friction velocity, β is the wave growth rate, c is the phase velocity of the wave, and p is a constant found by comparing with empirical data.

Although the idea of a saturation spectrum is somewhat dubious, the Phillips model is still used in some theoretical modeling because of its simplicity and flexibility. The wave spectrum in the region of the Bragg resonant waves is usually thought to be of the k^{-4} form given by the Phillips models.

The Durden and Vesecky Model

The Durden and Vesecky model (Durden and Vesecky, 1985) extends the Phillips model by noting that Phillips model only applies to irrotational fluids. This is generally not the case for a wind driven wave field. The physical mechanism which causes this condition to fail is when an appreciable wind drift layer exists, that is, when the surface layer is dragged along with the wind. It has been shown that this layer can greatly reduce the height at which a wave will break (Banner and Phillips, 1974). This "microbreaking" occurs at higher wavenumbers and somewhat limits the growth of the high wavenumber portion of the spectrum. Accounting for this deviation the Durden and Vesecky wave height spectrum is given as

$$\Psi(k,\phi) = \frac{0.004k^{-4}}{2\pi} \cdot \begin{cases} e^{-0.74(K_c/k)^2}(1 + c(1 - e^{-sk^2}))\cos 2\phi & k < 2 \\ \left(\frac{bku_*^2}{g}\right)^{a\log(k/2)}(1 + c(1 - e^{-sk^2}))\cos 2\phi & k > 2 \end{cases} \tag{2.18}$$

where k is the wavenumber, ϕ is the angle between the waves and the look direction, K_c is a cutoff wavenumber which depends on wind speed, u_* is the friction velocity, and s, b, and a are constants determined by fitting to empirical data.

The spectrum is split in order to separate the long gravity wave portion of the spectrum from the capillary portion. This model was readily applied to microwave scattering in an attempt to explicitly include the effect of swell on the radar cross section. The model suffers, though, from the need to fit several of the parameters using empirical data.

The Plant Model

The Plant model attempts to solve Eq. (2.8) for wavenumbers substantially above the peak. The goal of this model is to include the effect of the long waves modulating the amplitude of the small waves in the solution (Plant, 1986). The form of the modulation is assumed to be linear, described by a complex modulation transfer function. Using these approximations, the Plant model is given by

$$\Psi(\mathbf{k}) = \frac{A}{k^4}\left\{\frac{\beta}{\omega} + \frac{m_i'\Omega S^2}{\omega}[1 + (\gamma_0 + \gamma_1)\cos(\theta - \theta_w)]\right\} \tag{2.19}$$

where γ_0 and γ_1 depend on wavenumber and the m_i is the imaginary part of the modulation transfer function. This result is found by taking the ensemble average of Eq. (2.8) and expanding the result in terms of the mean squared long wave slope to the first order.

Since this model is derived explicitly for radar scattering applications, it is applicable only in the high wavenumber region. It does, however, include the effects of the long swell in the modulation of the small wave spectrum. It suffers from a lake of information about some of the variables used in the model including the short wave growth rate and the friction velocity of the surface winds.

2.1.4 Transition

The characterization and modeling of the wind driven sea is a very complicated proposition. The inherent non-linearity and chaotic behavior make standard modeling techniques difficult to apply and questionable in their validity. Never the less, all of the models presented in this section have been applied to microwave scattering theory with varying degrees of success. All of them have regions where they work fairly well and regions where the do not apply. This illustrates the need to

better understand the physical mechanisms involved in the scattering process. Once these mechanisms have been determined, EM theory can be applied to calculate the radar properties.

2.2 Electromagnetic Scattering from the Sea Surface

The scattering of electromagnetic radiation from a rough sea surface is a difficult problem. Through Maxwell's equations, the theoretical solution of any scattering problem can be written down exactly using Huygen's equations. In this light, the only problem in ocean scattering is properly specifying the conditions at the scattering boundary. As has been shown in the previous section, specifying the exact boundary of the sea surface is not a realizable situation.

In any case, even if the exact surface is specified, solving the scattering equations may still be impossible. For these reasons, the field of ocean scattering is a field of making approximations for both the ocean surface and the scattering equations in order to make them solvable. This section will present the scattering approximations most relevant to the field of ocean scattering.

2.2.1 Radar Scattering

Determining the amount of radiation scattered from an object or surface is a fundamental problem of electromagnetism. A great deal of effort has been expended in studying scattering problems like the sea surface problem. The exact solution for the scattered electric field can be represented using Huygen's equation:

$$\mathbf{E}_r = \int\int_S' \left\{ i\omega\mu \overline{\overline{G}}(\bar{r},\bar{r}) \cdot [\hat{n} \times \mathbf{H}(\bar{r}')] + \nabla \times \overline{\overline{G}}(\bar{r},\bar{r}) \cdot [\hat{n} \times \mathbf{E}(\bar{r}')] \right\} dS'. \qquad (2.20)$$

where $\overline{\overline{G}}$ is the dyadic green function and is given by

$$\overline{\overline{G}}(\bar{r},\bar{r}') = (\overline{\overline{I}} + \frac{\nabla\nabla}{k^2})\frac{e^{ik|\mathbf{r}-\mathbf{r}'|}}{4\pi|\mathbf{r}-\mathbf{r}'|}. \tag{2.21}$$

This equation states that the scattered **E** (or **H**) can be specified in terms of the tangential **E** and **H** fields at the surface of the scatterer. This is a general principle of EM theory and can, in principle, be used to solve any scattering problem. In practice, application of this equation may be problematic.

Radar measurements are usually quantified in terms of the "cross section", σ. The cross section of the target or illuminated area is defined from **E** using the relation

$$\sigma = \lim_{r->\infty} 4\pi r^2 \frac{P_i}{P_s} \tag{2.22}$$

where P_i is the incident power and P_s is the scattered power.

This parameter can be roughly interpreted as being a measure of how "big" the object appears to the radar system. As such it depends as much on the parameters of the radar such as polarization and frequency. In radar applications it relates the transmitted power to the return power via the radar equation. This relation is:

$$P_r = \frac{P_t G_s \sigma_\circ}{(4\pi r^2)^2} \tag{2.23}$$

where P_t is the transmitted power, G_s is the gain of the radar system, and r is the distance to the object and σ is the radar cross section. If the target is area extensive, as is the case with most ocean scattering measurements, then the normalized radar cross section, $\sigma_\circ$ is a more meaningful measure of the radar "brightness". $\sigma_\circ$ is the total radar cross section divided by the illuminated area. This removes the dependence of the distance and antenna beamwidth from the power measurement. In other words, it gives the brightness on a per–unit–area basis.

As stated previously, some approximation is necessary in order to evaluate Eq. (2.20) and determine the cross section of the sea surface. In general it is necessary to assume various types of scatterers are involved and treat them individually. Both theoretical, and empirical models have been developed to describe various proposed sea scatterers.

2.2.2 The Composite Model

There have been several recent models which attempt to predict the values for σ_o that are observed in experiments (Durden and Vesecky, 1985; Plant, 1986; Donelan and Pierson, 1987). All of these models are based on an assumed scattering model which is called the composite model. The composite model is described in full detail in these papers and so is only outlined here.

As discussed in the previous section, when the wind begins to blow over an initially undisturbed surface, the immediate result is the generation of centimeter sized capillary waves. In this case, one can make the approximation that the amplitude of the displacement of the water surface from it's mean value is small compared to the wavelength of the incident radiation. In this case, the integral in Eq. (2.20) simplifies a great deal using small perturbation theory (SPT) and can be evaluated to find the normalized radar cross section as:

$$\sigma_o = 16\pi k_m^4 |g_{ii}(\theta)| \Psi(2k_m \sin\theta, 0) \tag{2.24}$$

where k_m is the microwave wavenumber, Ψ is the wave height spectrum, θ is the incidence angle, and g_{ii} is the reflection coefficient which depends on the polarization with

$$g_{HH} = \frac{\epsilon_r - 1}{\left[\cos\theta + (\epsilon_r - \sin\theta)^{\frac{1}{2}}\right]^2} \tag{2.25}$$

and

$$g_{VV} = \frac{\epsilon_r - 1\left[\epsilon_r(1+\sin^2\theta) - \sin^2\theta\right]}{\left[\epsilon_r\cos\theta + (\epsilon_r - \sin^2\theta)^{\frac{1}{2}}\right]^2} \tag{2.26}$$

and ϵ_r is the permittivity of the water (Wright, 1966). Obviously, the small perturbation criterion is rarely satisfied at microwave frequencies on the sea surface. Usually there are much larger waves present. The next logical step is to modify this theory to include the longer waves.

The modified scattering model is called the composite model. The name arises from the main assumption of the theory: that the surface is composed of many small, locally planar "patches" which, local satisfy the small perturbation criteria. It is further assumed that the power scattered from each patch adds independently. The effect of the long waves in this model is to merely tilt these patches and change the local incidence angle as shown in Fig. 2.2.

To find the new radar cross section, the contribution of the individual patches is found by integrating the cross section of a patch at a particular local incidence angle (see Fig. 2.2), against the probability of finding a patch at that incidence angle or:

$$\sigma_\circ = 16\pi k_m^4 \int |g_{ii}(\theta)|\Psi(2k_m\sin\theta, 0)P(\theta)d\theta \tag{2.27}$$

where $P(\theta)$ is the probability distribution of the local wave slopes.

Obviously, the probability distribution of the wave slopes must been obtained either from a model or from empirical data. It has been shown by several researchers that the wave slope distribution can be well approximated by a Gaussian distribution.

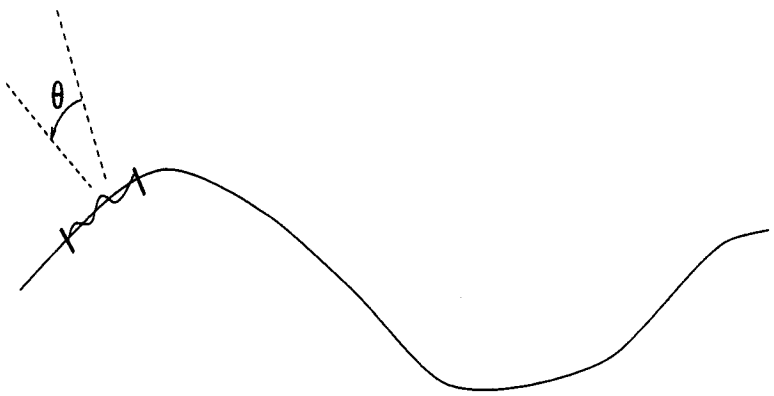

Figure 2.2: Representation of the composite model showing the definition of the local incidence angle.

If a Gaussian is assumed, then $P(\theta)$ can be written as

$$P(\theta) = \frac{1}{\sqrt{2\pi}S} e^{-\frac{\theta^2}{2S^2}} \tag{2.28}$$

where S^2 is the mean squared slope. The mean squared slope can be obtained from the wave height spectrum by

$$S^2 = \int k^2 \Psi(k) dk \tag{2.29}$$

where the integral is carried out over only the long, tilting waves. Therefore, given a wave height spectrum such as in the previous section, we can determine the mean squared slope and, hence, the distribution of the wave slopes.

This points out a deficiency of this model in that some "cutoff" wave number must be defined between the small waves (those being tilted) and the large waves (those doing the tilting). Several figures have been proposed for selecting the cutoff used in Eq. (2.29). Typical values for the cutoff are from one fifth to one tenth of the short wavenumber under consideration (Plant, 1986). The resulting

uncertainty in the value for S^2, given the possible range to choose from, is about 10 % (Hasselmann et al., 1985).

The various versions of the composite scattering model amount to using different forms for $\Psi(\mathbf{k})$ in Eq. (2.27). The results are mixed but the general consensus is that the best composite models under-predict the observed radar cross section. Because of this other scattering mechanisms have been proposed in addition to the Bragg scatterers of the composite model. These include wedge scattering (Lyzenga et al., 1983) and wave breaking (Jessup et al., 1990).

2.2.3 Wedge Scattering

Wedge scattering has been proposed as an additional mechanism for ocean scattering. Wedges occur on the sea surface when medium to large waves form the sharp peaks that most observers are familiar with. These wedges may or may not be associated with incipient wave breaking and tend to be associated with longer wavelength waves than those associated with Bragg scattering.

The usual treatment of wedge scattering is based on the geometrical theory of diffraction (GTD). The basics of this theory, worked out by Keller in the early 60's, are an attempt to generalize geometric optics (simple ray tracing) to include higher order effects such as diffraction. The basic assumptions of GTD are that a field can be assigned to each ray, and the total field at a point is the coherent sum of all the rays passing through the point. When reflecting from a surface or diffracting from an edge the ray is assumed to produce new rays which have a magnitude and phase determined by reflection or diffraction coefficients. These coefficients are then found using certain "canonical" problems (Keller, 1962).

In the ocean scattering problem, we are concerned with determining the backscatter from the waves by modeling them as a conducting wedge. A typical configuration is shown in Fig. 2.3. Using the techniques of GTD, the scattering

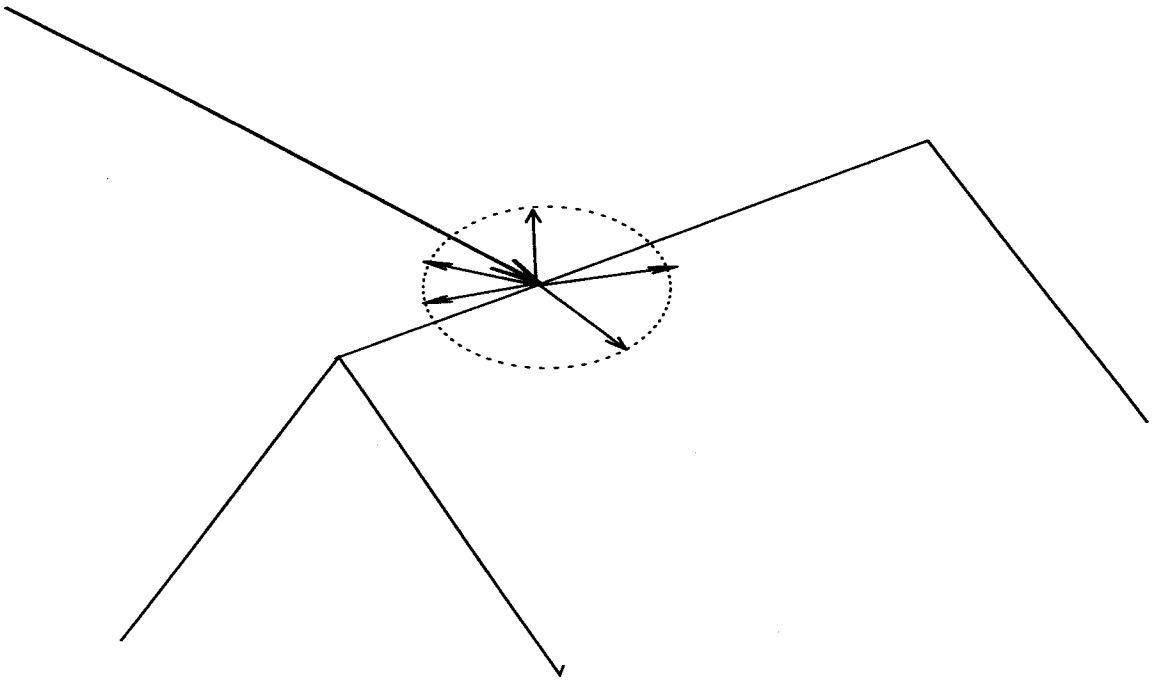

Figure 2.3: Backscattering from an edge.

coefficient for a conducting wedge is found to be

$$S = \frac{k_0}{2\pi} \int_C \frac{f \cos\phi_i \cos\phi_s + g \cos\phi_i' \cos\phi_s'}{\sin\beta_i \sin\beta_s} e^{i(\vec{k}_i - \vec{k}_s)\cdot \mathbf{r}} dl \tag{2.30}$$

where k_0 is the wavenumber, C is the contour along the edge, f is the modified E field diffraction coefficient, g is the modified B field diffraction coefficient, ϕ_i is the angle between the edge and the incident E field, ϕ_s is the angle between the edge and the scattered E field,ϕ_i' and ϕ_s' are the corresponding angles with the B field, and β_i and β_s are the angles between the incident and scattered wave vectors and the vertex of the wedge (Lyzenga et al., 1983).

The functions f and g are described in terms of the coefficients

$$X = \frac{\frac{1}{n}\sin\frac{\pi}{n}}{\cos\frac{\pi}{n} - \cos\frac{\psi-\psi_0}{n}}$$

and

$$Y = \frac{\frac{1}{n}\sin\frac{\pi}{n}}{\cos\frac{\pi}{n} - \cos\frac{\psi+\psi_0}{n}}.$$

where n is defined by $\alpha = n\pi$.

These coefficients includes the contribution from the faces of the wedge which we do not want since they are already included in the composite model. For the ocean scattering problem we are interested only in the contribution due to the edge. We can subtract the contribution of the i'th face using

$$X_i = -\frac{\sin\phi_i - \sin\phi_{0i}}{2(\cos\phi_i + \cos\phi_{0i})} \tag{2.31}$$

and

$$Y_i = -\frac{\sin\phi_i + \sin\phi_{0i}}{2(\cos\phi_i + \cos\phi_{0i})}. \tag{2.32}$$

Therefore the modified diffraction coefficients are given by

$$f = X - Y - \sum_{faces}(X_i - Y_i) \tag{2.33}$$

and

$$g = X + Y - \sum_{faces}(X_i + Y_i). \tag{2.34}$$

Using these relations, we can find the cross section using

$$\sigma = \frac{4\pi}{k_0^2}|S|^2. \tag{2.35}$$

In this case, the wedges are assumed to be oriented horizontally and the scattered fields are scattered back to the observer. Therefore, for the scatterometer, the parameters in Eq. (2.30) are given by:

- $\Phi_i = \Phi_s = 0$ for H-pol,$\Phi_i = \Phi_s = \pi/2$ for V-pol;
- $\Phi_i' = \Phi_s' = \pi/2$ for H-pol,$\Phi_i' = \Phi_s' = 0$ for V-pol;
- $\beta_i = \beta_s = \pi/2$ for backscattering.

In this case, the integral for S decomposes into H- and V-Pol components which are easily evaluated. Typical values for the cross section are shown in Fig. 2.4

The total contribution to the total radar cross section from wedge scatterers depends on what the density of the wedges are and what their particular geometry is. Assuming "reasonable" values for these parameters, researchers have shown that it is possible that at least some of the radar cross section may be due to wedge scattering (Lyzenga et al., 1983). Fig. 2.3 suggests that any contribution from wedge scattering should be most apparent in the H-pol return.

When added to a representative Bragg model, the wedge scattering tends to slow the rapid roll off of the Bragg contribution and provide a slow decrease with incidence angle. However, the true size and density of scattering wedges on the sea surface has not been measured empirically. A proto-typical wedge+Bragg model is shown in Fig. 2.5

2.2.4 Wave Breaking

Another proposed scattering mechanism is breaking waves. Breaking waves are certainly the most visually obvious mechanism on the wind driven sea, especially under high wind speed conditions. Despite this, relatively little work has been done towards including wave breaking in a scattering model. Most of this stems from the fact that wave breaking is a highly non-linear and fleeting process. Indeed the process is not well understood.

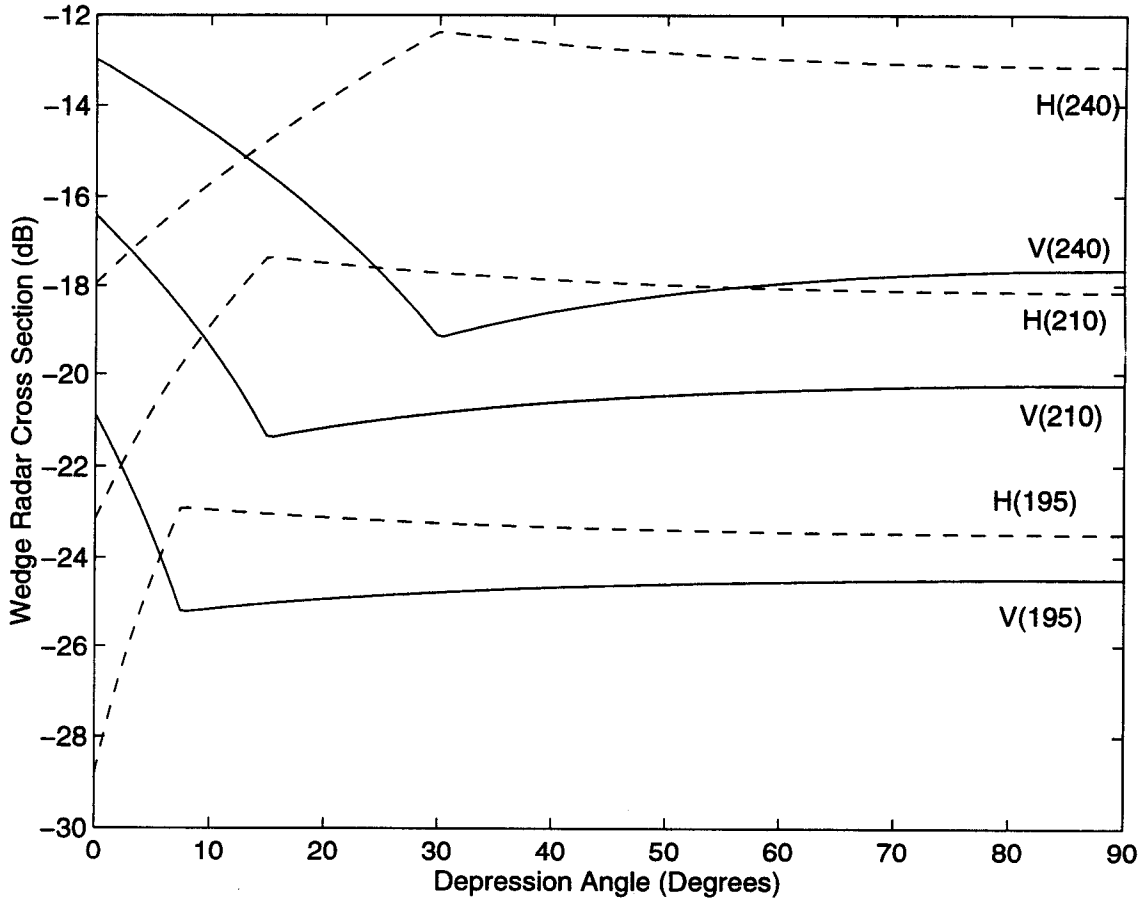

Figure 2.4: Radar cross section of a single wedge of unit length with specified exterior angle (parenthesis) verses grazing angle.

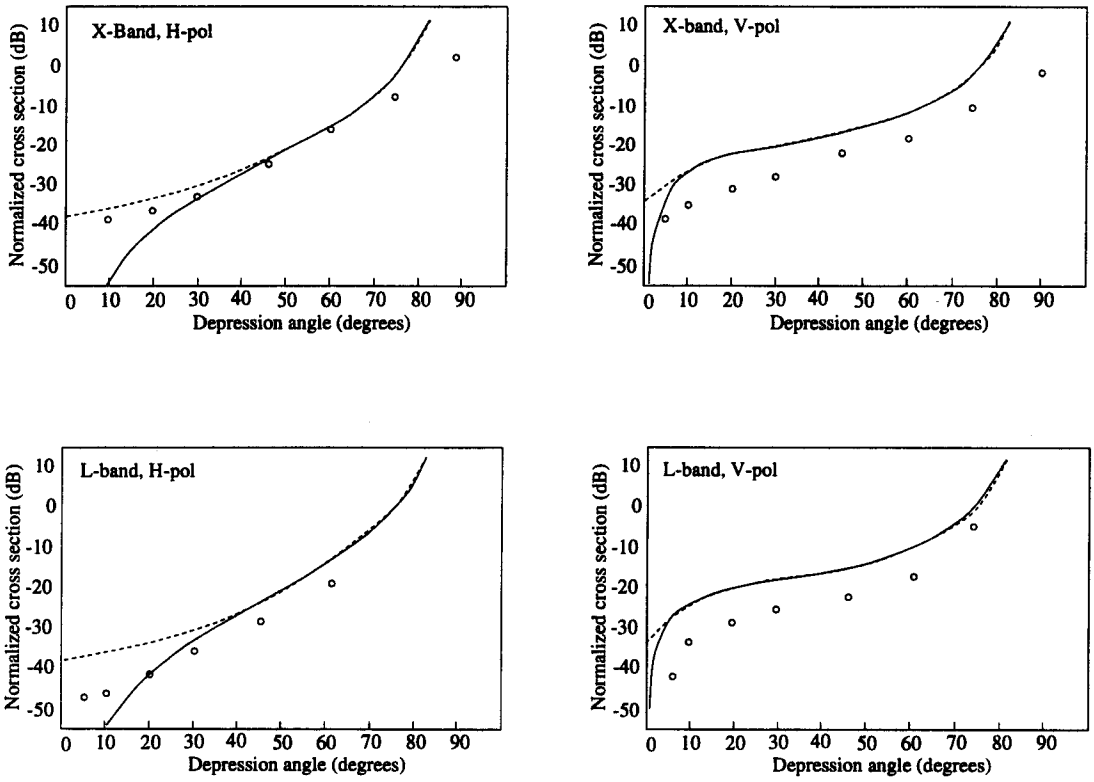

Figure 2.5: Proto-typical wedge scattering model. Solid line indicates Bragg only scattering, dashed line indicates Bragg plus wedge scattering. Circles indicate empirical measurements at 11 m/s. (Taken from Lyzenga (1984)

Most of the theoretical work on breaking waves has been done in the field of hydro-dynamics with only a secondary thought toward radar scattering applications (Longuet-Higgins and Turner, 1974). The results of this work are difficult to apply to a random wind driven sea. However, there are several general qualities of breaking waves which can aid in the study presented here. Also, there has been some recent empirical work which has indicated that wave breaking needs to be included in any complete scattering model.

There are two different types of wave breaking that occur on a wind driven sea; large scale breaking and small scale breaking. The more visible of the two is large scale breaking. This is because large scale breaking is associated with turbulent white caps while small scale breaking tends to be non-turbulent.

Large scale breaking begins when the wave height grows to that point where the slope is so steep the wave structure becomes unstable. The wave then degenerates under the force of gravity. If the action is vigorous enough, air is entrained in the water and a visible white cap is formed (see Fig. 2.6).

Small scale breaking is caused when the drift layer velocity caused by the surface wind stress become comparable to the phase velocity of the small waves. Under these conditions, the wave structure can become unstable and break at much smaller wave heights than under normal conditions. When these small waves break, small specular portions may be presented to the radar, enhancing the radar return. However, no current theory exists to quantify microbreaking and include it in a scattering model. More research is definitely needed into this area.

The effect of large scale breaking of the radar return is substantially different than that from other scattering mechanisms. Several properties of the scattered

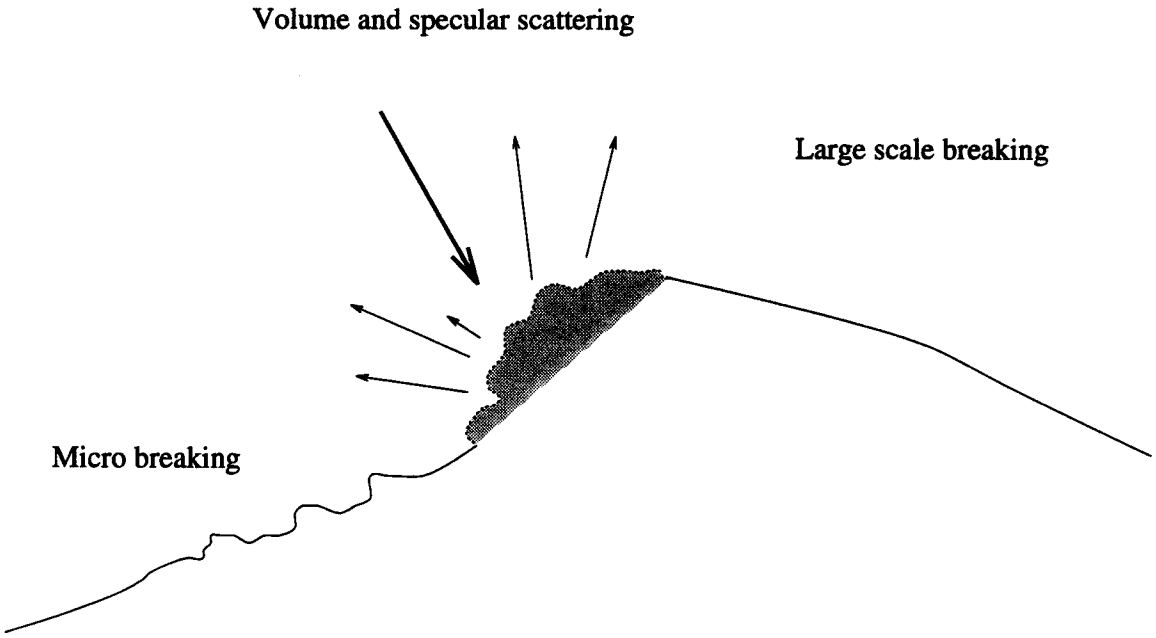

Figure 2.6: Typical breaking wave configuration.

fields can be used to measure the total cross section due to wave breaking (Jessup, 1990).

Since the breaking portion of the wave travels at the phase velocity rather than the group velocity of the wave, the Doppler shift of the radar return will be higher. There is also a rather large range of velocities associated with the rolling white cap so the bandwidth of the return will be high. The scattering from breaking waves tends to be specular in nature so the radar cross section is much larger than that due to Bragg scattering or wedge diffraction.

Visual comparison of radar returns and video of the sea surface has indicated that "sea spikes", large, short lived increases in radar cross section, are sometimes correlated with breaking waves (Jessup, 1990). Some of these properties are evident in the short data segment in Fig. 2.7.

Using detectors designed to detect these events it has been estimated by some researchers that breaking waves may contribute up to 20 % of the total radar cross section (Jessup et al., 1990). The contribution of the detected events to the total radar cross section as a function of friction velocity, u_*, is shown in Figs. 2.8 and 2.9.

2.2.5 Inventory

The groundwork for dealing with potential sea surface scatterers has already been laid by theoretical and empirical work by previous researchers. Understanding the wind-wave interaction on the sea surface is crucial to any attempt to analyze backscatter data from the air-sea interface. In this context "understanding" means knowing what physical processes are taking place on the sea surface and how they influence the radar return. Although there has been a great deal of research on

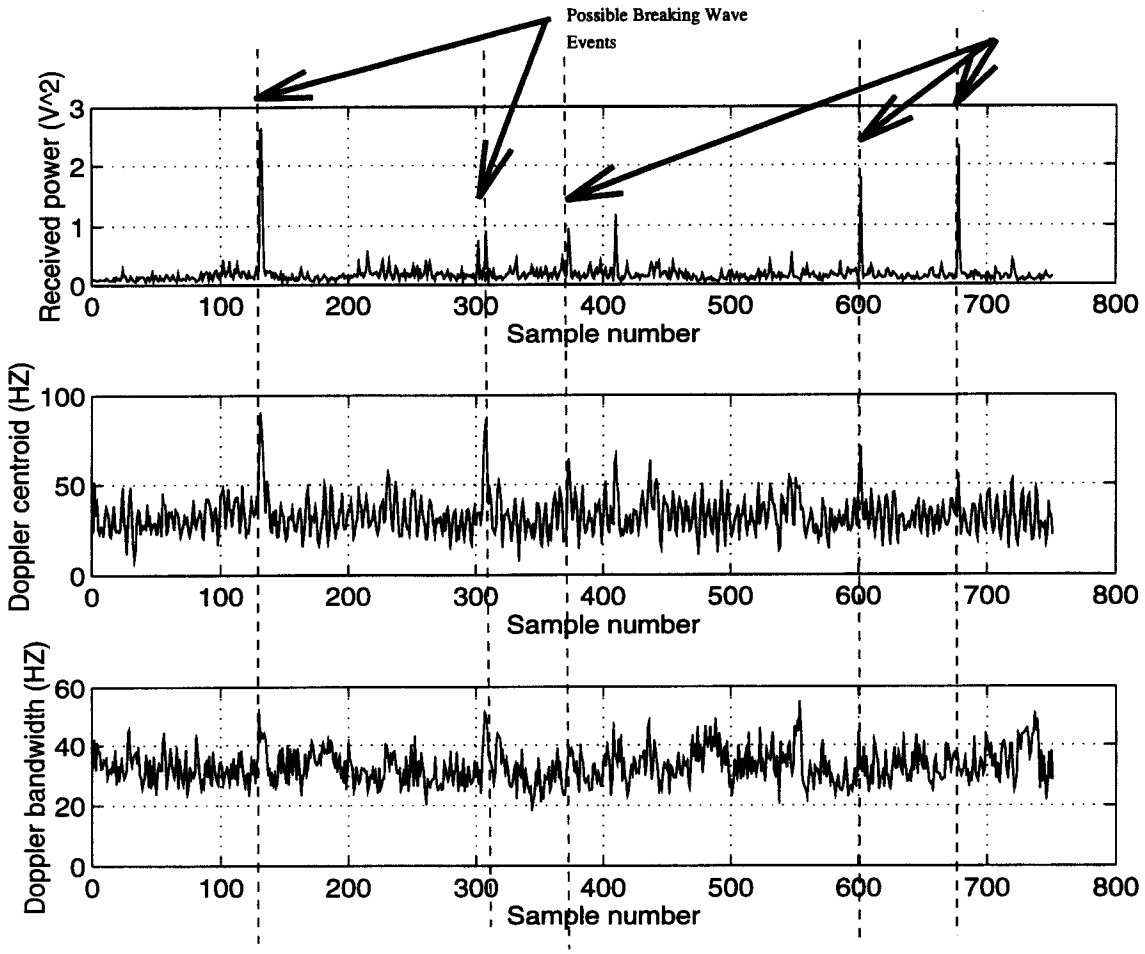

Figure 2.7: Radar time series from the Yscat94 experiment. Parameters for this measurement are: H-POL, 60 degrees, 8.5 m/s, upwind, Ku band.

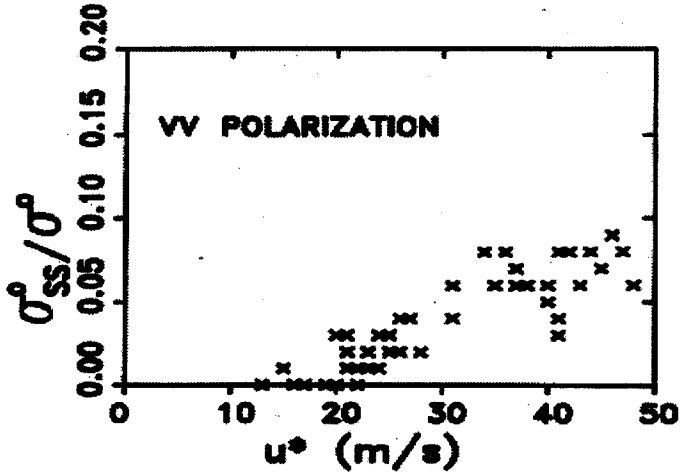

Figure 2.8: Breaking wave contribution, V-Pol. Taken from Jessup (1990)

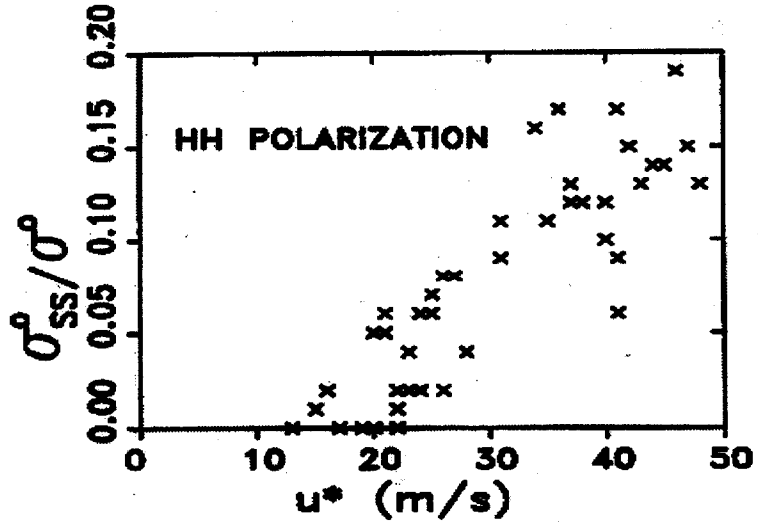

Figure 2.9: Breaking wave contribution, H-Pol. Taken from Jessup (1990)

the subject, the diversity of opinions and models shows that there is still some work to be done. This is not surprising since the subject involves many difficult areas of study such as nonlinear wave interaction, wave breaking, short wave modulation, hydrodynamics, and electromagnetics. In any case, the final pass or fail test for any of these theories must lay in empirical comparison. The rest of this dissertation presents an effort to gather and analyze empirical data in an attempt to verify the validity of current scattering models.

Chapter 3

YSCAT94 EXPERIMENT

3.1 Introduction

The Yscat94 experiment was a comprehensive, long term study of the air-sea interface conducted on Lake Ontario from the beginning of May to the end of November 1994. The goal of the experiment was to obtain measurements of the radar cross section under a wide variety of environmental conditions. This chapter describes the experimental site, the equipment used in the experiment, the observations made, and the conditions observed during the experiment.

3.2 Experimental Site

The site for this experiment was a research tower operated by the Canadian Centre for Inland Waters (CCIW). The tower is located at the west end of Lake Ontario approximately 1.1 km off shore. At the location of the tower, the lake bottom slopes evenly at about 11 m/km from shore to a depth of 12 m at the tower. The shoreline is fairly straight and the bottom contours are parallel in a region extending 3 km from the tower in all directions (see Fig. 3.1). The annual variation in water depth is less that 0.5 m and there is no significant tides, seiches, or associated currents. Other random currents are typically less than 10 cm/s.

Prevailing winds in this area are westerly which provide fetches from 1.1-2 km. However, fetch can vary widely with wind angle up to 300 km with a south-easterly wind. Because of the generally short fetch, extremely long waves are rare. Wave periods of 4 s are fairly common while periods of up to 8 s occur less frequently.

Wave periods of more than 4 s are modified by the finite depth of the location. However, waves with periods less than 4 s can be considered to be "deep water" waves (Donelan et al., 1985).

The tower itself is designed to minimize the disruption of the surface airflow (see Fig. 3.2). It is a two level design with a catwalk located 4 m from the water surface and a large $100m^2$ experiment deck located about 6 m from the mean lake surface. At the four corners of the tower are support legs which extend up to 10 m above the lake. In the center of the deck is a small equipment shack and a mast that extends up to 12 m above the surface. The tower is supplied with 120 V AC and a telephone hook-up via an under water cable which terminates at an on-shore trailer.

3.3 Equipment: Yscat

The primary instrument used during the experiment was the Yscat radar. Yscat was designed to be a tower mounted radar system which could operate in the hostile environment of a unmanned sea platform. In addition, in order to study the dependence of the radar cross section to various radar and environmental parameters, it was necessary to design the radar so it could continuously vary its operating parameters (frequency, polarization, azimuth, elevation, etc.) over a long unmanned deployment. To achieve this goal, it was necessary to develop both a very agile radar system and a novel control system to operate it from over a thousand miles away.

The radar system consists of several subsystems under the control of a main controller. These subsystems include the RF, IF, calibration and pre-processing, and the positioning subsystems. The location of the various sub-systems and equipment is shown in Fig. 3.3.

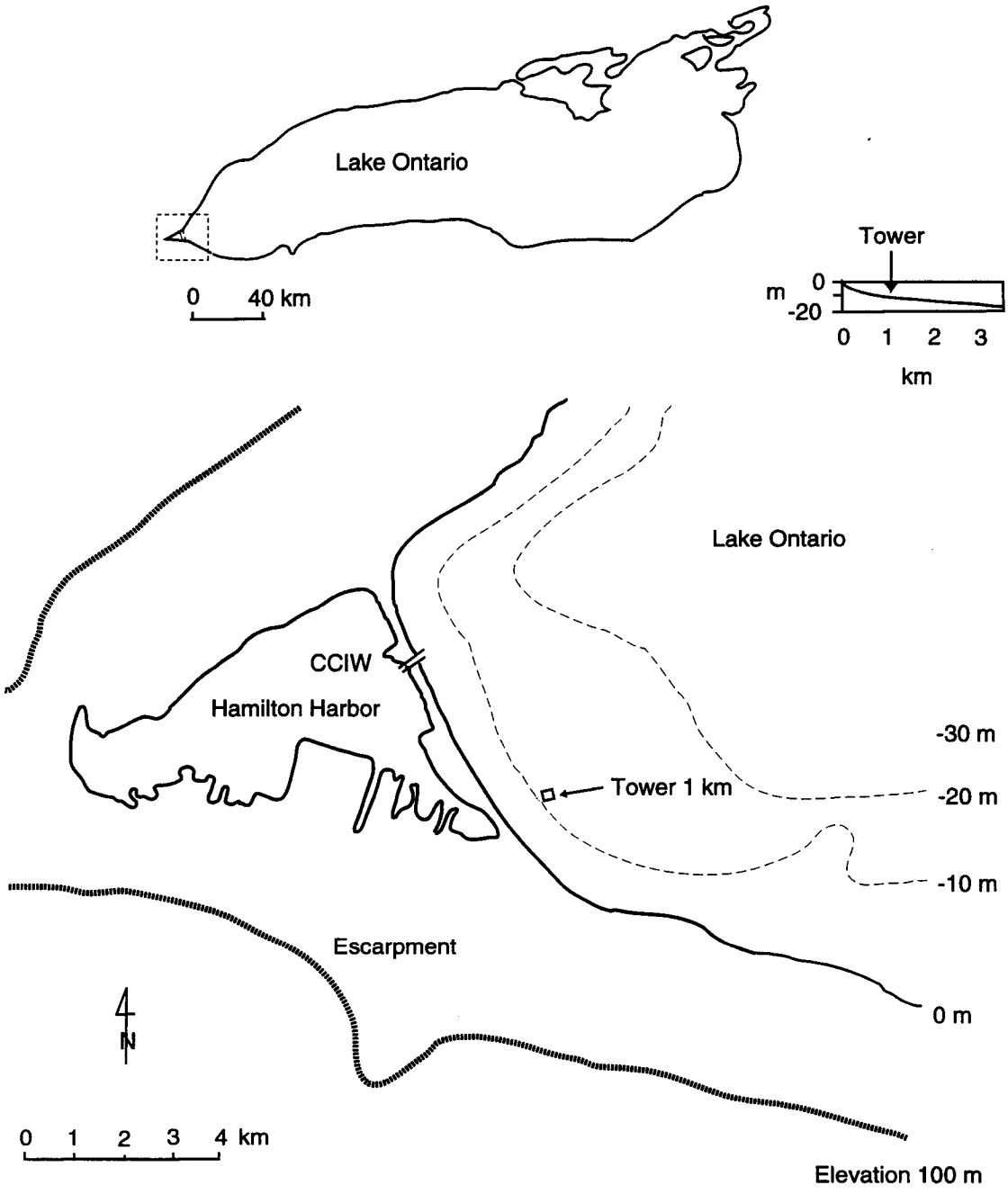

Figure 3.1: Location of Lake Ontario deployment site

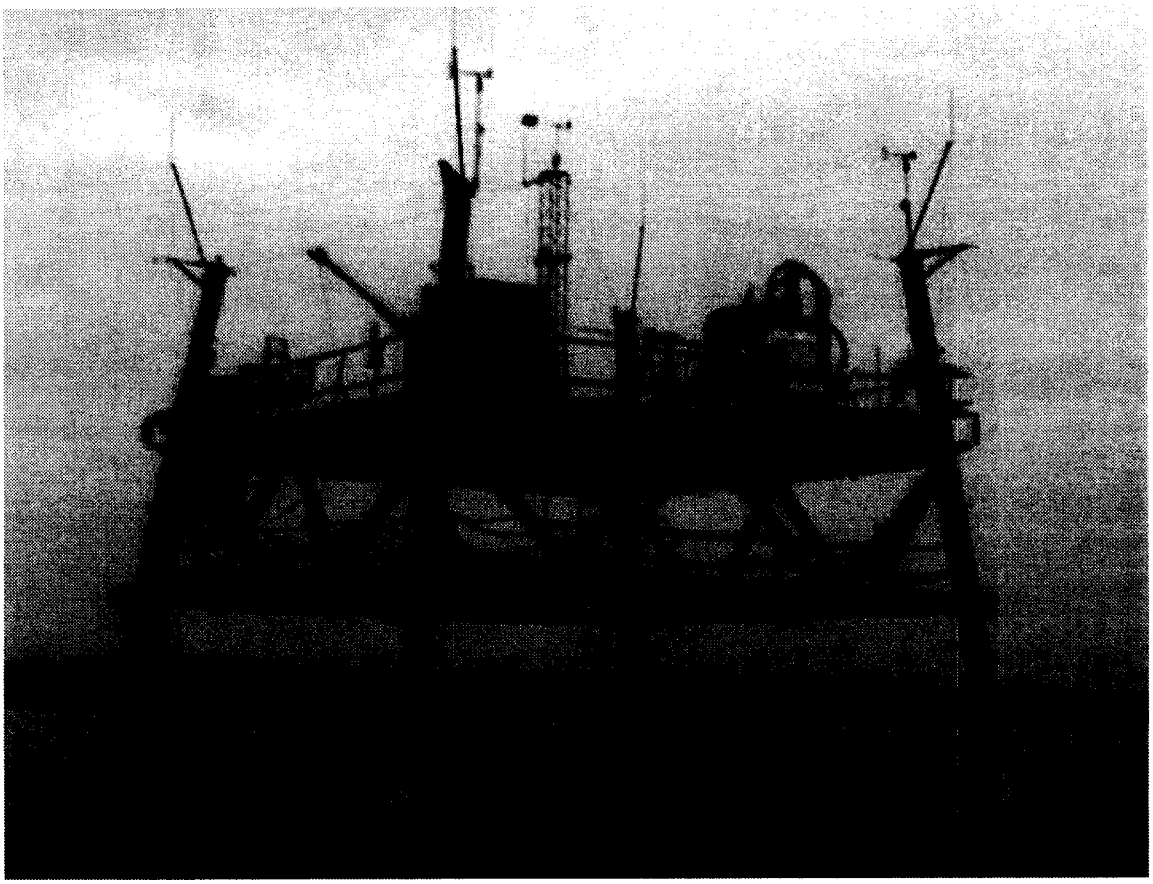

Figure 3.2: The CCIW WAVES research platform. Yscat is the crane-like structure on the upper deck. Also visible are the two anemometers on the support legs and the bi-vane anemometer on the tower in the center of the platform.

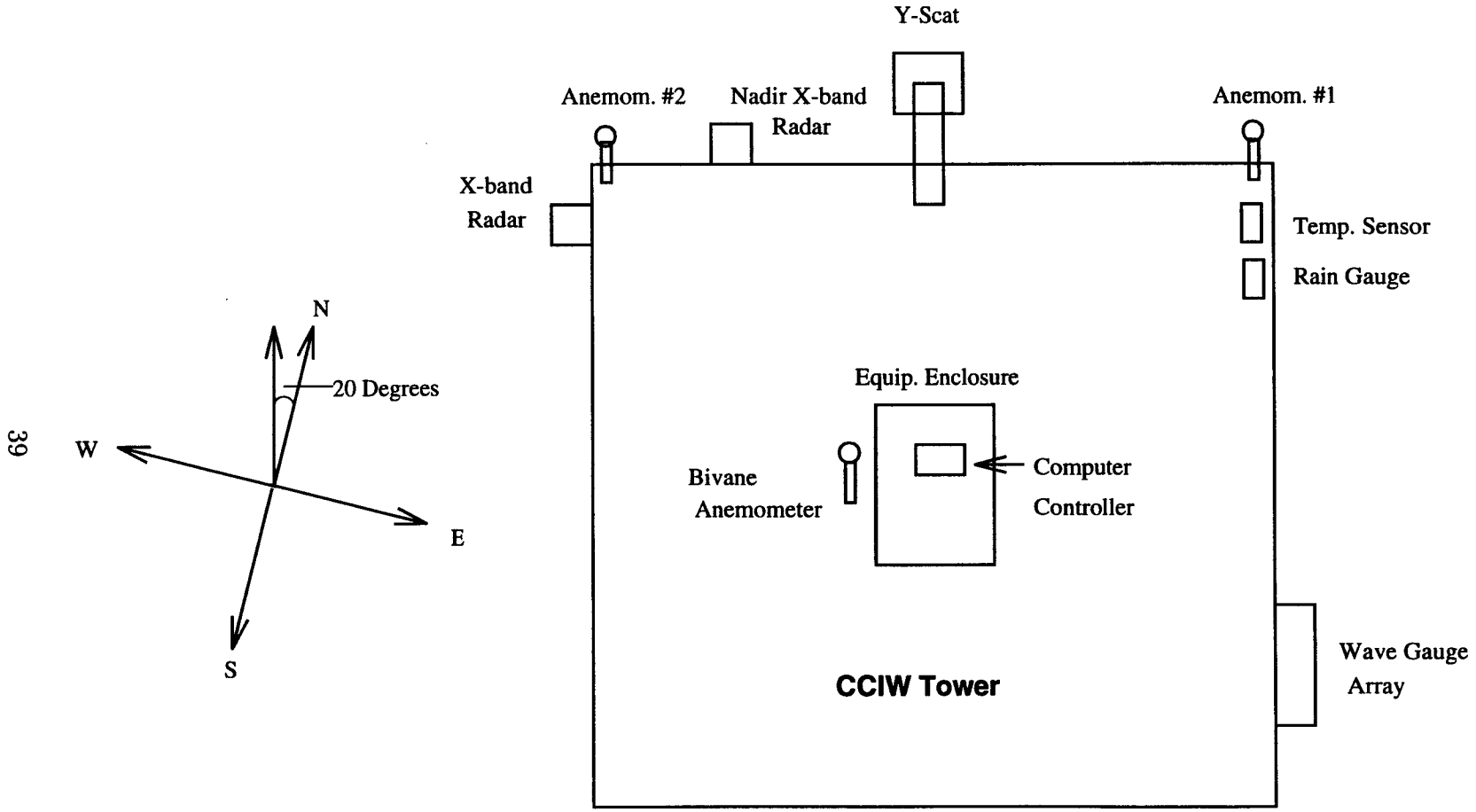

Figure 3.3: Layout of the various systems on the CCIW research tower.

Center Frequency	2-18 GHz
Peak Output Power	23 dBm
Transmit Polarization	V or H (selectable)
Two-Way Antenna Beam width	10-5 degrees
Receive Polarization	V and V
Polarization Isolation	15-20 dB
LO-IF	166 MHz
Dynamic Range	50-110 dB
Baseband Signal Bandwidth	900 Hz

Table 3.1: RF System Parameters

RF Subsystem

Y-Scat is an ultra-wide band radar with an operating frequency that can be varied continuously from 2 to 18 GHz. The heart of the RF sub-system is an HP-83590A microwave generator and a variable YIG filter (see Fig. 3.4). The generator is controlled via an HPIB link to an embedded controller. The generator can be remotely switched to any frequency from 2-18 GHZ.

From the RF generator, the signal is split between the transmitter and the receiver using a 3 dB power splitter. The transmitter signal is amplified to 23 dBm and either routed through the antenna or through the internal calibration circuit. If the calibration circuit is selected, the signal is attenuated by 60 dB and then split evenly and coupled into the two receive circuits using 10 dB directional couplers.

The transmit antenna is a custom designed 36" ellipsoidal figure reflector that gives a nearly constant 5 degree beam width over most of the operating bandwidth (from 4 - 18 GHz) of the radar system (see Fig. 3.5). The feed is a dual polarization, sinuous feed in order to minimize VSWR changes over the large frequency range. This special antenna design is crucial to making broad spectrum measurements of the same size surface patch.

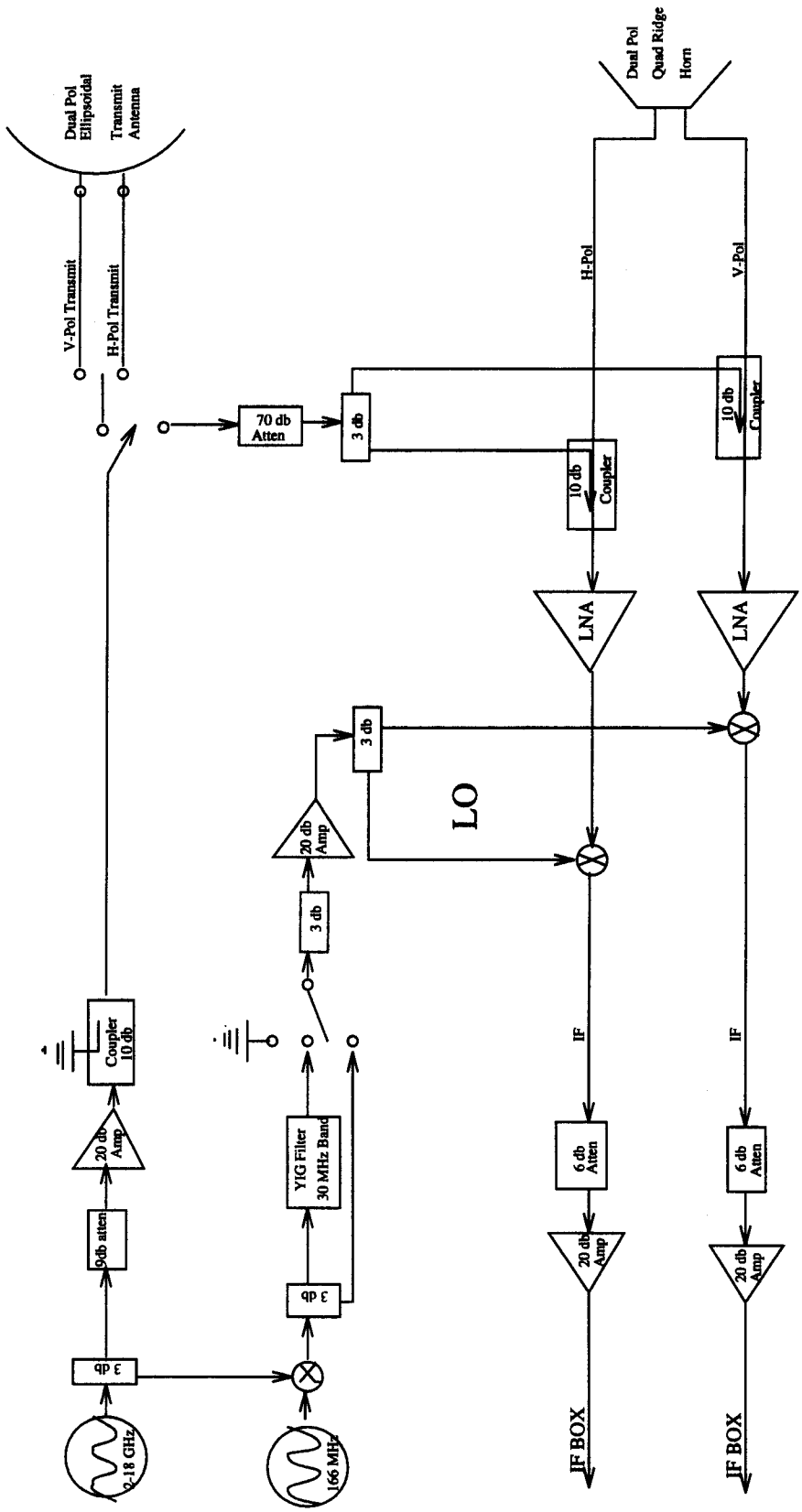

Figure 3.4: Y-Scat block diagram.

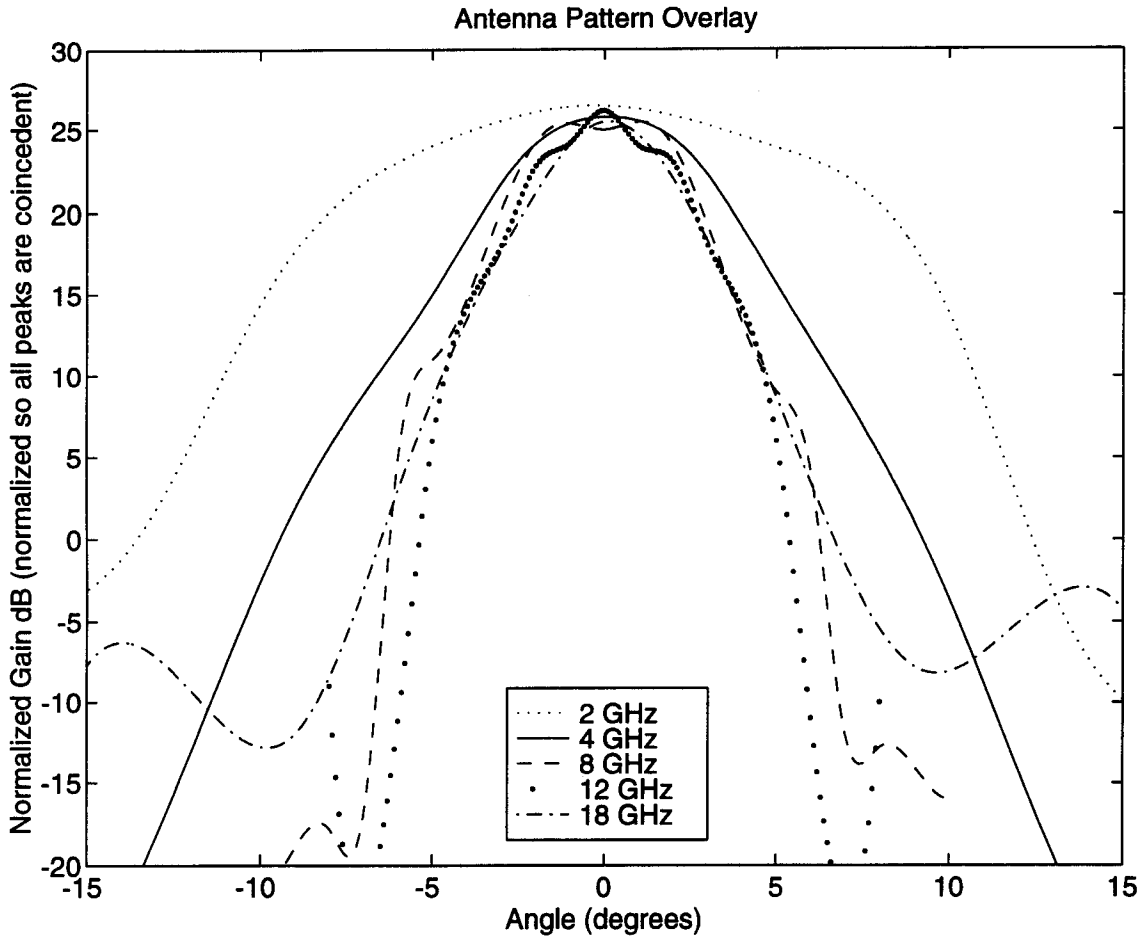

Figure 3.5: Two-way antenna patterns.

The receive antenna is a quad-ridge, dual-polarization rectangular horn with an aperture of 10 x 10 cm. This provides a broader pattern than the transmit antenna to help minimize the effects of pointing alignment errors.

The receiver is a dual pol system designed to maximize the system SNR. After each polarization is received and amplified using low noise amplifiers, both channels are mixed down to the IF in a single side band mixing operation.

The SSB LO is generated by mixing the RF carrier with the desired IF signal in a normal double sideband mix, and then filtering off one of the sidebands using a voltage controlled YIG filter. The YIG filter has a 30 MHz 3 dB bandwidth that can be varied continuously from 2 to 18 GHz. This provides about 60 dB of carrier and sideband suppression over the entire operating range.

IF Subsystem

The IF sub-system is designed to operate at a constant frequency regardless of the operating mode of the RF sub-system. The IF signal source is an HP-86568B signal generator which can be remotely controlled. Under normal operation the IF is 166 MHz (see Fig 3.6).

The horizontal and vertical signals are received from the RF system, split into I and Q signals, and mixed down to baseband. The baseband signal is high pass filtered at 1 Hz to eliminate antenna feed through and any returns from stationary targets, and then amplified from 0-60 dB and low-pass filtered at 900 Hz using a programmable filter-amplifier. The signal is then digitized by the computer/controller. The entire SSB IF circuit is phase balanced and a sample and hold circuit is utilized to provide an image rejection of more than 40 dB across the baseband bandwidth of $\pm$500 Hz.

Calibration, Positioning, and Pre-processing Subsystems

The ultra-broadband nature of the radar system presents a formidable calibration challenge. Not only do the various system gains drift with temperature, but this drift is frequency dependent. Temperature drift is minimized by a temperature control system that can maintain the RF components at 25° $\pm$ 5° C under normal

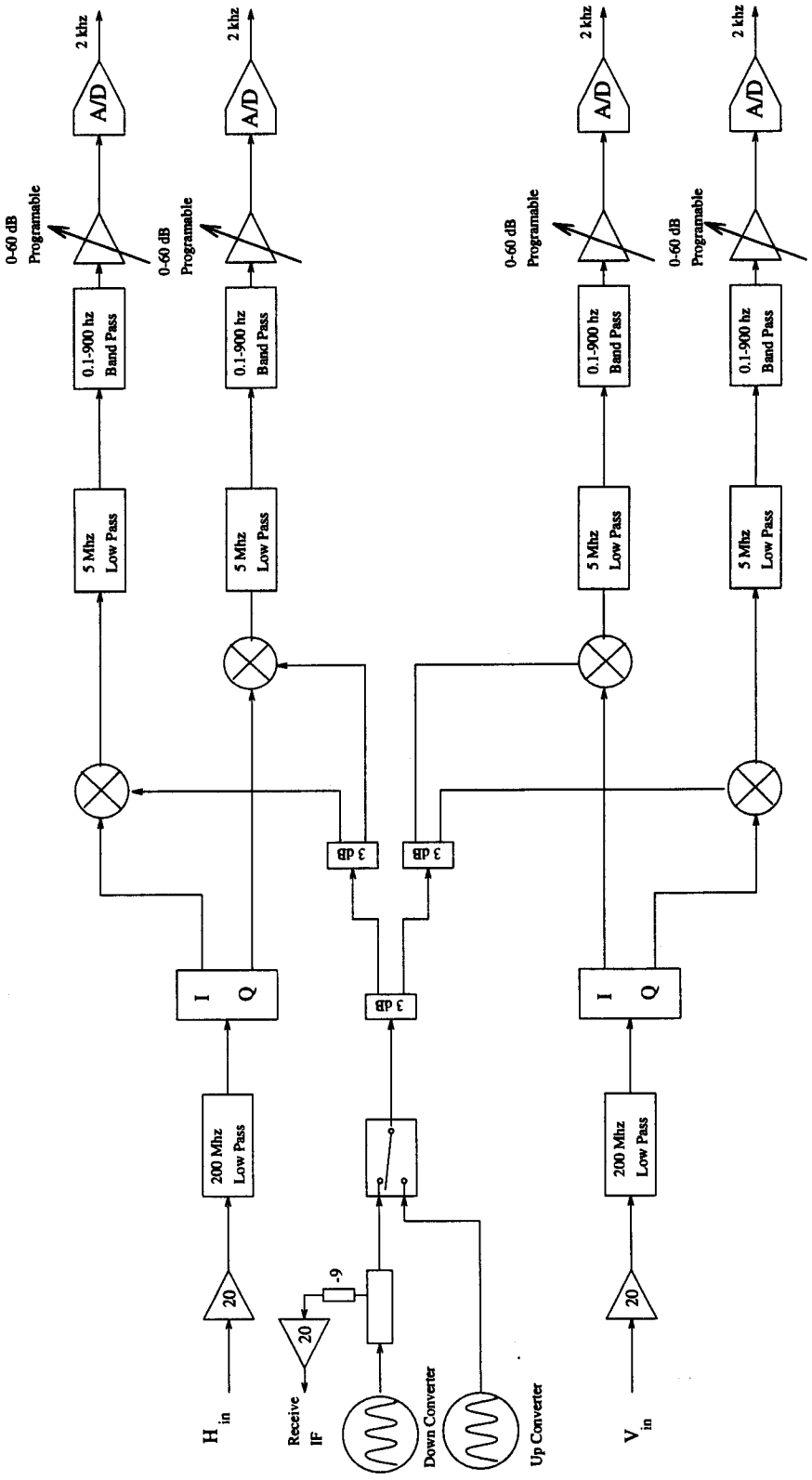

Figure 3.6: IF circuit block diagram.

operating conditions. The residual system drift requires that the Y-Scat system be continuously calibrated while in operation.

The internal calibration is accomplished by routing a portion of the transmit signal through the entire transmit-receive chain. This is done at each frequency of operation just before and just after each σ_o measurement, and thus allows the true transmit power for each measurement to be determined with great precision.

A custom two axis mounting system allows the radar to be pointed in almost any direction from $\pm 80°$ in azimuth and from $+30°$ to $-90°$ (nadir) in elevation. Two digitally controlled stepping motors are used to position the radar system. Pointing control is accurate to 0.1 degrees. Direction is measured using twelve bit absolute encoders mounted directly to the support shafts.

Under normal conditions, baseband signals produced by the IF subsystem are sampled via sample and hold circuitry at 2 kHz on each of four signal lines (in phase and quadrature phase for both h and v pol returns.) Since this data rate is unsuited for extended unattended deployments, it is reduced by pre-processing the data.

First and second moment estimation methods are used to calculate and store signal power, Doppler centroid, and Doppler bandwidth at 10 Hz. This reduces the total data rate from +50 MBytes per hour to about 1 MByte per hour. Although under normal operating conditions, the radar data will be collected weekly on tape, an on-board 1.2 GByte hard drive and 2 GByte Digital tape drive will hold up to 4 weeks worth of data.

Environmental System

Yscat is designed to support data intensive studies of ocean scattering and the air/sea interface in general. It includes a full complement of environmental sensors. The most crucial measurement for interpreting the radar data is the surface wind speed. An accurate measurement of this parameter is assured by the use of two anemometers located at the two most northern corners of the tower. The system also measures air temperature, humidity, and water temperature. Thirty second averages of all these measurements are computed and transmitted to the main computer. In addition to these instruments, Yscat also monitors a bi-vane wind stress sensor and an eight wire wave gauge array. Data from these sensors is collected at 10 Hz and stored on separate data tapes.

Control

The remote control problem is challenging because the deployment site makes it impractical to manually operate the radar system, yet the experiment goal required the radar parameters (position, frequency, polarization, operating mode, etc.) to be constantly changed. The solution was to design the system around a 486 personal computer that performs preliminary data processing and coordinates the control signals sent to the RF, positioning, IF and sampling, and environmental sub-systems of the radar.

In order to minimize the duties of the main controller, the RF and positioning subsystems are controlled by their own computer controllers which handles the details of operation and receives main commands from the central controller. The main controller reads commands from pre-written batch files which contain commands to operate the radar system for several weeks at a time.

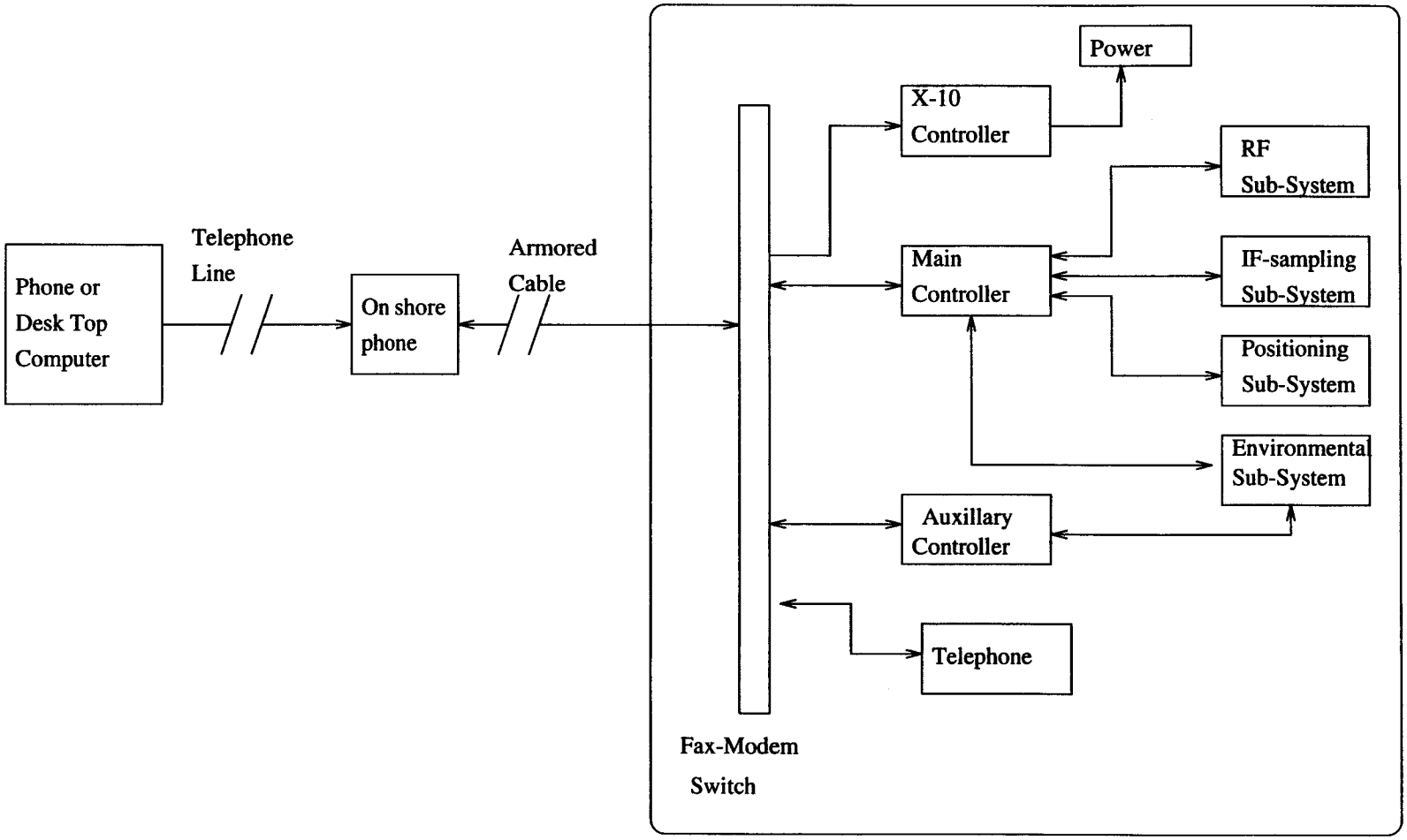

Figure 3.7: Control signal flow diagram of Yscat radar control system.

The embedded RF sub-system controller is a Kila V80 computer-on-a-board. The Kila controls the RF subsystem via a TI GPIB card and a Computer-Board AT-16 A/D card. The GPIB card communicates commands to the HP signal generator. The A/D card allows the Kila to monitor system temperature and supply voltages, generates digital signals that control high frequency switches on the RF system, and synthesizes analog signals for generating FM pulses and sweeping the center frequency on the YIG filter. The Kila receives commands from and transmits control information to the central controller via 9600 baud RS-232 connection. This relieves the central controller of much of the mundane control tasks, but still allows for strict system monitoring.

The positioning sub-system is controlled by two Precision Industries stepper motor controllers for the elevation and azimuth axes, respectively. These two controllers are pre-programmed by the central controller with anticipated control parameters and motions. The motor controllers then receive commands from the central controller via a 9600 baud RS-232 connection, which are executed according to the pre-programmed motion profiles. The movements of the radar are monitored by the central controller via two Teledyne-Gurly absolute encoders via a custom interface card. If the movements commanded by the motor controllers do not meet the tolerances set by the central controller, the motor controllers are commanded to correct the position.

In addition to commanding the RF and positioning sub-systems, the central controller is also tasked with controlling the IF and sampling sub-system. The IF sub-system consists of 2 HP signal generators, 2 programmable filters which handle 2 channels each, and a custom IF circuit which performs a single side-band mix down

operation from the IF frequency (50 - 500 MHz) to baseband. The control of these systems is primarily via GPIB interface and digital I/O from an A/D card. Since the parameters of these systems are not changed often, the load on the central controller is minimal.

Control of the environment monitoring sub-system is divided between two sub-controllers. An R.M. Young meteorological station consisting of two anemometers, an air temperature gauge, a humidity sensor, and a rain gauge are controlled with a Kila V80 computer-on-a-board. Data from each of the sensors is averaged for 30 seconds, coded with a time stamp, and transmitted to the main controller where it is stored in an 8 Kbyte buffer until the main controller is free to read the data and store it with the rest of the radar data.

The second portion of the environmental sub-system operates independently of the main controller and consists of a bi-vane wind stress sensor, an eight wire wave gauge array, a water temperature sensor, and two auxiliary radars. The data is recorded at approximately 30 Mbytes/day after compression and is stored on separate 4 mm dat tapes.

Since the radar system is so complex, periodic monitoring, trouble shooting, and fixing is required. Towards this end, the main controller is connected an on shore telephone line with an armored underwater cable. The total cable run is approximately 1.1 km. The main controller has a 9600 baud modem which has no trouble driving the line for this distance. In addition to the main controller, the auxiliary radar controller and an X-10 phone operated switching module controller are connected to the phone line using an off-the-shelf 4 channel fax-modem-phone

switch. This switch answers the phone and can be commanded to ring one of four lines using telephone touch tone signals.

If the X-10 controller is selected, then the power to any of the main systems can be turned off and on over the phone. This is useful for the inevitable reboots needed with the computer controllers. The X-10 modules transmit signals on the AC circuit connecting the equipment. Because of this they are sensitive to noise on the AC circuit generated by some of the equipment (mostly the motor indexers). However, the large capacitive loads of the computer power supplies seemed to adequately filter the noise to maintain the operation of the X-10 modules. This did require some care to be taken in assuring that the computers were not turned off without first turning off the indexers. With the indexers on it was possible to turn off the computers but not turn them back on. Despite this small problem the X-10 modules functioned quite well.

If either the main controller or the auxiliary controller are selected by the fax switch, the designated modem answers the phone and activates a TSR called PC-Anywhere running on the controller. PC-Anywhere momentarily interrupts whatever is running on the controller and attempts to turn over control of the computer to the caller. If the call is from a computer running the correct software, control is handed over to the calling computer and the interrupted program resumes operation. All this occurs with minimal interruption of the radar control program.

Once control has been handed over to the calling computer, trouble shooting, monitoring, and fixes can be effected over the phone, if possible, or the system can be shutdown to wait for a service trip. This simple communication scheme proved

very useful since control could be established from any phone jack using a laptop computer equipped with a modem. This allowed complete testing of the control system before leaving the deployment area.

This combination of custom and off the shelf equipment proved to be an inexpensive, robust and flexible means of controlling a very complicated radar system from over a thousand miles away. The Lake Ontario deployment lasted from the beginning of May to the end of November and required only four on site trips (not including data pick-up, which was performed by the CCIW staff) including setup, maintenance, and take down. Although admittedly "low-tech," this system minimized the required intervention a great deal. Without this remote operation system, deployments of more than a few weeks are very impractical if not impossible.

3.4 Experiment Plan

The experiment plan for the Yscat94 experiment was designed to exploit the system's parametric agility in order to get as much data, under as wide a variety of conditions, as possible. Towards this end the data collection scheme is divided into several "modes," each designed to isolate at least one environmental parameter in the measurement. The modes are designated azimuth scan, wind tracker, and long wave modulation modes.

The azimuth scan mode holds the incidence angle and frequency constant while scanning in 20° increments in azimuth. The return power is recorded for one minute at each point. The objective is to scan the radar's entire azimuthal field of view fast enough that the wind speed and wave field are approximately constant. This mode is designed to determine how the statistics of the radar signal vary with relative wind-look angle.

The wind tracker mode attempts to keep the radar pointed either upwind, downwind, or cross wind (in that order of priority) at all times. Wind direction is determined to be the most previous 20 minute average of the wind direction. The measurement length is one minute. This allows the wind speed dependence to be determined for specific relative azimuths.

The long wave modulation mode is similar to wind tracker except that the record length is twenty minutes. This mode is designed to study the variation of the radar statistics caused by the long wave field.

Each of these modes was run for about 2 days consecutively, then the mode was switched. This means that each mode gets about one third of the total experiment time. In addition to these modes, two X band radars were monitored constantly for the entire deployment period. One radar was pointed at nadir, and the other one was at an incidence angle of 20 degrees.

3.5 Experiment Summary

Data collection began on May 19, 1994 and was concluded on 30 November, 1994. During this time about 5.5 Gbytes of pre-processed radar data, 18 Gbytes of auxiliary data, and about 10 Gbytes of raw unprocessed data files were collected. Because of the length of the deployment, this data covers a wide variety of environmental conditions.

Table 3.2 summarizes the distribution of standard measurements with respect to wind speed. Measurements not included here are long wave modulation mode measurements, measurements contaminated by rain, wind tracker mode measurements which were not at one of the listed frequencies, and measurements ruined by equipment failures.

WS/ Frequency		0-5	5-7.5	7.5-10	> 10
H-Pol	2	4245	1196	516	587
	3	3808	810	388	299
	5	7263	1756	791	806
	10	3739	833	369	308
	14	6775	1763	744	828
V-Pol	2	4315	1502	511	396
	3	4658	1539	555	366
	5	10083	3319	1179	622
	10	6176	2001	636	310
	14	8595	3064	1034	499

Table 3.2: Number of measurements for various wind speed/ frequency conditions.

Fetch varies quite significantly depending on the wind direction (see Fig 3.1). Figure 3.8 shows the wind vector plotted for all H-Pol, 5 GHz measurements. This shows that we experienced a good variety of wind directions and strengths. The notable exception is the lack of even moderate winds from 90 to 180 degrees on Fig.3.8. Although this seems unusual, it agrees with the results of the WAVES'87 experiment (Colton, 1989). Since most of the experiment was conducted during the summer, we generally observed stable boundary layer conditions. Several days were contaminated by rain and were removed from the data set. In general, wave heights were less than 0.5 meters because of the prevailing short fetch (Collyer, 1994).

3.6 Signal Processing Methods

The radar data collected during the Yscat94 experiment was collected by the A/D board as I/Q samples of like- and cross-pole signals. Since this translates into 2000 samples per second on four channels, it is necessary reduce the data rate by pre-processing. The data rate from the radar system was reduced using a covariance spectral estimation technique commonly used in Doppler weather radar (Doviak and Zrnic, 1984). In order to store the Doppler spectra of the signals received by the radar exactly, one needs to store the same number of data points as in the original signal. However, another way of representing the signal is through its spectral moments. The i'th moment of the signal is defined as

$$m_i = \int x^i f(x) dx \tag{3.1}$$

where $f(x)$ is the probability density function of the parameter x. In general, it takes an infinite number of moments to completely describe the data. In radar scattering,

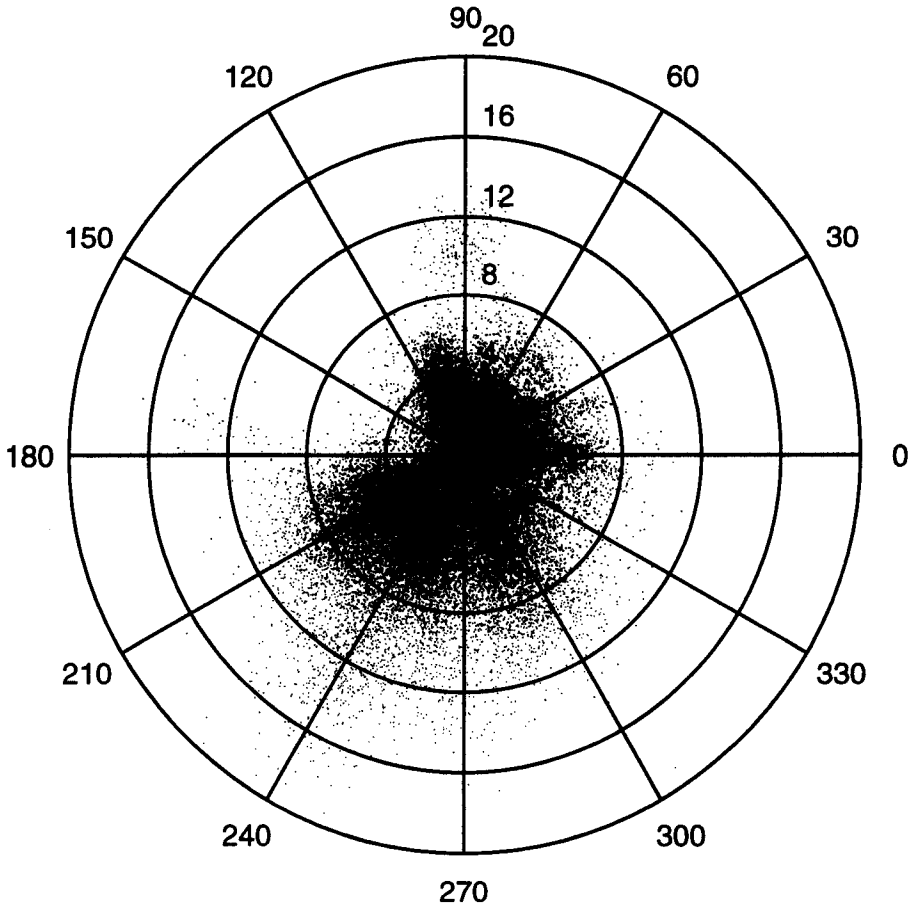

Figure 3.8: Wind vector plot. Radius is wind speed in m/s and angle is in degrees true.

however, a few of these can be considered of much more interest than others. These are:

1. The mean of the return power
2. The centroid of the Doppler spectrum
3. The width of the Doppler spectrum.

The mean power of the radar signal was computed by computing the mean of the squares of the measured voltages at the output of the A/D card, that is:

$$\overline{\sigma} = \frac{1}{N}\sum_{N} x_i^2. \tag{3.2}$$

This is a maximum likelihood estimator with well-known characteristics.

The Doppler centroid and bandwidth were estimated using a covariance estimation procedure. The Doppler centroid is estimated by assuming that the power spectra of the sequence is symmetric about some center frequency $f_\circ$. We can write the Fourier transform of this power spectrum (the autocorrelation, $R(\tau)$, of the time sequence), $P(f)$, in terms of corresponding spectrum centered at $f_\circ = 0$, $P_c(f)$ by

$$R(\tau) = \mathcal{F}[P(f)] = e^{i2\pi f_\circ \tau}\mathcal{F}[P_c(f)]. \tag{3.3}$$

If $P(f)$ is symmetric about $f_\circ$ then the transform of $P_c(f)$ will be real. Therefore we can estimate the centroid of $P(f)$ by computing the phase of the autocorrelation of the time sequence. Following this reasoning, the Doppler centroid is given by

$$f_\circ = \frac{arg(R(\tau))}{2\pi\tau}. \tag{3.4}$$

The Doppler bandwidth is estimated by assuming that the true spectrum is Gaussian shaped, and noting that the normalized correlation function corresponding to a Gaussian with a variance β^2 is

$$\rho_{Guassian}(\tau) = e^{-2(\pi\beta\tau)^2}. \tag{3.5}$$

Using this relation, we can easily solve for the variance, β, given the correlation function evaluated at a known lag. For the Yscat radar system, the correlation function was estimated at a lag of one sample $[R(1)]$using

$$R(1) = \frac{1}{M}\sum x^*(m)x(m+1). \tag{3.6}$$

The applicability of this technique in ocean scattering applications has been examined by other researchers (Jessup, 1990). In short, it has been found that this method accurately estimates the first moment of typical Doppler spectra obtained from CW radar scattered from the sea surface, while slightly underestimating the true bandwidth. However, it is judged to be a good compromise between speed, accuracy, cost, and data volume.

3.6.1 Data Editing

In a field experiment such as the Yscat94 experiment, where data is collected constantly over a 6 month period, some of the data is bound to be collected under less than optimal conditions. Because of this some of the data must be discarded. Care must be taken, though, to ensure that data is not rejected without reason. Reasons for rejecting Yscat data fall into two categories:

1. Radar system failures

2. Environmental anomalies.

Several times during the experiment, some portion of the radar system failed and caused some of the data to be rejected. These include RF signal generator failures, motor indexer failures, weather station failures, and human errors (e.g., painters standing in front of the radar). These failures were recorded in a log book and were subsequently removed from data set.

Certain environmental conditions can also give cause to discard data. Rain strongly effects the radar return by changing the characteristics of the radar antenna and cables by getting them wet, changing propagation characteristics of the transmit medium, and by changing the water surface by splashing. The general effect is to increase low wind speed radar returns by causing splashing, and decreasing high wind speed returns by damping the surface waves. Rain data was collected by the weather station and stored in the data files. Therefore, rain–contaminated data is easily detected and removed form the data set.

The effect of having a wet radar system was avoided by also removing data for several hours after significant rain storms. Other environmental anomalies include rapidly changing wind conditions, such as wind speed and direction. Rapidly changing wind direction occurs very often at low wind speeds, and more rarely at higher wind speeds. The small Bragg scattering waves respond very quickly to changes in the wind direction and so can be used to detect changing wind. This is done by requiring that the Doppler shift of the return signal be above a small threshold. This helps to eliminate confused seas when the waves are not traveling with the wind.

Chapter 4

POWER DISTRIBUTIONS

4.1 Introduction

The distribution of the radar return scattered from the water's surface depends on the scattering mechanisms involved. The central limit theorem suggests that if the radar foot print is large, the distribution will be normal and only the mean will depend on the specific scatterers. Radar returns from spaceborne scatterometers have been found to follow this distribution precisely. However, for small foot print radars, the situation is much more complicated. In fact, the distribution of the radar return is completely dependent on the scatterers involved.

Because of cost and time considerations, small earth based radars have been used to study ocean radar scattering. The smaller foot prints of these radar systems are on the order of the coherence area of the water surface and so allow the study of the cross section distributions. However, there is no unanimous consensus as to what the observed radar cross section distribution is or should be. Various distributions have been proposed on both theoretical and empirical grounds. Some of the distributions include Weibull, log–normal, Rayleigh, K, and two-component Weibull distributions (Gotwols and Thompson, 1994). The varying results suggest the need for further study in this area.

One important reason for studying the distribution of the radar return is because current ocean scattering theory does not accurately predict the observed mean radar cross section. Although understanding the mean radar cross section is the

ultimate goal of space based scatterometer applications, the scattering model should also predict the complete distribution of the observed cross section.

Part of the problem in developing a model of the mean radar cross an incomplete understanding of the mechanisms involved in the scattering. The basic composite scattering model proposes that the radar cross section at moderate incidence angles is dominated by the Bragg resonant result given by small perturbation theory. Additional scattering mechanisms that have been proposed are breaking waves and wedge scattering. If these additional scattering mechanisms are contributing significantly to the mean radar cross section it is likely that the distribution of the radar return will be different than that predicted by the composite model in ways other than simply the mean.

Therefore, this chapter considers the distribution of the radar cross section in terms of the composite model in order to see if the statistics of this distribution agree with those predicted by the composite model. The first section considers the background and theory which is used to predict what the cross section distributions should be. Along with this a simple model of the scattering distributions is presented and a simulation technique is outlined. The second section describes the technique used to analyze the empirical data in light of the simple model, and the empirical results are presented. The third section compares the simulation and the empirical results. The last section presents some conclusions that can be drawn from the results of this analysis.

4.2 Background and Theory

As stated in the introduction there has been significant work, both theoretical and empirical, in studying the mean of the radar cross section of the sea

surface. Although there are many unknown variables in scattering models, the general consensus is that they under predict the radar cross section of the water surface (Plant, 1986; Donelan and Pierson, 1987; Colton, 1989).

Studies of the whole distribution have been limited and have reported differing results. That the distribution was not Rayleigh was determined early using analysis of variance techniques (Trunk, 1972). Since then, empirical analysis of the distribution has been limited by the availability of scatterometer data. A notable exception is the data resulting from the SAXON experiments which has yielded useful models of the amplitude distribution of Ku and X band radar returns (Gotwols and Thompson, 1994). This data showed that for the footprints sizes in the SAXON experiment, the amplitude returns were Rayleigh distributed in accordance with the central limit theorem. The authors did suggest, however, that a radar with a footprint on the order of the size of Yscat's might be able to avoid the central limit theorem effects. There has not been a comprehensive analysis of empirical data covering the complete range of radar parameters, with a comparison to the composite model.

4.2.1 Theory and Probability

In order to compare the empirical data generated by the Yscat94 experiment with scattering theory, it is necessary to develop a simple scattering model from which to draw conclusions about theoretical statistics of the radar cross section. As will be seen, the theoretical characteristics of the radar return is different for large footprint radars such as satellite borne radars, and the small foot print radars which are typically associated with field experiments. This section presents the issues pertinent to both the large footprint and small footprint radars. A simple model which

predicts the observed radar cross section distribution based on the composite model is presented and a simulation technique is outlined.

Large footprint radars

The distributions of the radar return from radar systems which illuminate large regions of the sea surface are governed by the familiar radar concepts of Rayleigh fading and the central limit theorem. Extensive discussions of Rayleigh fading and the central limit theorem are found in may textbooks on radar systems and statistics. Notable are (Ulaby, 1983) and (Papoulis, 1991) from which this short review is drawn.

When coherent microwave radiation is scattered from a large, essentially random surface, such as the sea surface, the return is governed by the central limit theorem (CLT). Since the surface is uncorrelated over large distances, the return radiation will be the sum of the fields scattered from many independent regions. The CLT suggests then, that the real and imaginary parts of the scattered EM field will be normally distributed. Furthermore, because of the random nature of the surface, the phase of the return radiation will be uniformly distributed between 0 and 2π.

The resulting distribution of the radiation is a jointly normal distribution in the real and imaginary components of the fields. A typical radar system employs either a linear detector or a square law detector. A linear detector detects the envelope of the return fields. The fundamental theorem of statistics says that the distribution of a random variable, Z, which is related to two independent, normally distributed random variables, X and Y, by the equation

$$Z = \sqrt{X^2 + Y^2} \tag{4.1}$$

will be Rayleigh distributed. That is, if X and Y's distribution are given by

$$f_X(x) = \frac{1}{\sqrt{2\pi}\sigma_x} e^{-\frac{x}{2\sigma_x^2}} \tag{4.2}$$

then the distribution of the envelope (Z) will given by

$$f_Z(z) = \frac{z}{\sigma_x} e^{-\frac{z^2}{\sigma_x^2}}. \tag{4.3}$$

If a square law detector is used (whose output is proportional to the power at its input $W = Z^2$), the fundamental theorem can again be applied to find that the output power is exponentially distributed i.e.,

$$f_W(w) = \frac{1}{2\sigma_x} e^{-\frac{w}{2\sigma_x}} \tag{4.4}$$

Unfortunately, the resulting is a wildly fluctuating signal even in the absence of additional noise. The ratio of the square of the mean to the variance of this distribution is always 1 (0 dB).

Since this is inherent to the system, one typically employs a low pass filter to reduce this signal fluctuation. Essentially an integrator, the low pass filter performs the function of averaging independent samples of the output together. The resulting output again tends to a normal distribution as the integration time includes more and more independent samples. For the square law detector, the output distribution is a chi-square which tends to a normal distribution very slowly and is given by

$$\chi^2(n, x) = \frac{1}{2^{\frac{n}{2}}\Gamma(\frac{n}{2})} x^{\frac{n}{2}} e^{-\frac{x}{2}} \tag{4.5}$$

where n is the degrees of freedom. The exponential distribution is a $\chi^2(2)$ distribution. It can be shown that the sum of N independent variables with $\chi^2(2)$ distributions is $\chi^2(2N)$ distributed (Ulaby, 1983). This is illustrated in Fig. 4.1 which shows

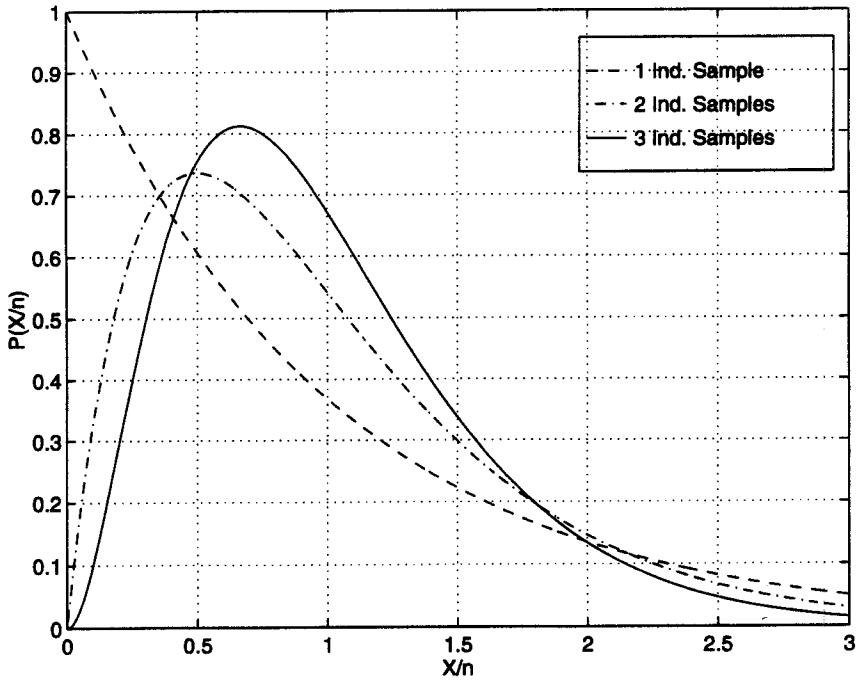

Figure 4.1: Probability distributions of the sum of independent exponential distributed RV's. Note that the distribution converges very slowly to a normal. Shown are $\chi^2(2)$,$\chi^2(4)$,and $\chi^2(6)$ corresponding to 1,2, and 3 independent samples.

$\chi^2(2N)$ for various values of N (the number of independent samples). Therefore, the shape of the distribution of the output of such a system depends on the number of independent samples in the integration time, or roughly, the correlation time of the scattered fields.

Small footprint radars

For small footprint radars, the shape of the distribution depends much more on the scattering mechanism than it does for the large footprint radar. For a system like the Yscat radar, the antenna footprint is on the order of a "coherence area" or the typical size over which the surface scatterers are correlated. Because of

this the central limit theorem cannot be applied and we need a model of the scattering mechanism in order to determine the distribution of the cross section measurements.

The most popular scattering model for ocean scattering is the composite model. This model proposes that the water surface is composed of small independent "patches" whose individual cross sections are given by small perturbation theory, i.e.,

$$\sigma_\circ = 16\pi k_m^4 |g_i(\theta)|^2 \Psi(2k_m \sin\theta) \tag{4.6}$$

where $\sigma_\circ$ is the cross section, k_m is the microwave number, g_i is a reflection coefficient, θ is the local incidence angle, and Ψ is the wave height spectral density (Wright, 1966). Each of these small patches is tilted by any underlying long waves or swell which changes its cross section by changing the apparent incidence angle. Therefore the distribution of $\sigma_\circ$ is strongly influenced by the distribution of the wave slopes.

The total cross section is the sum of the cross section of the individual patches illuminated by the antenna footprint. If the distribution of the cross section, $\sigma_\circ$, at a given slope, s, is given by $f(\sigma_\circ|s)$ then the distribution of the cross section measured by the radar is

$$f(\sigma_\circ) = \int f(\sigma_\circ|s) f(s) ds \tag{4.7}$$

where $f(s)$ is the distribution of the slopes (Trunk, 1972). This integral can be simplified if we assume that the distribution $f(\sigma_\circ|s)$ is replaced with a functional relationship, $\sigma_\circ(s)$. In this case the distribution of the cross section is found by using a fundamental theorem of statistical distributions

$$f_\Sigma(\sigma_\circ) = \sum_i \frac{f_S(s_i)}{|g'(s_i)|} \tag{4.8}$$

where $f_\Sigma(s)$ is the cross section distribution, $f_S(\sigma_\circ)$ is the slope distribution, $\sigma_\circ = g(s)$ is the slope dependence of the cross section, and the s_i's are the roots of the slope dependence.

For the relationship given in Eq. (4.6), we need equations for the reflection coefficient, $g_i(\theta)$, the wave height spectrum, $\Psi(2k_m \sin\theta)$, and the distribution of the incidence angles or, equivalently, the slopes. The reflection coefficients are given by small perturbation theory as (Plant, 1986)

$$g_v(\theta) = \frac{\cos^4\theta(1+\sin^2\theta)^2}{(\cos\theta + 0.111)^4} \tag{4.9}$$

and

$$g_h(\theta) = \frac{\cos^4\theta}{(0.111\cos\theta + 1)^4}. \tag{4.10}$$

In this representation, an empirical value for the permittivity of the water ($81\epsilon_0$) has been used. It has been shown that this value more closely follows the wave tank observed reflection coefficients than the commonly used assumption that water is a perfect conductor.

The wave height spectrum is the subject of some debate as was discussed in the introduction; however, empirical forms are available which have been developed from wave staff data. One particularly suited to this case is the Donelan spectrum. The Donelan spectrum was developed using wave staff data collected on the same research tower on which the Yscat94 experiment was conducted.

According to Donelan et al (1985) the frequency spectrum of the surface can be expressed as

$$\Phi(\omega) = \alpha g^2 \frac{\omega^{-4}}{\omega_p} e^{-\frac{\omega_p}{\omega}} \gamma^\Gamma \tag{4.11}$$

$$\Gamma = e^{-(\omega-\omega_p)^2/2\sigma^2\omega_p^2} \tag{4.12}$$

where the various parameters are:

- ω_p is the spectral peak;
- α is the equilibrium range parameter;
- γ is the peak enhancement factor;
- σ is the peak width factor.

The parameter α is given by

$$\alpha = 0.006(U\cos\theta/c_p)^{0.55} \tag{4.13}$$

where U is the wind speed and c_p is the phase velocity of the peak frequency wave. The peak enhancement factor (γ) is given by:

$$\gamma = 1.7 + 6\ln(U/c_p) \tag{4.14}$$

for U_c/c_p 1, and 1.7 otherwise. The peak width parameter is given by

$$\sigma = 0.08\left(1 + \frac{4}{(U\cos\theta/c_p)^3}\right) \tag{4.15}$$

and the ratio U/c_p is given by:

$$U\cos\theta/c_p = 11.6\tilde{x}^{-0.23} \tag{4.16}$$

where $\tilde{x}$ is the non-dimensional fetch.

The fetch (the distance over which the wind blows over the water) varies significantly on Lake Ontario, as can be seen from Fig. 3.1. However, as Fig. 4.2 shows, the fetch encountered for up and downwind measurements (roughly north and south) the fetch varies from about 18 km to 1 km. Assuming that the directions are

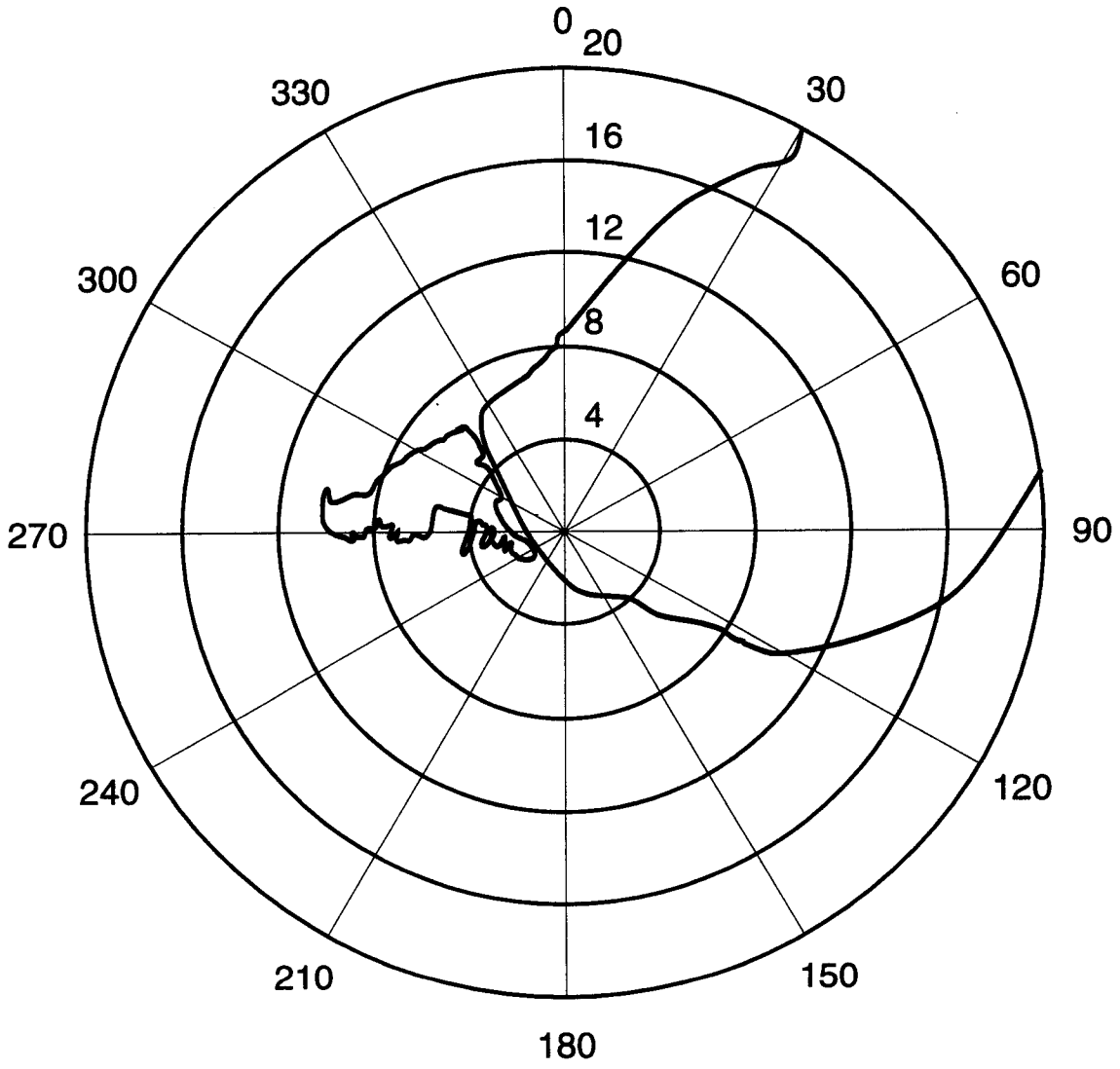

Figure 4.2: This map shows the experiment location at the center of the grid. The bold line denotes the shoreline of Lake Ontario. Angle is shown in degrees true, distance scale is in kilometers. For both upwind and downwind models, unless otherwise noted, the fetch used was 6 km.

fairly uniformly distributed, the fetch used in this model is 6 km unless otherwise noted.

Equations (4.9), (4.10), and (4.12) can be used in Eq. (4.6) to define the function which relates local incidence angle to observed cross section, $\sigma(\theta)$. This relationship is known to breakdown in the region below about 15 degrees incidence angle. This is a transition region between Bragg scattering and specular scattering. In scattering models this is usually referred to as the quasi-specular component and is found via physical optics (Durden and Vesecky, 1985). Since the focus of this study is on the composite model, the effect of this quasi-specular is modeled by "soft-limiting" the Bragg scattering component to 10 dB. This relationship is shown in Fig. 4.3.

The exact distribution of the slopes is unknown; however many researchers have shown that the long, swell-type wave slopes are well approximated by a normal distribution (Gotwols and Thompson, 1994). As was stated in Chapter 2 , the exact meaning of slope in the context of a scatterometer and the composite model needs to be defined. In the composite model the slope is supposed to be the local slope of an underlying wave. However, this assumes two distinct scales of waves, ones that are very long compared to the antenna footprint (those that tilt the surface) and some that are very short compared to the antenna footprint (the Bragg waves). In reality though there is a continuum like that described by Eq. (4.12).

For the Yscat radar system the typical antenna footprint is about 2/3 m long. So for practical purposes, waves on the order of 1 m and larger will appear as a time-varying tilt of the surface. Therefore, it is reasonable to include in the spectrum of Eq. (4.12) only those wavelengths longer than 1 m.

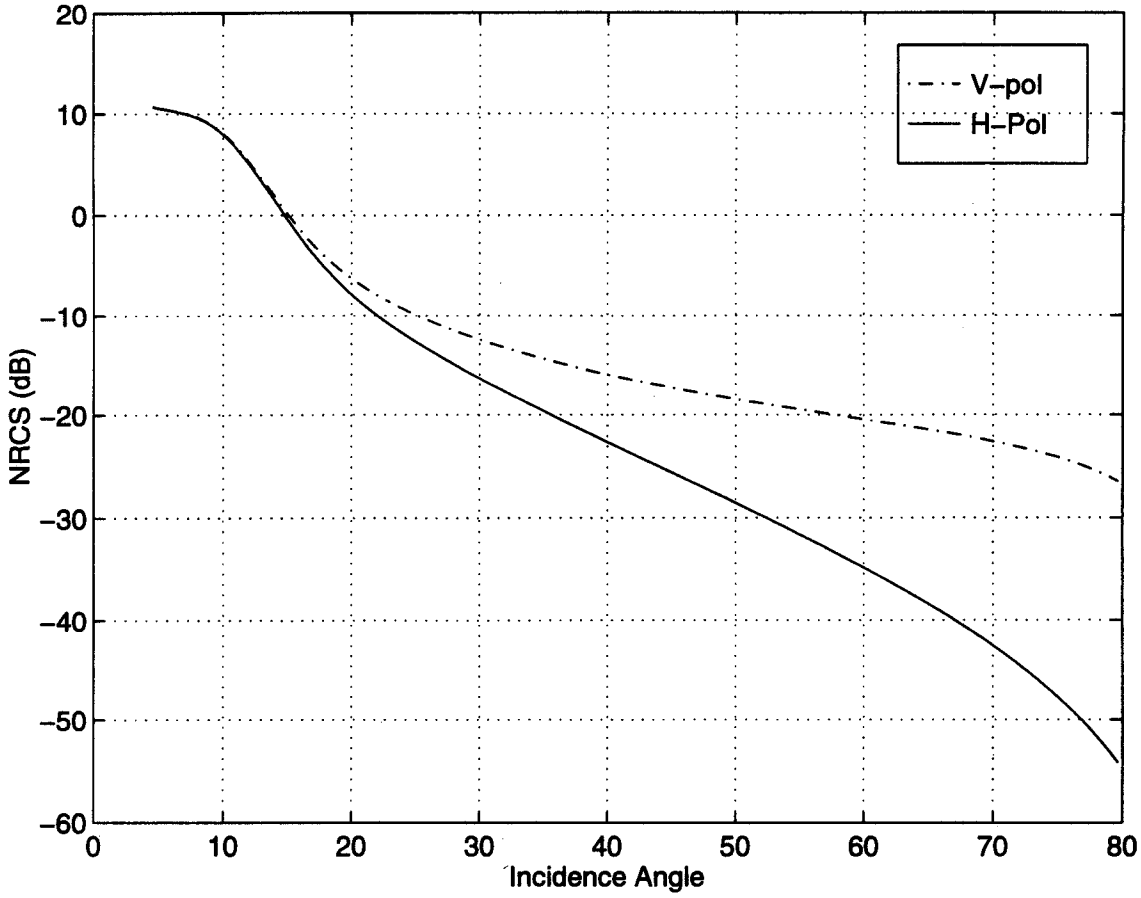

Figure 4.3: Dependence of cross section on incidence angle. Shown here is the case for 14 GHz, wind speed 8 m/s utilizing the Donelan spectrum with a 9km fetch.

For the simulations in this material, the slope is calculated as the first order fit to a stochastic realization of a 2/3 meter-sized water surface. A realization of the surface is generated by summing the different Fourier components of the surface with magnitudes given by Eq. (4.12) and phases that are uniformly distributed.

Obviously, the validity of using a linear fit over 2/3 m to calculated the slope of a surface with component wavelengths as small as 1 m needs some justification. Qualitatively, when the wind speed is low, the wave amplitudes, and therefore the slopes, are very small. As a result, the error incurred by using the linear fit is small. As the wind speed increases, the dominant wavelength increases rather quickly so that by the time the waves are large enough to create significant slopes, the dominant wavelengths are much longer than 1 m.

As a check, however, we can calculate the coefficient of determination from the linear regression used to calculate the slopes. The coefficient of determination is defined as

$$R^2 = \frac{\sum(\hat{y} - \bar{y})^2}{\sum(y - \bar{y})^2} \tag{4.17}$$

where $\hat{y}$ is the function estimated using the regression and $\bar{y}$ is the mean value of the data. This is a measure of how much of the variation in the data is accounted for by the regression. The average value of R^2 for each wind speed is shown in Fig. 4.4 along with the standard deviation calculated from the 600 slope estimates. The typical values of R^2 are around 0.8. This seems to justify this method of defining the local slope of the surface.

The distribution of the slopes may now be calculated with some confidence using the technique described above. This is accomplished by forming a realization of the sea surface, and then letting the various spectral components propagate through

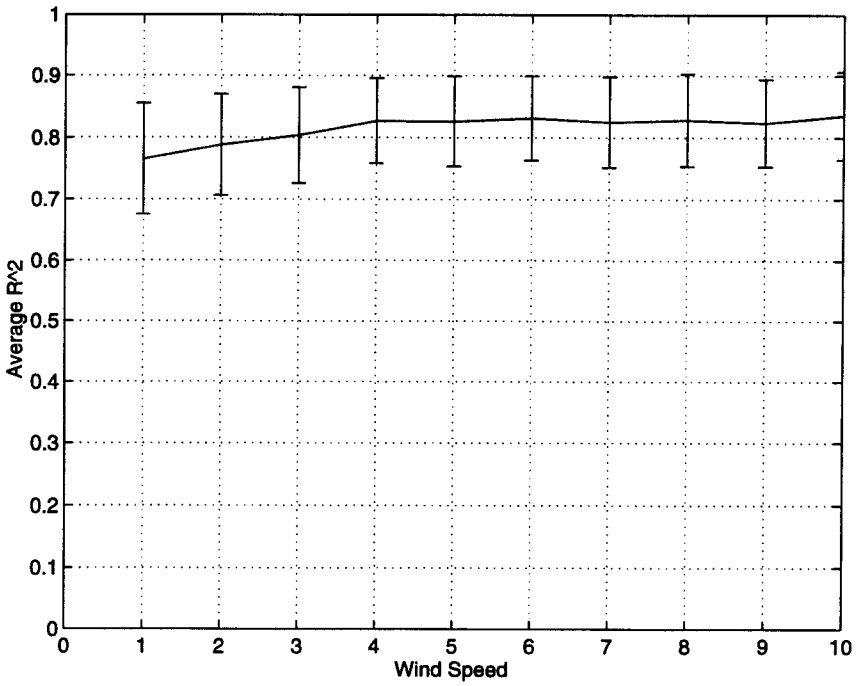

Figure 4.4: The coefficient of determination for the slope estimates of the Donelan spectrum as described in the text. Values near 1 indicate that the slope estimation technique described in this section provide a good characterization of the surface.

the antenna footprint according to the dispersion relation for water waves. A realization is generated by forming a surface with a spectrum given by Eq. (4.12) with a uniformly distributed phase. The slopes are calculated at 1/10 second intervals for 600 measurements. This corresponds to the 1 minute measurements made by the Yscat radar.

The slope distributions derived in this manner from the Donelan spectrum are shown for 3 and 9 m/s in Fig. 4.5. These distributions slope distributions from 400 independent realizations of the surface. Note that the distributions appear normal. The "normality" of the slope distributions may be quantified by measuring the coefficient of kurtosis, ξ, where

$$\xi = \frac{\mu_4}{\mu_2^2} - 3 \tag{4.18}$$

and the μ_i's are the ith moments of the distribution. This coefficient is 0 for normal distributions (mesokurtic), negative for distributions less peaked than the normal (platykurtic), and positive for distributions distributions that are more peaked (leptokurtic). The coefficients of kurtosis for the distributions shown in Fig. 4.5 are less than 0.01 for both 3 m/s wind speed and 9 m/s wind speed. Figure 4.6 shows the coefficient of kurtosis for the simulation distributions as a function of all wind speeds. These values correspond to the average values obtained in 10 realizations of the sea surface at each wind speed. The rather low values of this coefficient indicate that a normal is a good (or at least justified) approximation for the distribution of the wave slopes.

In Fig. 4.3, it is clear that for mid–range incidence angles, the dependence can be well approximated over small incidence angle ranges by a linear fit (in log space). In other words, if the range of incidence angle variation is small, the rather

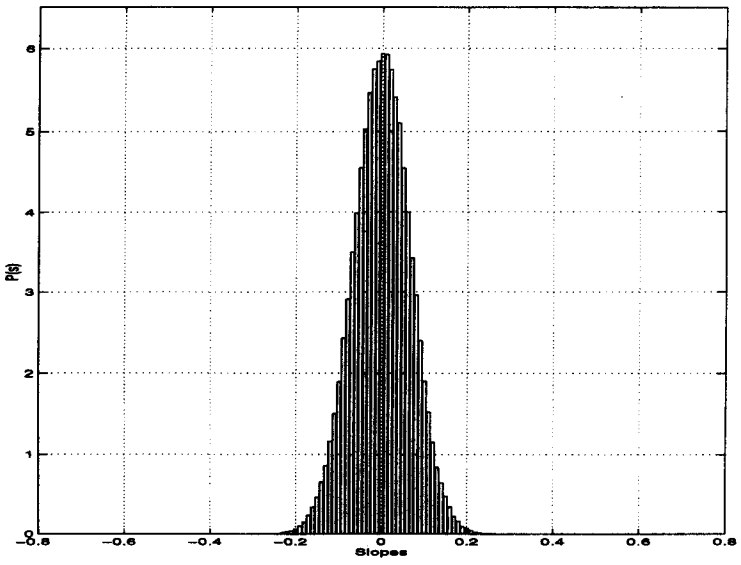

(a) 3 m/s

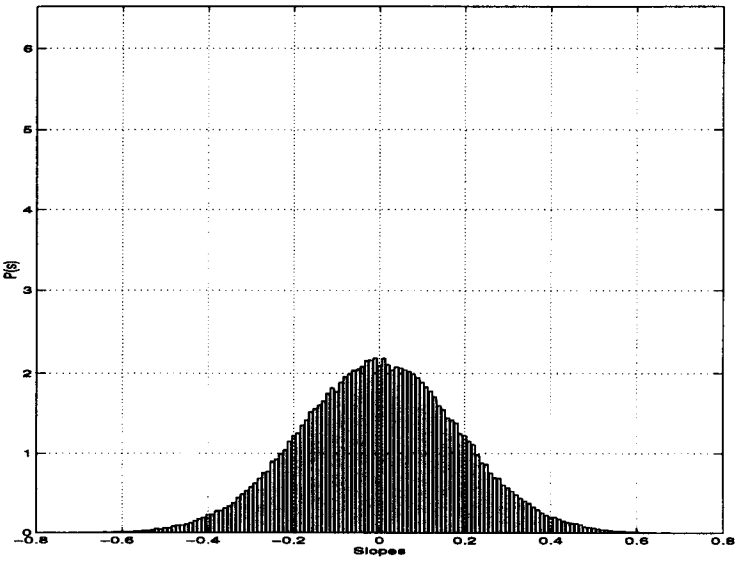

(b) 9 m/s

Figure 4.5: Distribution of slopes from Donelan spectrum. Each histogram corresponds to 400 independent realizations of the surface for wind speeds of (a) 3 m/s and (b) 9 m/s.

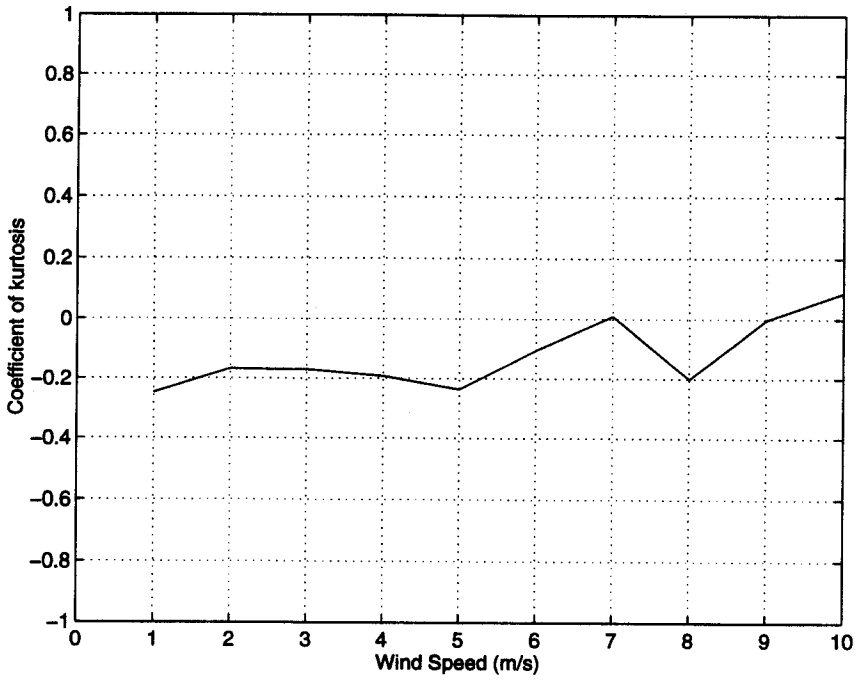

Figure 4.6: Coefficients of kurtosis for the simulation spectrum. The relatively low values indicate that the simulated slope distributions are well approximated by a normal distribution.

complicated expression in Eqs. (4.6) thru (4.10) can be well approximated with an expression of the form

$$\sigma_o = Ae^{m\theta}. \tag{4.19}$$

The validity of the assumption that the incidence angle variation is small varies with wind speed. The approximate range of incidence angles encountered under normal conditions is on the order of ±10 degrees (Colton, 1989), depending on wind speed. Figure 4.7 shows the distribution of incidence angles from the simulation for a wind speed of 9 m/s. Obviously, the significance of this depends on the application and the

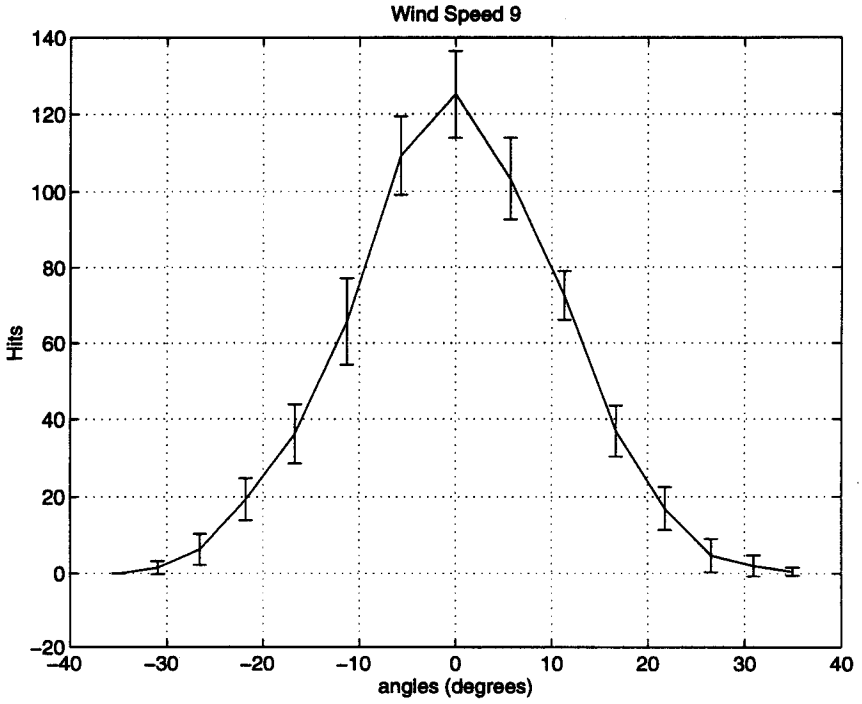

Figure 4.7: Histogram of simulated incidence angles at 9 m/s wind speeds for Lake Ontario. Note that at high wind speeds, very steep slopes may be observed, albeit quite infrequently.

radar parameters. This will be discussed more in the results section of this chapter.

Given this simpler relationship in Eq. (4.19) one may easily calculate the distribution of the cross section. If the distribution of the slopes is normal and given by

$$f(x) = \frac{1}{\sqrt{2\pi s^2}} e^{\frac{-(x-s_m)^2}{2s^2}} \tag{4.20}$$

where s^2 is the variance of the observed slopes and s_m is the mean of the slopes (usually zero) then the distribution of the observed power will be given by

$$\frac{1}{m\sigma_o\sqrt{2\pi s^2}} e^{\frac{-(\ln\sigma_o - \ln A)^2)}{2m^2 s^2}} \tag{4.21}$$

which is a log-normal distribution. This result has been noted by previous researchers who suggested that the very straight slope dependence of the H-pol cross section dependence implies that a log-normal distribution will be observed under proper conditions (Gotwols and Thompson, 1994). However, as long as the range of incidence angles observed is small, the incidence angle variation of both pols may be approximated by exponentials of the form in Eq. (4.19) and, hence, the distributions of both polarizations should approximate a log-normal.

A more exact prediction of the cross section distribution can be determined using the model described above by numerically simulating the sea surface and calculating the cross section. The slopes that are calculated using the algorithm described above may be used to calculate the observed radar cross section using Eq. (4.6). By adjusting the parameters of the simulation, a time series of cross sections can be generated which correspond to the Yscat94 measurements for various environmental and radar parameters. The resulting time series may be processed using the same algorithm as was used for the empirical data to compare the simulation results with the Yscat94 data.

By way of a summary, a simple model for the cross section distribution has been presented which is based on the composite scattering model. The assumptions of the model are that the range of incidence angles that are observed is small and that relationship between slope and cross section given by the small perturbation result in Eq.4.6, can be adequately approximated as an exponential. A simulation technique was also outlined which will be used to compare the observed radar data with the model described in this section.

4.3 Empirical Results

The large data set obtained during the Yscat94 experiment provides a good basis for determining what the distribution of the radar return is. In this section the techniques for determining the distributions observed by Yscat are outlined, log-normals are fit to each distribution, and the quality of the fit is discussed. The results of the estimation are presented and compared to the model.

4.3.1 Fitting the Distributions

In the previous section, theoretical observations were made which indicated that the observed radar cross section distributions should be approximately log-normal. The large data set collected during the Yscat94 experiment provide a good basis for determining what the distributions really are. To do this, two distributions families were selected as candidates for the empirical distributions to see which one best fits the data. The log-normal and Weibull were chosen based on previous research. The log-normal was chosen as a result of the previous section. The Weibull was chosen because of its generality, and because it has been proposed by other researchers (Trizna, 1991). Although the K distribution has been proposed by some

researchers (Jakeman and Pusey, 1976), it was not used here because it is difficult to work with and is difficult to relate to physical parameters.

In order to determine which distribution "best" fits the data, the data was separated according to wind speed, wind direction, frequency, incidence angle, and polarization. Then, histograms for each measurement were computed using 0.5 dB bins centered on the mean return power. Therefore, each histogram consists of 600 individual measurements. This corresponds to one minutes worth of 1/10 second power measurements made in a typical measurement. A sample histogram from a single measurement is shown in Fig. 4.8.

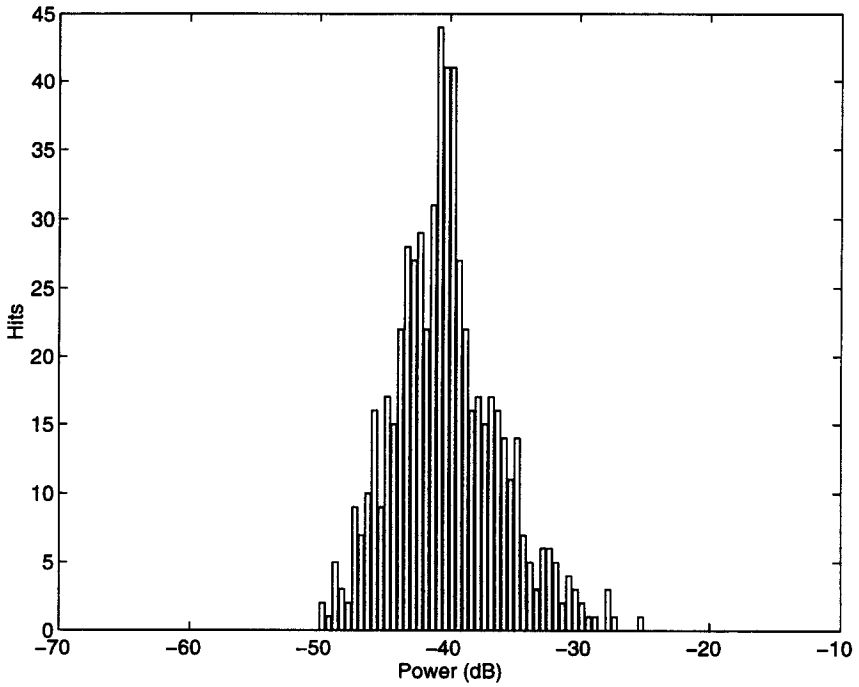

Figure 4.8: Sample histogram of a single measurement. This is from a single measurement set taken at 14 Ghz, upwind, 40 degrees incidence, 8 m/s winds, and H-pol polarization.

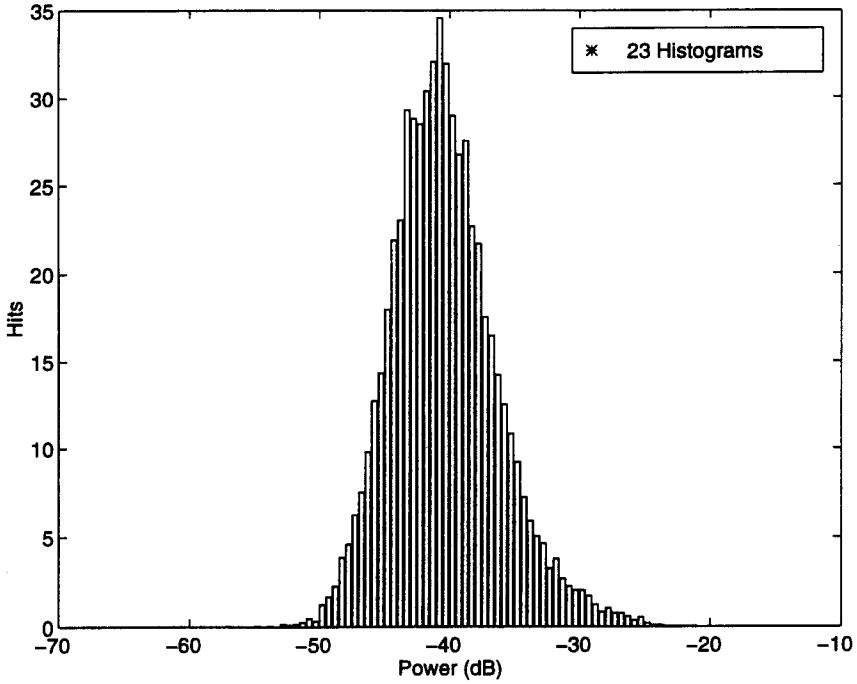

Figure 4.9: Average histogram of all measurements corresponding to the measurements in Fig. 4.8. The average histogram is calculated by normalizing the means of the individual histograms and averaging the bins.

Once the individual histograms have been computed, all of the histograms which correspond to the same measurement parameters are averaged together to estimate the average histogram. Since we are looking for the average shape of the distribution, the mean of each distribution was normalized to the same value. Each bin was then averaged together. The average value of all the individual means was added back in. This was done to minimize the effects of mean changes on the shape estimation. Such changes may be due to slow changes in system gain or other parameters which aren't relevant to the shape of the distribution. In the case of Fig. 4.9, 23 individual histograms were averaged together.

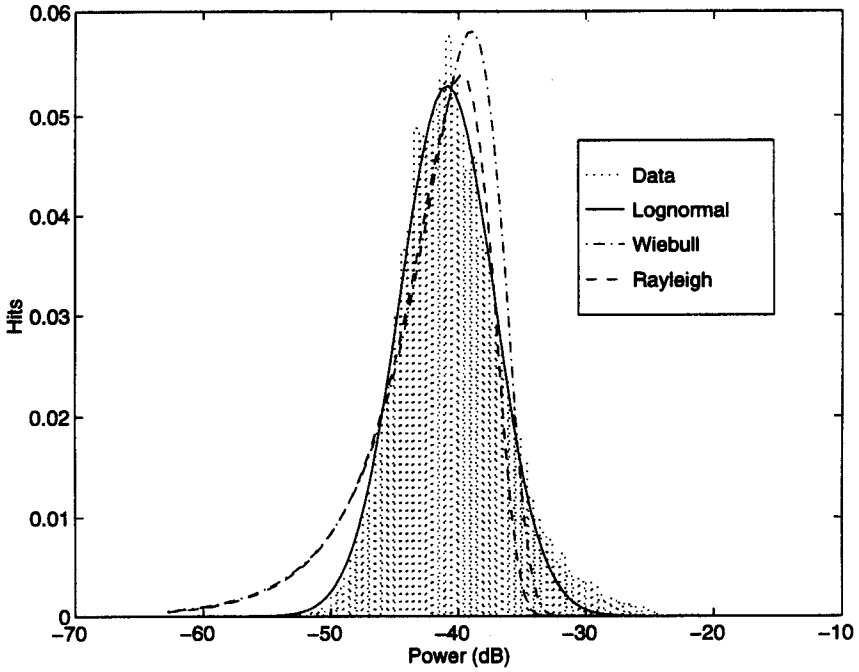

Figure 4.10: This plot shows the average histogram in Fig. 4.9 with the fitted distributions superimposed.

Once the average histogram is calculated, the distribution is found by normalizing the histogram so its area equals 1. The resulting distribution is compared to the common distributions mentioned above by finding the distribution from the particular family in question that minimizes the L2 norm between the empirical and the theoretical distributions. The L2 norm is given by

$$L2_{err}(f(x), g(x)) = \int (f(x) - g(x))^2 dx. \tag{4.22}$$

Figure 4.10 shows the log-normal, Rayleigh, and Weibull fits to the data in Fig. 4.9 which are optimal in their respective families.

All of the Yscat94 data was processed in the manner described above. The residual error of the different fits are shown in Fig. 4.11. The lower pair of lines in each plot correspond to the error of the log-normal fit and the upper pair are those of

the Weibull fit. The Rayleigh fitting errors are not shown since they are special cases of the Weibull and therefore always have worse fitting error than the more general distribution.

Although this error criteria gives a measure of the relative fits of the two distributions, it does not indicate how good the log-normal fit is in an absolute sense. To get an absolute measure of fit, one can calculate the ratio of the power in the empirical distribution to that of the fitted distribution. The number varies from 0.75 to 1.8, but is usually near 1. The average ratio for all the distributions is 1.02 with a standard deviation of 0.18. The distribution of the ratios is shown in Fig. 4.12 and suggests that the log-normal is indeed a good fit for most of the empirical histograms. The outliers in the upper tail of the histogram correspond to cases where there were relatively few measurements.

It is obvious that the distribution in Fig. 4.10 has more of an upper tail than the log-normal. In fact, this is fairly typical of the Yscat94 data. It might be argued that a better fit might be obtained by using a log-Rayleigh or log-chi square type of a distribution. However, the log-normal is retained because (1) the error is small, (2) it can be easily related to physical parameters, and (3) it is supported by the theory outlined previously.

The general conclusion to be drawn from the fitting error data is that the log-normal distribution provides a much better fit than the Weibull under the criteria described above. This is not completely surprising since the trend for the radar return distribution towards a Rayleigh-like distribution is valid only when the received E-field is scattered from many independent regions. This occurs when the antenna illumination pattern is very large. The configuration of the tower mounted

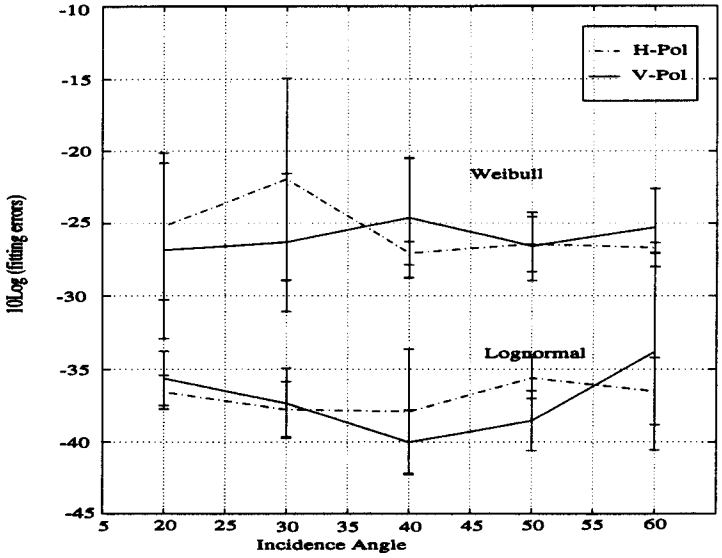

(a) Upwind

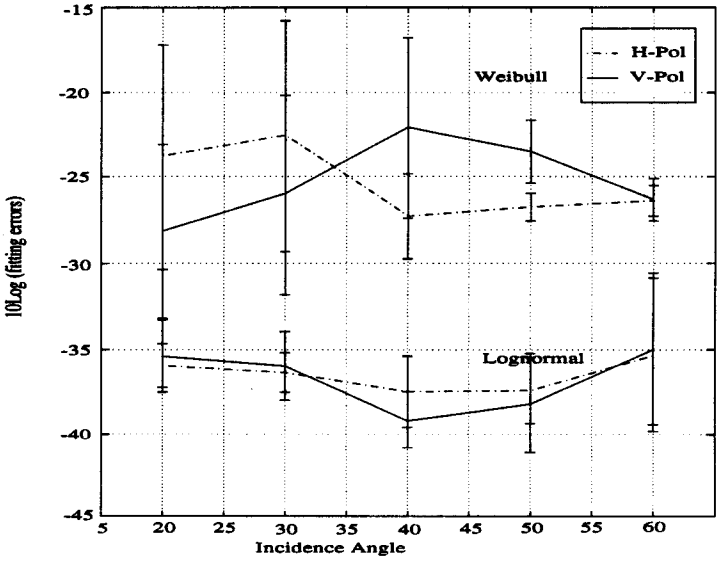

(b) Downwind

Figure 4.11: Average fitting errors for the upwind and down wind measurements. The upper pair of lines are the errors for the Wiebull fits and the lower pair of lines are the errors for the log-normal fits. Note that the log-normal distributions are much better fits according to the error criteria in the text. Errors have been averaged over all wind speeds and frequencies.

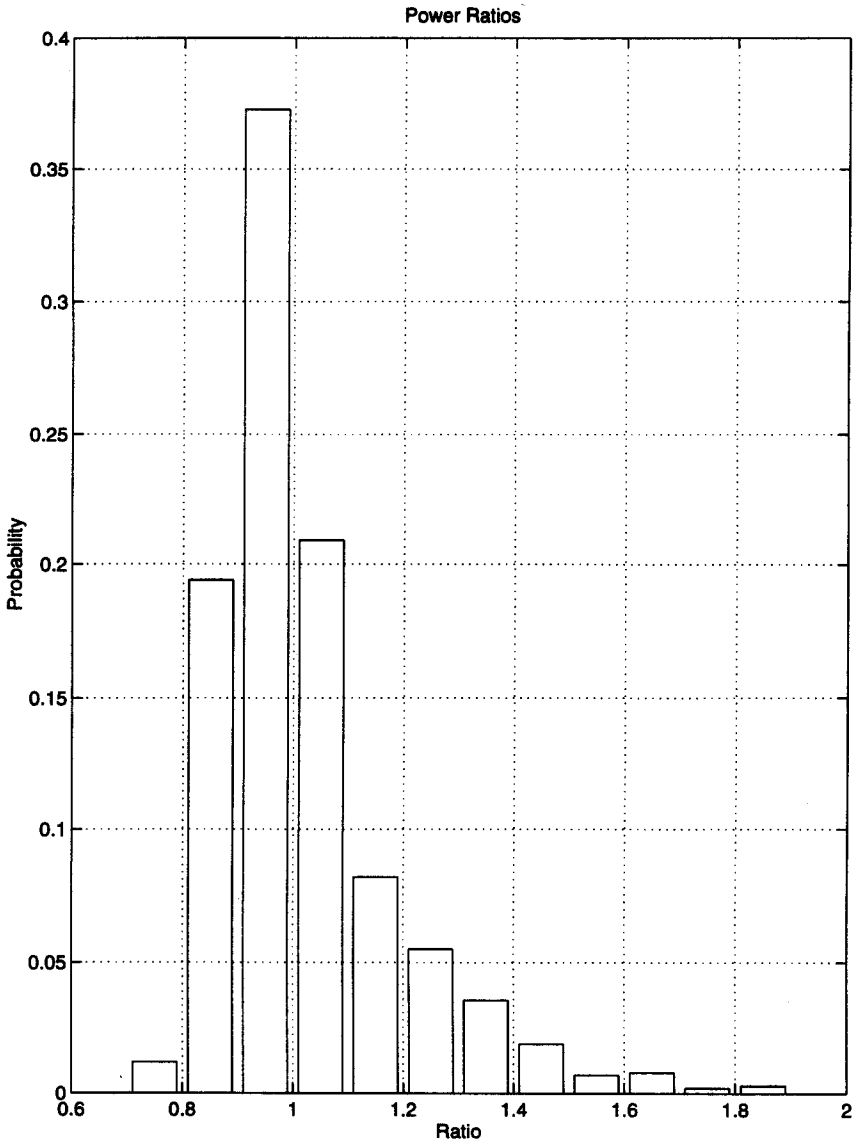

Figure 4.12: Histogram of the quality of fits of the log-normal distributions fit to the empirical data for all cases. The x axis is the ratio of the power in the empirical distribution to the log-normal fits.

Yscat radar provides illumination patterns on the order of a typical coherence region and so has fewer independent regions and a different distribution.

These results provide some validation for the model presented in the previous section. Further validation may be found by comparing the results of the simulations which were described above.

4.3.2 The Distributions

The empirical distributions can show the evolution of the radar return distributions with wind speed. An example is shown in Fig. 4.13 which shows the histograms drawn in a waterfall plot against wind speed. Beneath each waterfall plot is a contour plot of the same thing which show the change in the distributions with wind speed and incidence angle.

It is apparent in Fig. 4.13 is that it is difficult to extract information directly from the true histogram. Thus it is useful to have these distributions parameterized. Since the log-normal describes the distributions well, the distribution parameters obtained from the fits can be used to observe the evolution of the distributions. The fitted distributions are of the form

$$f(x) = \frac{1}{\sqrt{2\pi\sigma_L^2}} e^{-\frac{(\ln x - x_m)^2}{2\sigma_L}}. \tag{4.23}$$

In this case the parameters are the log-mean and the log-variance. The log-mean is the mean of the Gaussian distribution in log space and the log-variance is its variance. The linear statistics can be found from the log-mean and log-variance by:

$$mean = e^{x_m + 1/2\sigma_L} \tag{4.24}$$

$$median = e^{x_m} \tag{4.25}$$

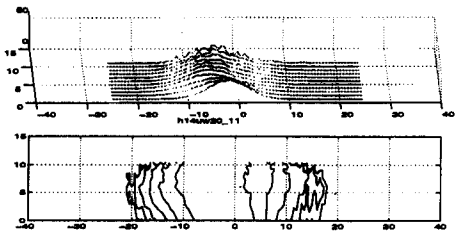

(a) 20 degrees

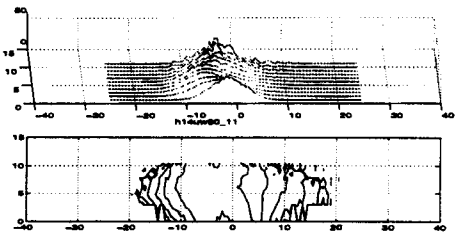

(b) 30 degrees

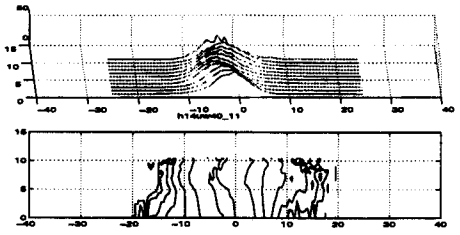

(c) 40 degrees

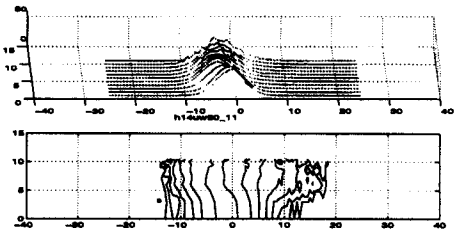

(d) 50 degrees

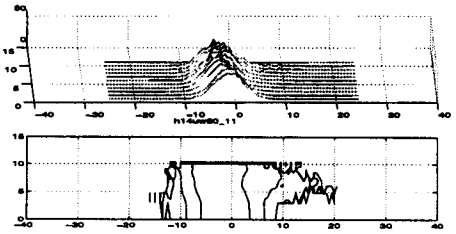

(e) 60 degrees

Figure 4.13: Wind speed evolution of power distribution. Distributions are normalized to have mean of zero dB to show the change in distribution shape with incidence angle and wind speed.

$$mode = e^{(x_m - \sigma_L^2)} \tag{4.26}$$

$$variance = w(w-1)e^{2\sigma_L} \tag{4.27}$$

where $w = e^{\sigma_L^2}$.

Figures 4.14 thru 4.17 show these parameters in graphical form. The plots are separated by polarization, frequency, and incidence angle. The log-means are plotted as a function of wind speed. The error bars correspond to the square root of the log-variance.

The most obvious trend is the increase in the mean cross section with wind speed. Although this is the characteristic of sea scattering which is the focus of most research, it will not be analyzed here in much detail. Detailed discussions of the magnitude of the radar cross section are available in many papers. The rate of the increase with wind speed has also been previously studied in depth and the reader is referred to (Collyer, 1994) for further details.

The log-variance of the data illustrates some of the problems of wind retrieval using microwave radar. Note that the width of the distributions is rather large compared to the change in the mean with wind speed. In some cases a horizontal line may be drawn which goes through the error bars for all wind speeds. These results give an indication of how much averaging must be done in order to make a good estimate of the mean radar cross section.

Several trends are also visible in the log-variance data. One is that the log-variance of the distributions decreases with increasing incidence angle. This is in agreement with the composite model which predicts smaller variance as the slope of the incidence angle dependence (m) decreases and the antenna footprint increases. Using this same argument, we should see that the V-pol log-variances are less than

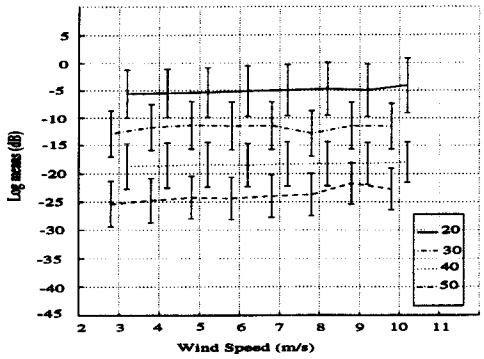

(a) 2 Ghz

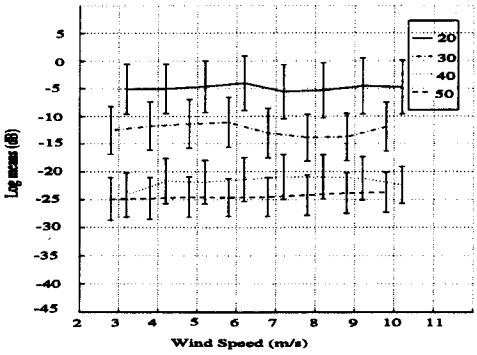

(b) 3 Ghz

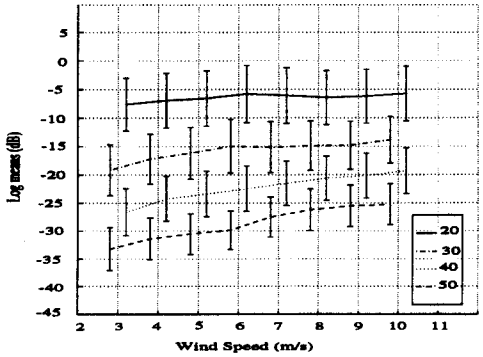

(c) 5 Ghz

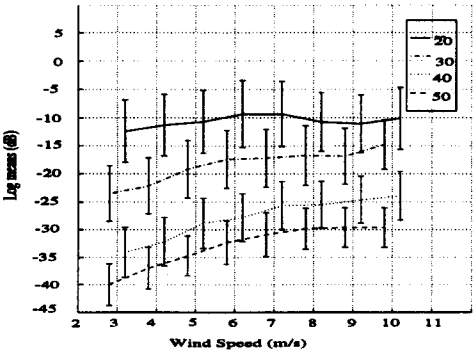

(d) 10 Ghz

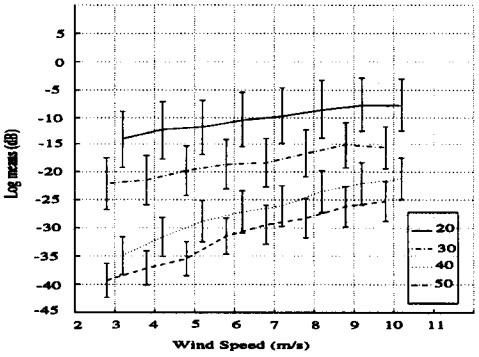

(e) 14 Ghz

Figure 4.14: Log mean plots for H-pol, upwind data verses wind speed. The error bars correspond to ± the square root of the log-variance. The legend specifies the line type of various incidence angles in degrees.

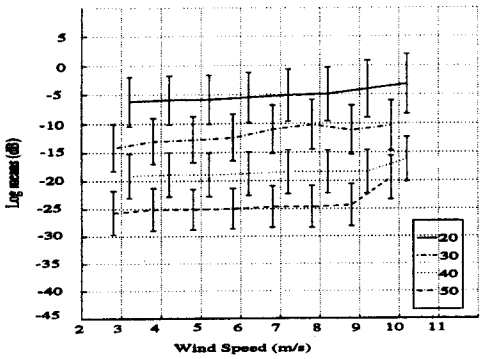

(a) 2 Ghz

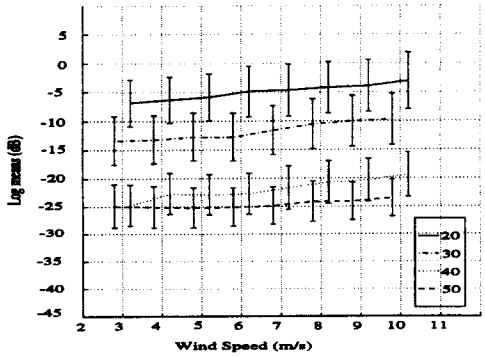

(b) 3 Ghz

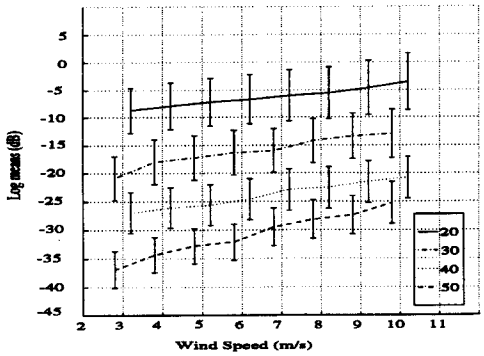

(c) 5 Ghz

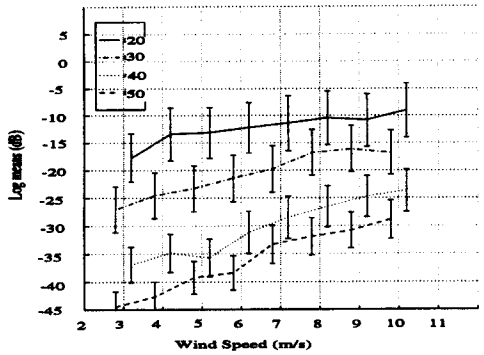

(d) 10 Ghz

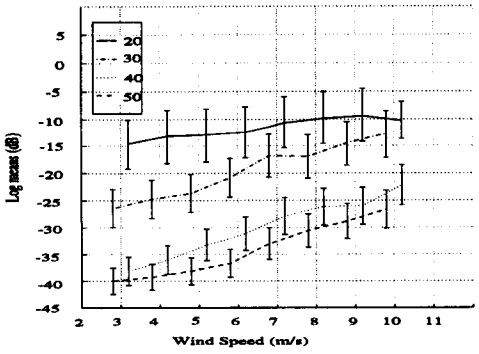

(e) 14 Ghz

Figure 4.15: Log mean plots for H-pol, downwind data verses wind speed. The error bars correspond to ± the square root of the log-variance. The legend specifies the line types corresponding to various incidence angles in degrees.

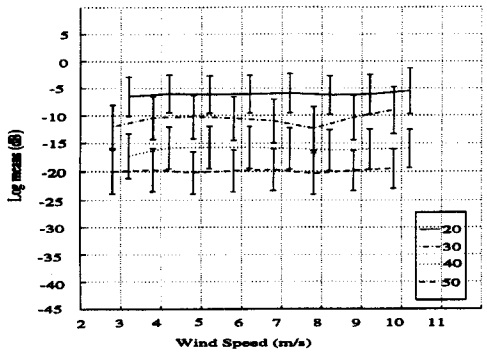

(a) 2 Ghz

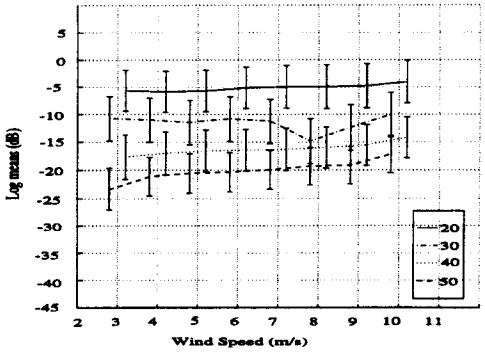

(b) 3 Ghz

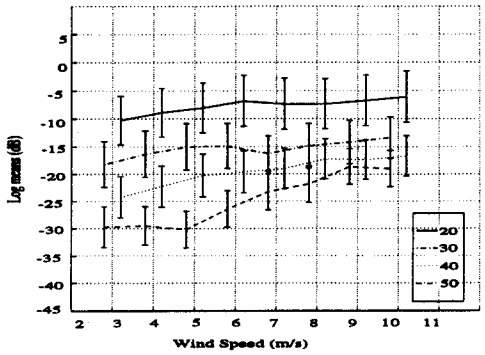

(c) 5 Ghz

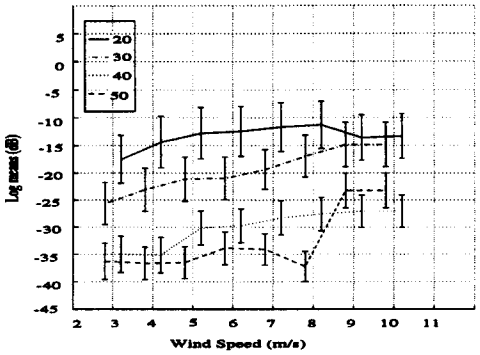

(d) 10 Ghz

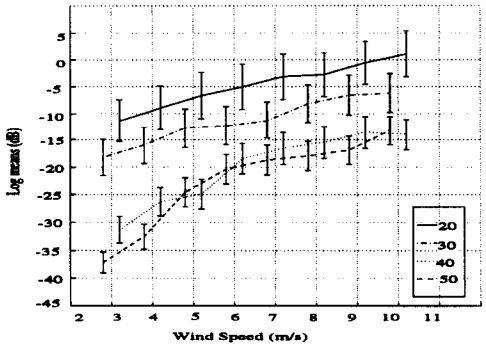

(e) 14 Ghz

Figure 4.16: Log mean plots for V-pol, upwind data verses wind speed. The error bars correspond to ± the square root of the log-variance. The legend specifies the line types corresponding to various incidence angles in degrees.

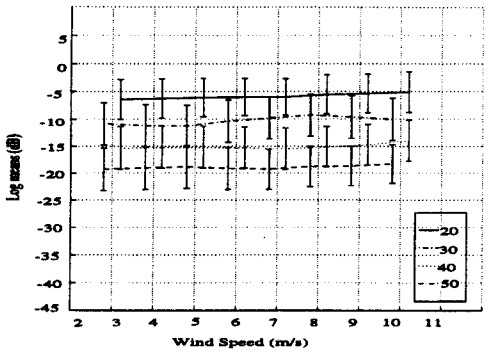

(a) 2 Ghz

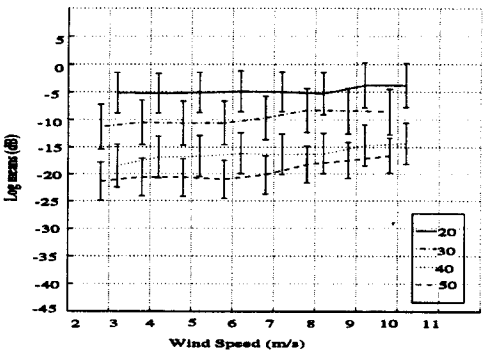

(b) 3 Ghz

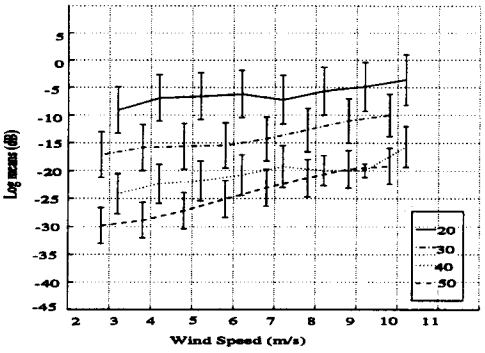

(c) 5 Ghz

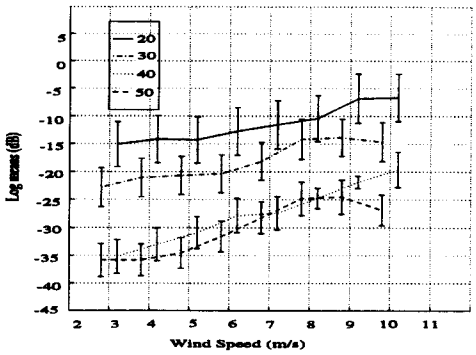

(d) 10 Ghz

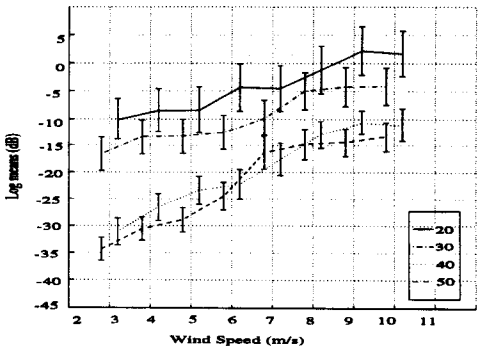

(e) 14 Ghz

Figure 4.17: Log mean plots for V-pol, downwind data verses wind speed. The error bars correspond to ± the square root of the log-variance. The legend specifies the line types corresponding to various incidence angles in degrees.

the corresponding H-pol log-variances. Figures 4.18 thru 4.21 show that the V-pol log-variances are typically 5-10 dB less than H-pol which supports this idea.

Another noticeable trend is that the log-variances does not seem to change strongly with wind speed. To see this more clearly, Figs. 4.18 thru 4.21 show the log variance verses wind speed for different incidence angles. Also note that the V-pol log variances are much less variable than the H-pol. Even for low incidence angle, low frequency data which for the H-pol increases quickly with wind speed, the V-pol log variance is remarkably flat. This agrees with the composite model since the V-pol incidence angle dependence is much less for moderate incidence angles, as seen in Fig. 4.6.

The rather small or even negative wind speed dependence of the log-variance of the measured distributions does not seem to fit with the simple model developed in the simulation; one would expect the distributions to become wider as the mean square slope increases with wind speed.

To investigate this further we can utilize the simulation described in the previous section. This data is analyzed using the same techniques as the empirical data to compute the average histogram of the cross section distribution. Then log-normal distributions are fit using the same criteria as before. Figure 4.22 shows the wind speed dependence for the simulation data for 40 and 50 degree incidence angles.

Note that the simulation log-variance is on the same order of magnitude as the empirical results. Also encouraging is the incidence angle dependence apparent in the empirical data which is also visible in the simulation. However, the wind speed dependence is distinctly different. While the simulation data increases significantly with wind speed, the empirical data shows no increase in most cases and even

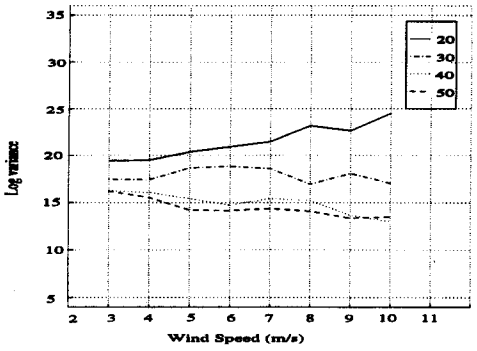

(a) 2 Ghz

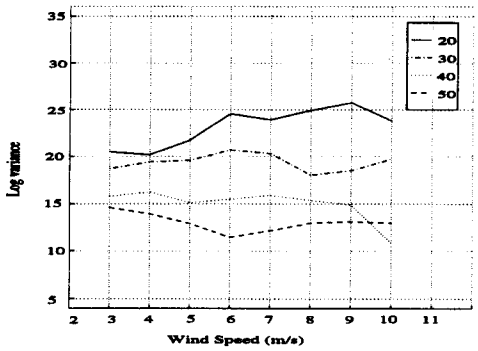

(b) 3 Ghz

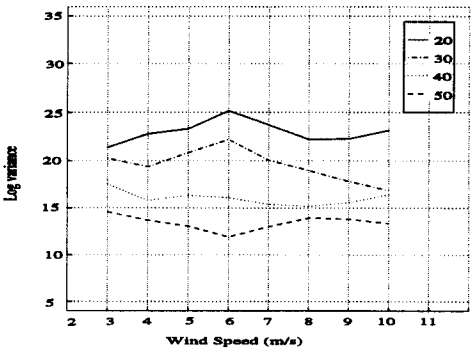

(c) 5 Ghz

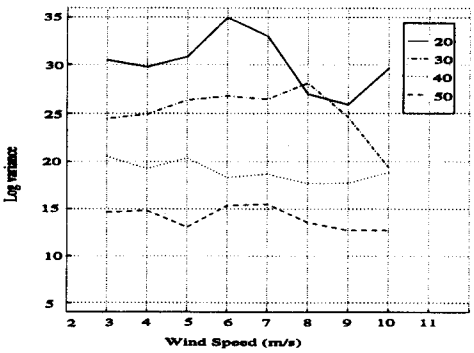

(d) 10 Ghz

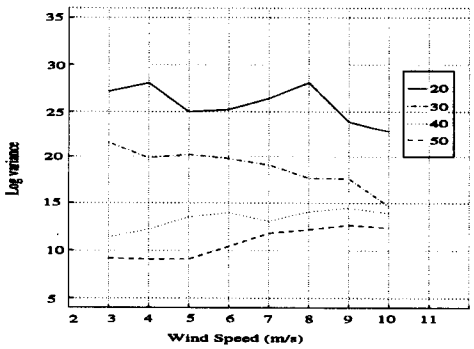

(e) 14 Ghz

Figure 4.18: Log variance plots for H-pol, upwind data verses wind speed. The legend specifies the line types corresponding to various incidence angles in degrees.

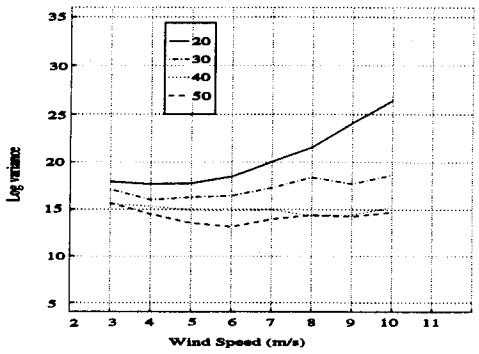

(a) 2 Ghz

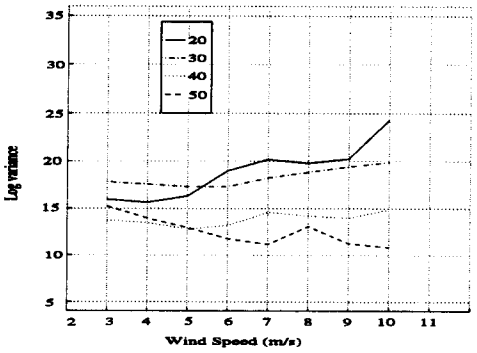

(b) 3 Ghz

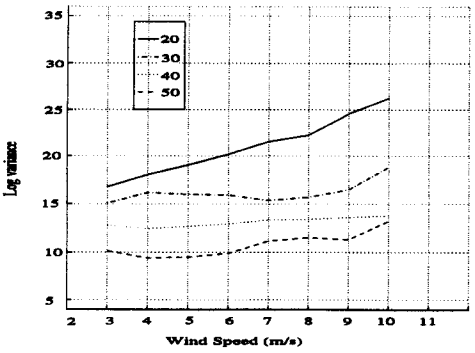

(c) 5 Ghz

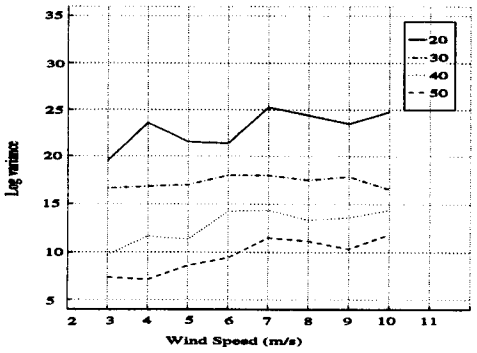

(d) 10 Ghz

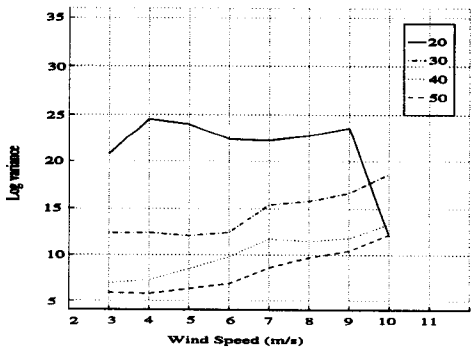

(e) 14 Ghz

Figure 4.19: Log variance plots for H-pol, downwind data verses wind speed. The legend specifies the line types corresponding to various incidence angles in degrees.

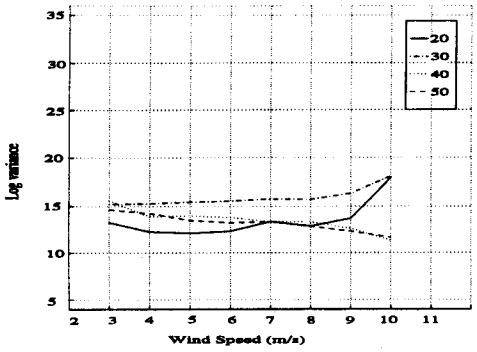

(a) 2 Ghz

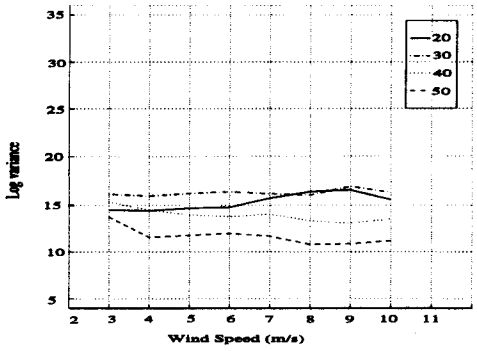

(b) 3 Ghz

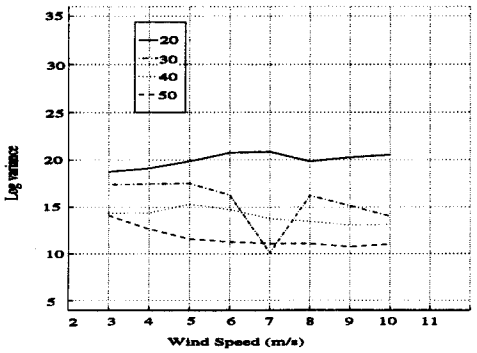

(c) 5 Ghz

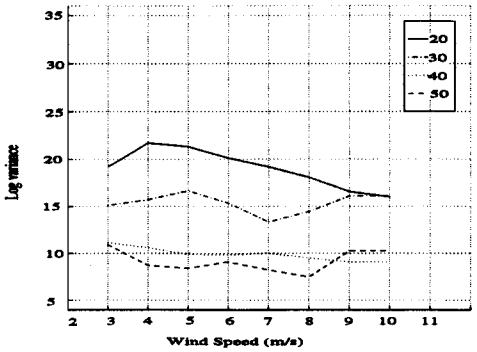

(d) 10 Ghz

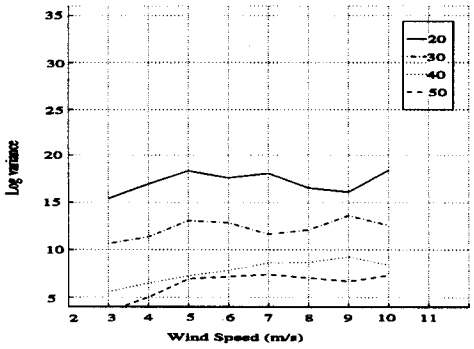

(e) 14 Ghz

Figure 4.20: Log variance plots for V-pol, upwind data verses windspeed. The legend specifies the line types corresponding to various incidence angles in degrees.

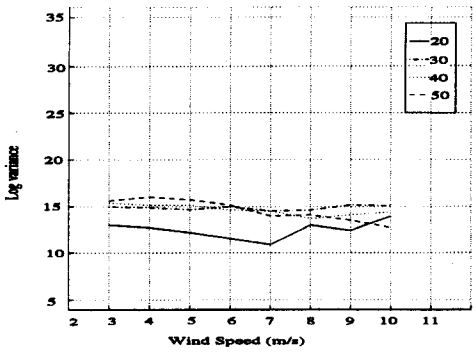

(a) 2 Ghz

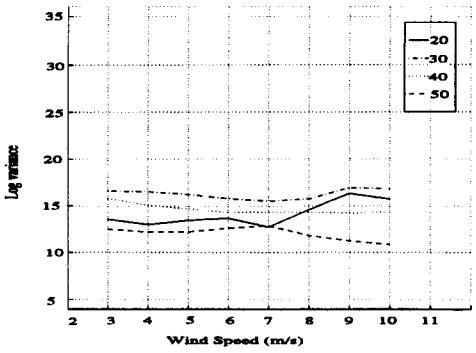

(b) 3 Ghz

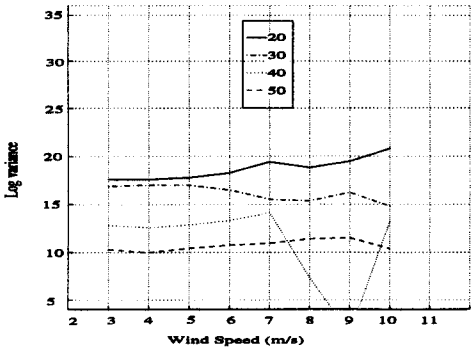

(c) 5 Ghz

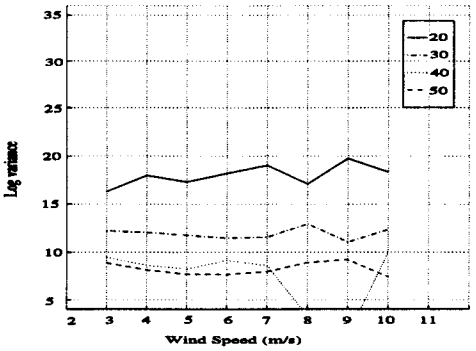

(d) 10 Ghz

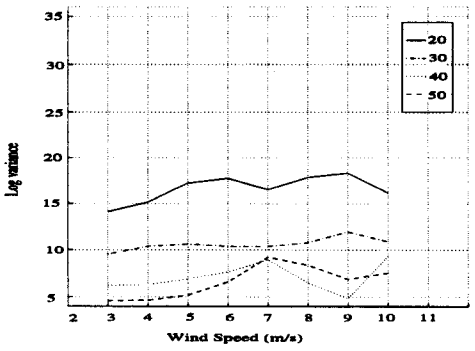

(e) 14 Ghz

Figure 4.21: Log variance plots for V-pol, downwind data verses wind speed. The legend specifies the line types corresponding to varous incidence angles in degrees.

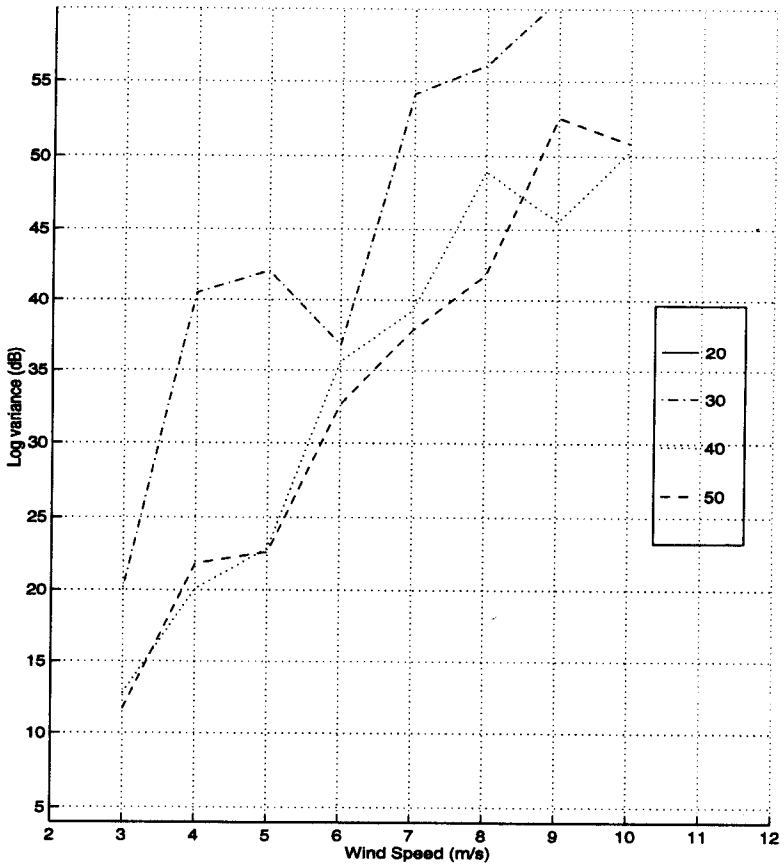

Figure 4.22: This plot shows the log-variance of the simulation data verses wind speed. The simulation increases more strongly with wind speed than does the empirical data. The legend specifies the line types corresponding to various incidence angles in degrees. This particular curve corresponds to H-pol, upwind, 10 GHz data, however all of the simulation data showed a similar trend.

slight decreases in others. The only measurements consistently increasing with wind speed are low frequency, low incidence angle measurements and high frequency, high incidence angles for H-pol.

When this is viewed in light of the composite model, it is clear that the fluctuations of the local incidence angle, which increase with wind speed, will tend

to increase the log-variance of the radar return as was illustrated in the simulation. However, if the coherence area of the surface is decreasing with wind speed, the antenna footprint is averaging over more independent areas, which tends to decrease the variance of the measurements. Figure 4.22 shows the effect of averaging independent areas in the simulation. From this figure we can see by increasing the number of independent areas from 1 to 10, the log-variance is substantially reduced.

From Fig. 4.23 we can see that if the coherence length decreases by a factor of two (corresponding to an increase by a factor of four in the number of independent areas) results in a wind speed dependence similar to that observed in the empirical data. Some empirical work has been done on the subject of coherence areas but the results insufficient to determine the wind speed dependence (Plant et al., 1994). The Yscat94 data suggests that coherence areas decrease with increasing wind speed.

4.4 Further Comparison With Simulations

Comparison of the simulations with the empirical data in the previous section illustrated some areas of disagreement between the simple model presented in the first section and the empirical results. Further analysis may help illuminate other disagreements between the theory and the empirical data.

Detailed, case by case comparison of each set of simulation-empirical pairs would be cumbersome given the huge amount of data. Dividing the data by frequency, polarization, incidence angle, wind speed, and wind direction results in 1000 separate cases. Fortunately, some generalizations may be drawn from some representative data.

Qualitatively, the simulations compare quite well with the data. For moderate incidence angles and wind speeds the distributions appear quite log-normal.

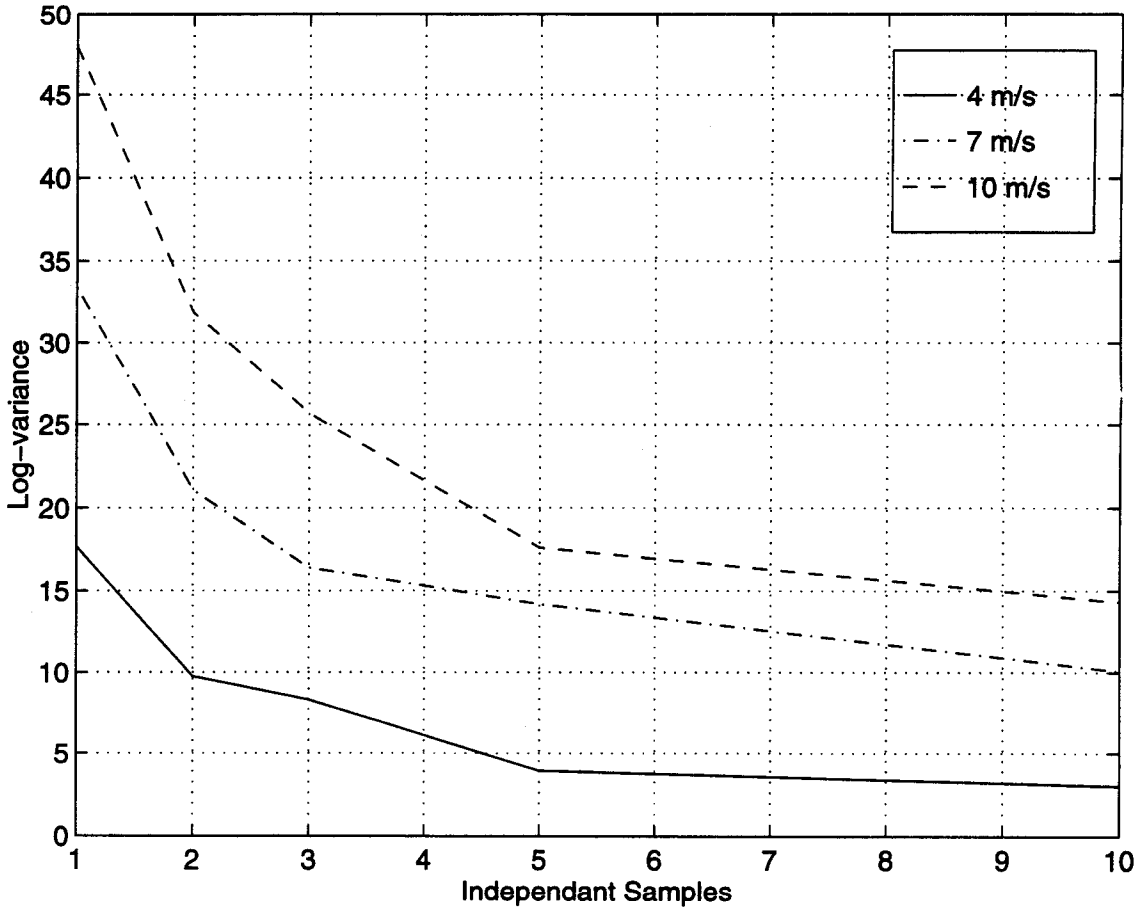

Figure 4.23: The effect of increasing the number of independent areas in the antenna pattern on the log variance. This data corresponds to the simulation data for H-pol, 10 GHz, 40 degree incidence angle data for various wind speeds.

However, there are some notable exceptions. The differences seem to be most dependence on incidence angles so the comparison presented here is stratified only by this parameter.

The data collected at 20 degrees incidence is notably different from the simulation data. Figure 4.24 compares the distributions of the empirical and simulated data side by side. The simulated data shows a distinct bi-modal distribution.

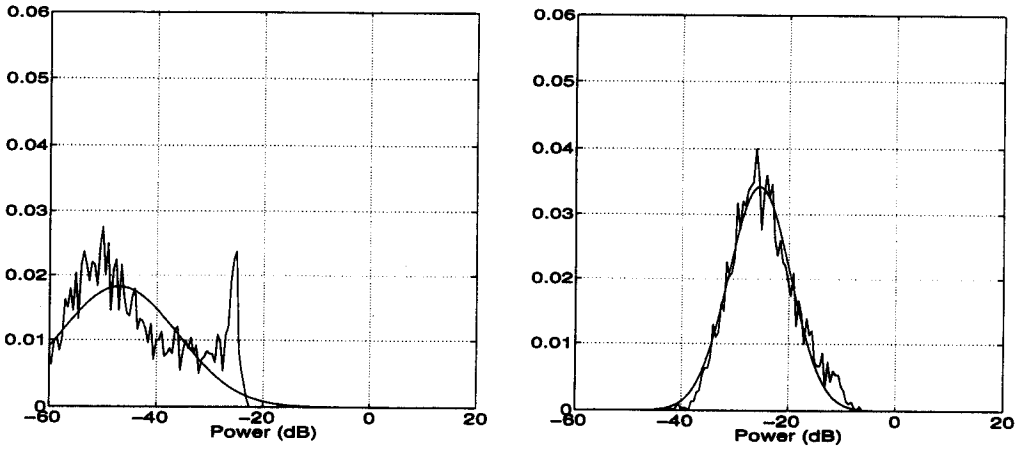

(a) H-pol, 7 m/s simulation

(b) H-pol, 7 m/s Yscat

Figure 4.24: This shows the (a) 20 degree incidence angle simulation and (b) empirical data. Note the strong specular component (the peak to the right) in the simulation data. This shows that the composite model does not apply to this range of incidence angles.

Examining Fig. 4.3 it is clear that this is caused by the superposition of the specular and Bragg scattering components of the incidence angle dependence. As the mean squared slope increases with wind speed, more and more portions of the sea surface become normal or near normal to the radar. This specular scattering tends to dominate the radar return. This is illustrated in Fig. 4.25. However, this bi-model behavior is noticeably absent in the actual radar data.

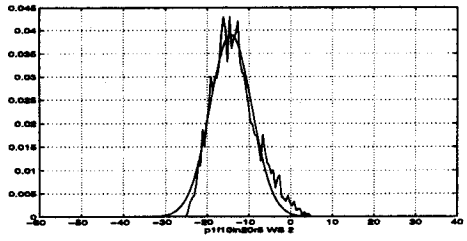

(a) 2 m/s

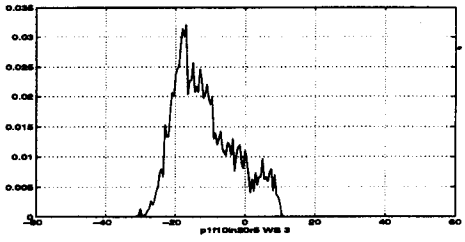

(b) 3 m/s

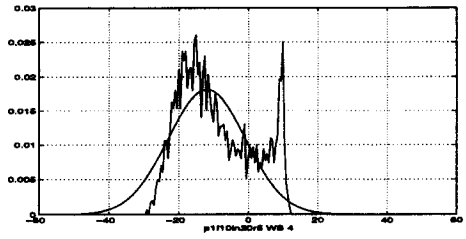

(c) 4 m/s

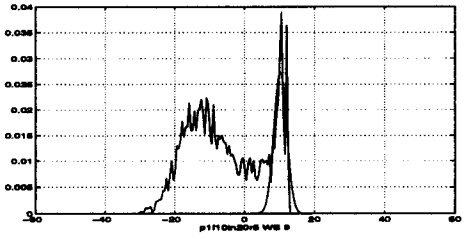

(d) 9 m/s

Figure 4.25: The evolution of simulated 20 degree incidence data with increasing wind speed. Note how the specular portion soon dominates the return as wind speed increases. The smooth line is the log-normal fit.

An explanation for the lack of a specular peak in the radar data may be that some other mechanism moderates the transition from specular to Bragg scattering which would tend to wash the peaks of the distribution out. In any case, the simulation demonstrates a fact not usually stressed in discussions of the composite model: even though the rms waveslope does not seem large enough to cause significant specular scattering, the extremely large cross section of these specular events can cause the upper tail of the wave slope distribution to dominate the cross section distribution, even though they occur relatively infrequently.

The 30 degree incidence data compares much better with the simulation. The specular portion is only visible at higher wind speeds and does not dominate the return. Figure 4.26 compares the simulation and empirical data at 7 m/s wind speed and 10 GHz. Note that although at this wind speed the specular events are not strong, there is a distinct upper tail to both the simulation and the empirical data, although the simulation does show some effects of the specular scattering.

The upper tail deviation in the empirical data from the log-normal may be caused by some of the additional scatterers which have been proposed in previous research. Wave breaking has been associated with "sea-spikes" which are short lived, large increases in the radar cross section. If this were occuring regularly, it should show up in the upper tail of the distribution. However, this cannot be the case in the simulated data since no attempt was made to include wave breaking in the model.

Note, though, that in Fig. 4.11 that the error in the empirical fits is slightly smaller at mid-incidence angles (40 and 50 degrees) than at more extreme incidence angles. This leads one to believe that the source of the error might be the

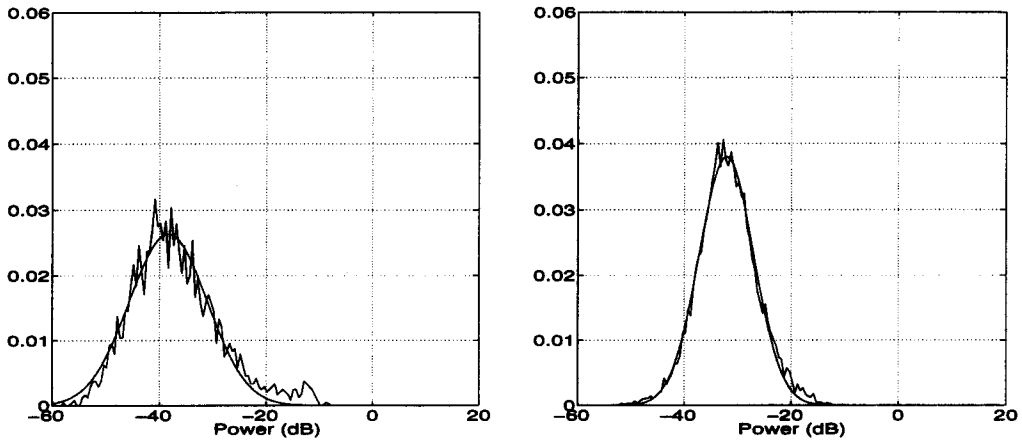

(a) H-pol, 7 m/s simulation

(b) H-pol, 7 m/s Yscat

Figure 4.26: This shows the (a) 10 Ghz, H-pol, 30 degree incidence angle simulation and (b) empirical data. The simulation data agrees with the empirical data quite well except for the extreme upper tail which shows signs of specular scattering in the simulation.

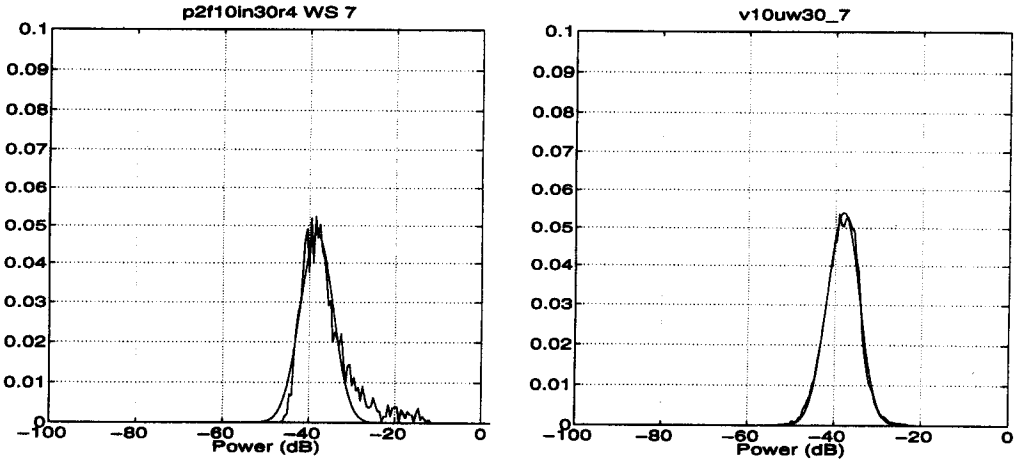

(a) V-pol, 7 m/s simulation

(b) V-pol, 7 m/s Yscat

Figure 4.27: This shows the (a) 10 Ghz, V-pol, 30 degree incidence simulation and (b) empirical data. The quality of the fit is similar to that for H-pol. Note that the difference in the variances of the empirical distributions between H and V-pol is reflected quite well in the simulation data.

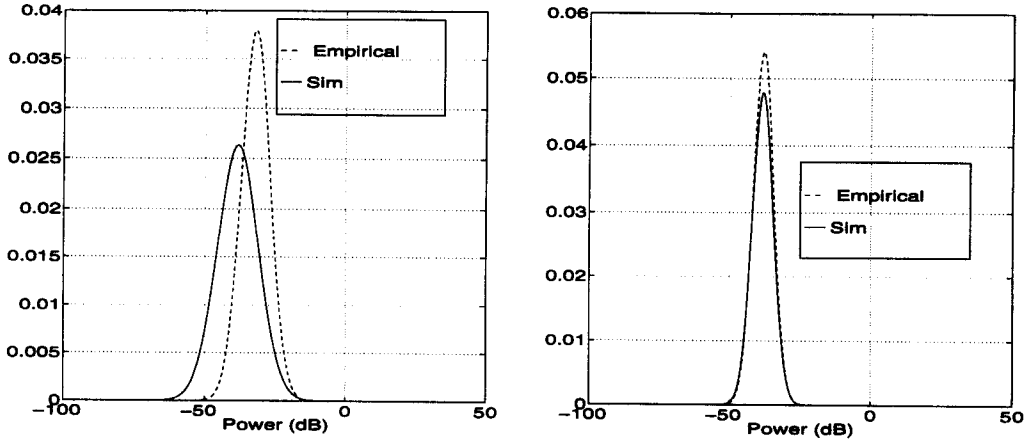

(a) H-pol

(b) V-pol

Figure 4.28: 30 degree, 10 GHz, 7 m/s simulation and empirical data overlaid for both (a) H-pol and (b) V-pol.

"nonlinearity" of the slope dependence, which is more severe at the extremes of the incidence angle range.

One of the assumptions made in arriving at the log-normal distribution from the composite model was that it was assumed that the incidence angle variation was small. Clearly, this is assumption is not as valid at high wind speeds than at low wind speeds. The simulation results agree with conventional wisdom that the mean squared wave slope increases linearly with wind speed. Figure 4.29 shows the mean squared wave slope of the simulation compared to the empirical formula given by Cox and Munk i.e.,

$$s^2 = 0.001(3 + 5.12U_w) \tag{4.28}$$

where U_w is the wind speed. The slightly lower value for the mean squared slopes arises from the fact that the fetch on Lake Ontario is generally limited, whereas the Cox and Munk result was obtained for the unlimited fetch of the ocean. Because of this increase in the variance of the wave slope, the assumption that the variance is small becomes less and less valid as wind speed increases. This suggests that the measured distributions may be less and less log-normal as wind speed increases. Figure 4.30 shows the fitting error as a function of wind speed. The fact that the fitting error increases with wind speed is consistent with the assumptions of the composite model.

The hypothesis that the deviations from the log-normal might be explained within the composite model seems to be verified in the simulation data. It seems clear from the simulation that this deviation is in fact due to the non-linearities of the $\sigma_\circ$ verses slope dependence shown in Fig. 4.3. This points out that care must be taken when interpreting the upper tail of the distribution as the result of

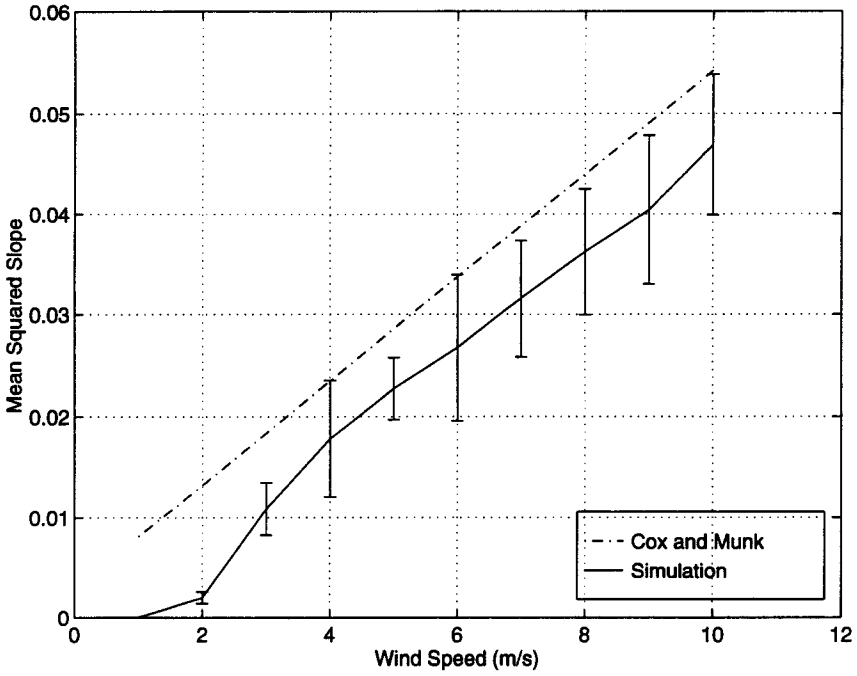

Figure 4.29: Mean squared slope of the water surface in the simulations. These values are the averages of 10 realizations of the sea surface. Note that the simulation values are slightly lower than the Cox and Munk values obtained in the ocean. This is because of the limited fetch on Lake Ontario. The simulation results agree with those of Donelan (1984).

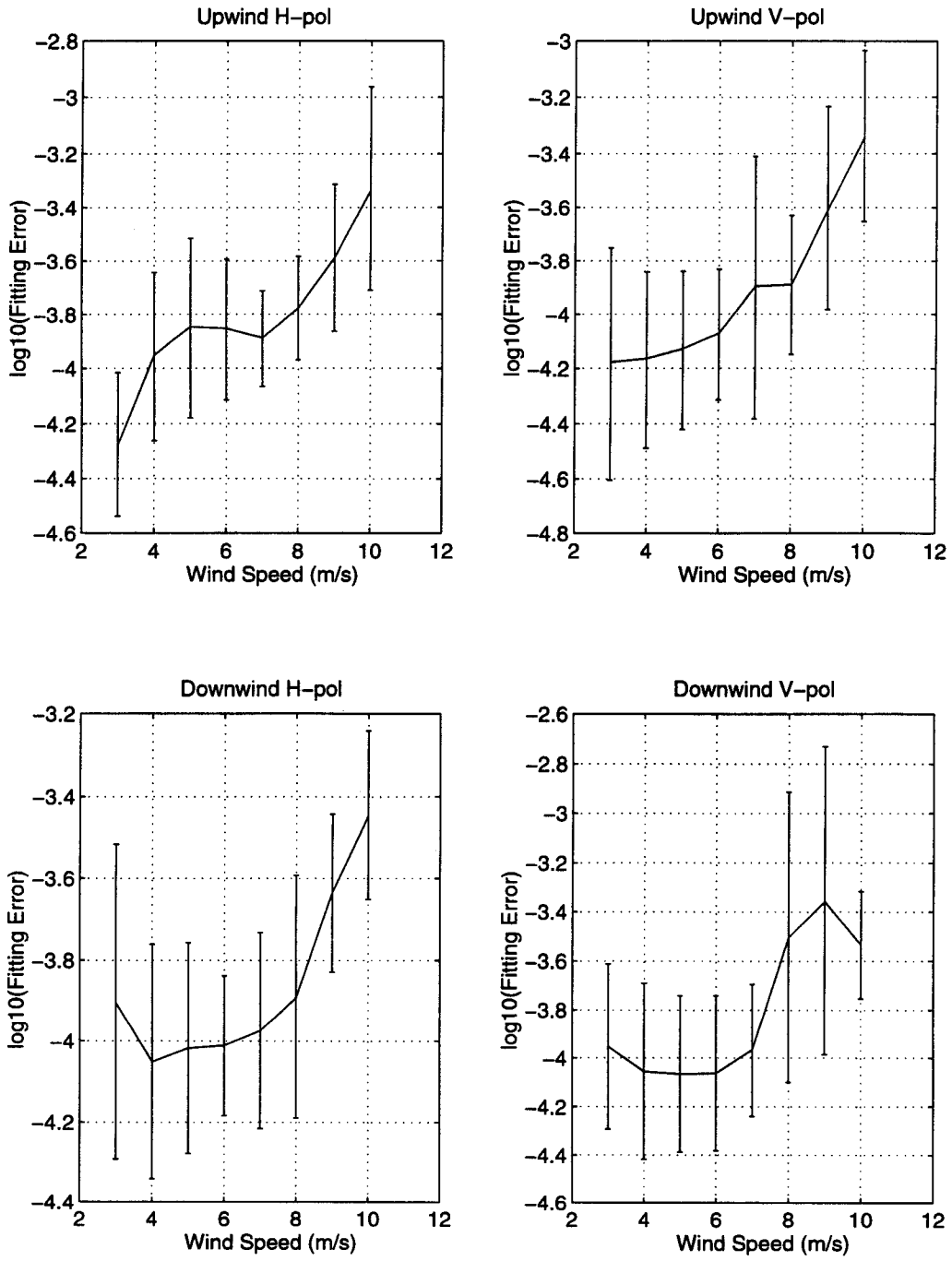

Figure 4.30: Log-normal fitting errors for the Yscat94 data plotted as a function of wind speed average over all incidence angles. The general increase with wind speed reflects the increasing variation of the observed incidence angles.

non-Bragg scattering. At least a portion of this upper tail can be explained by the composite model. This also points out an advantage of utilizing the simulation results in interpreting empirical data.

The results of the 40 and 50 degree incidence angle simulations are in good agreement with the simulation. Figure 4.31 and 4.34 show that both the variance of the distribution and the shape of the upper tail are in agreement with the simulation for both polarizations. This is the region where one expects the composite model to hold most strongly and the good agreement in the shape of the distributions seems to verify this.

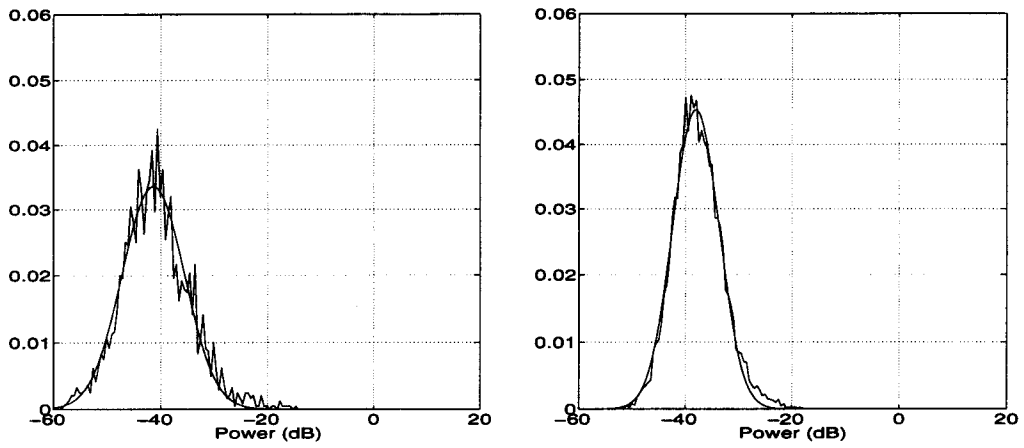

(a) H-Pol, 7 m/s simulation

(b) H-Pol, 7 m/s Yscat

Figure 4.31: 10 GHz, H-pol, 40 degree (a) simulated and (b) empirical data. Note that the general shape matches quite well; however, the simulation distribution is slightly wider than the empirical distribution.

In the 60 degree incidence angle simulations, we again see some strong departures from the simulation. Figures 4.37 and 4.38 show a strong lower tail developing in the simulation distributions. Based on the model we can deduce that this is

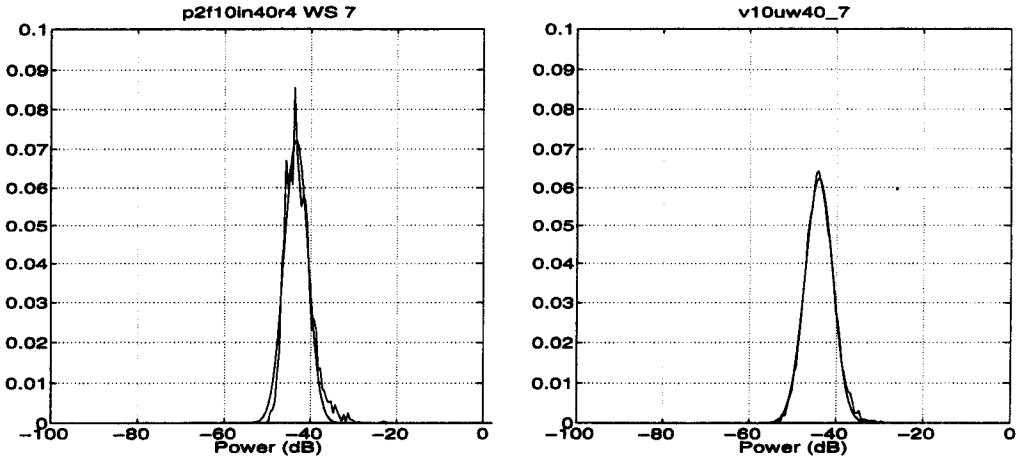

(a) V-Pol, 7 m/s simulation

(b) V-Pol, 7 m/s Yscat

Figure 4.32: 10 GHz, V-pol, 40 degree incidence angle (a) simulated data and (b) empirical data.

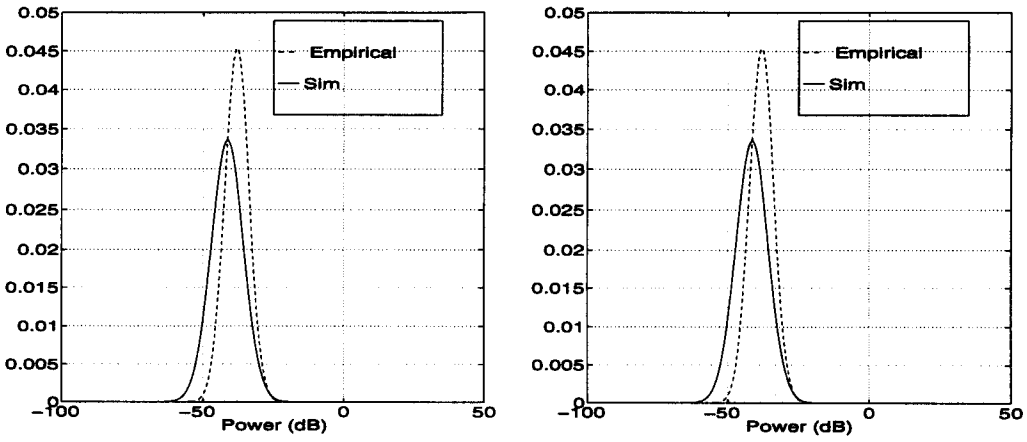

(a) H-Pol, 7 m/s

(b) V-Pol, 7 m/s

Figure 4.33: 10 GHz, 40 degree incidence angle (a) simulation and (b) empirical log-normal fits.

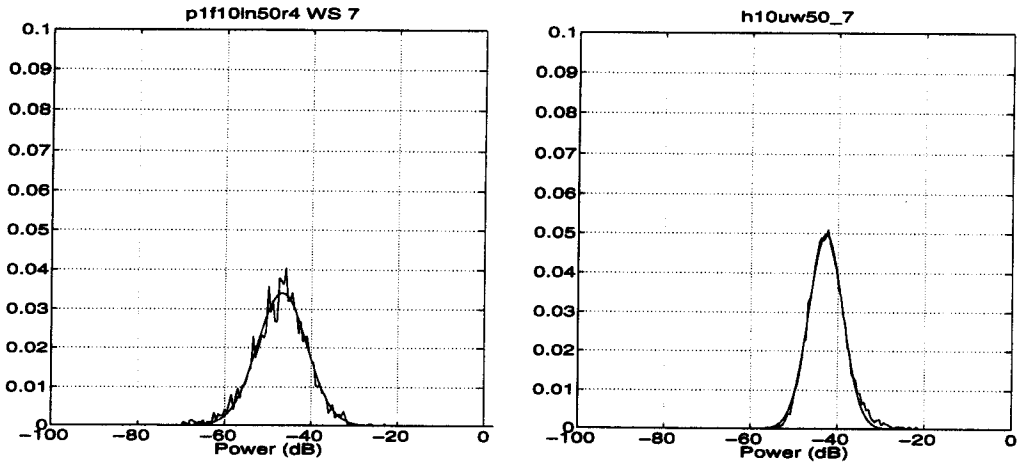

(a) H-Pol, 7 m/s simulation

(b) H-Pol, 7 m/s Yscat

Figure 4.34: 10 GHz, 50 degree incidence angle, H-pol (a) simulation and (b) empirical data.

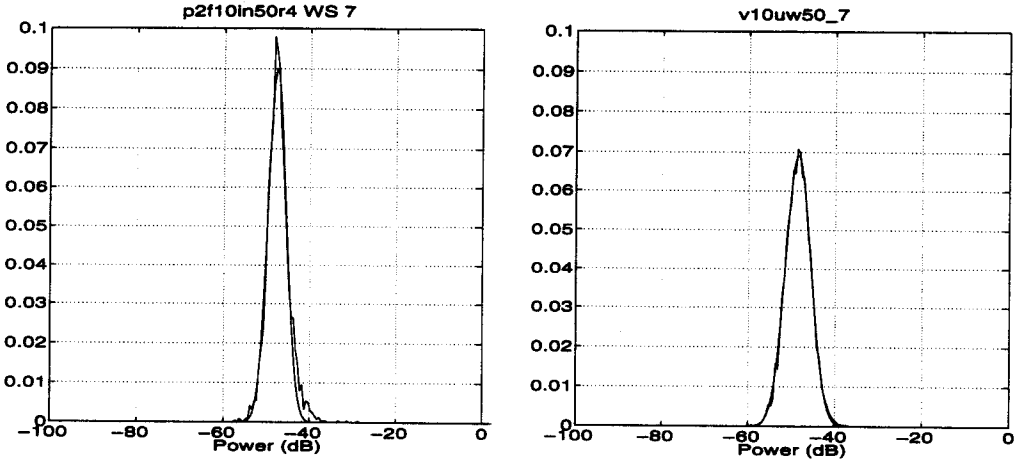

(a) V-Pol, 7 m/s simulation

(b) V-Pol, 7 m/s Yscat

Figure 4.35: 10 GHz, 50 degree incidence angle, V-pol (a) simulation and (b) empirical data.

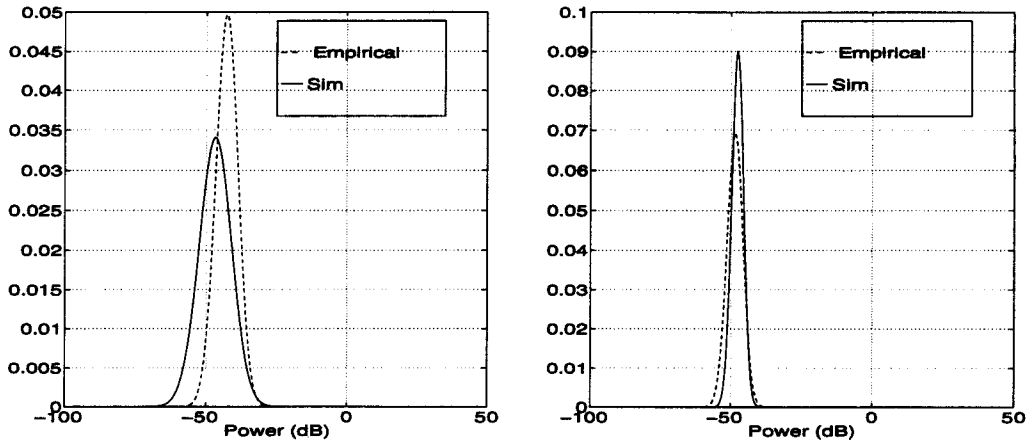

(a) H-Pol, 7 m/s

(b) V-Pol, 7 m/s

Figure 4.36: 10 GHz, 50 degree incidence angle simulation results and empirical log-normal fits.

due to the steep roll off of the Bragg contribution to the model that occurs at about 70 degrees (see Fig. 4.6).

Note however that this lower tail is conspicuously absent from the empirical data. This implies that some mechanism is adding to the incidence angle dependence when the Bragg contribution drops off. It has been noted by several researchers that the mean radar cross section does not drop off with incidence angle as predicted by Bragg scattering (Lyzenga et al., 1983).

It has been postulated that either wave breaking or wedge scattering becomes important at low incidence angles (see Fig. 2.5). Either of these mechanisms could account for the lack of a sharp drop off at high incidence angles. However, the effect on the distribution of return power would be different for each mechanism. Since breaking waves occur relatively infrequently, the distribution of a combination of wave breaking and Bragg scattering would appear very much like that of Bragg scattering alone, with a few high power events in the upper tail raising the overall mean. On the other hand, the distribution of a wedge scattering plus Bragg scattering model would be appear like the Bragg only distribution with the lower tail being truncated by the addition of the low cross section wedge scattering. The lack of a lower tail in the 60 degree incidence angle data supports this latter description of wedge plus Bragg scattering.

4.5 Summary

The simple model presented in this chapter is based on the composite model and subject to the assumptions that the incidence angle variations observed by the radar will be small and that the distributions of the wave slopes are normal. Although both of these assumptions may be criticized, the comparison of the empirical data

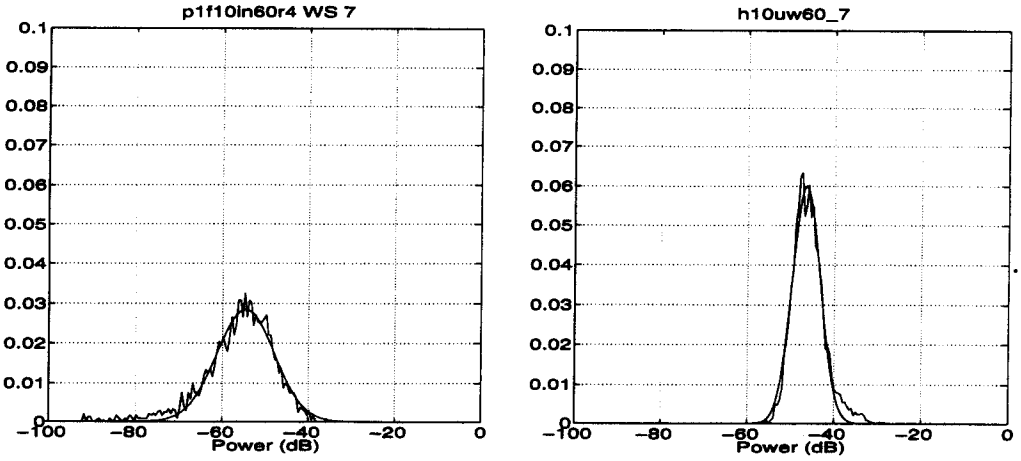

(a) H-Pol, 7 m/s simulation

(b) H-Pol, 7 m/s Yscat

Figure 4.37: 10 GHz, H-pol, 60 degree incidence angle (a) simulation and (b) empirical data. Note that the simulation data has a distinct lower tail caused by the roll off of the Bragg reflection coefficients. It's absence in the empirical data may be due to wedge scattering which is not included in the simulation.

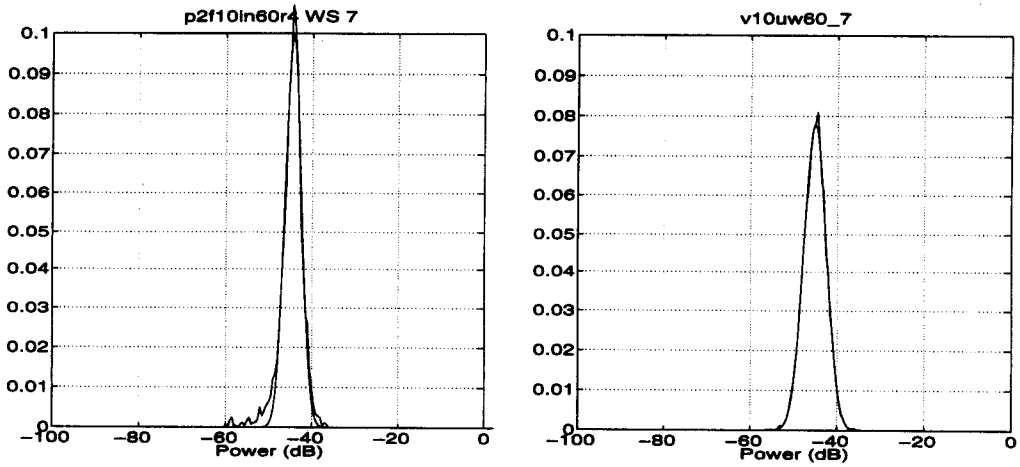

(a) V-Pol, 7 m/s simulation

(b) V-Pol, 7 m/s Yscat

Figure 4.38: 10 GHz V-pol, 60 degree incidence (a) simulation and (b) empirical data. Results are similar to H-pol.

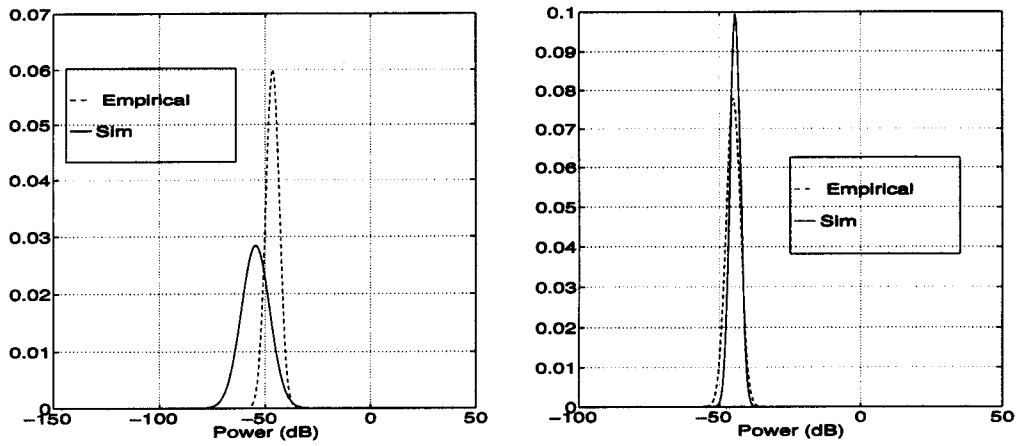

(a) V-Pol, 7 m/s H-pol

(b) V-Pol, 7 m/s V-pol

Figure 4.39: 10 GHz, H and V-pol 60 degree simulation and empirical log-normal fits.

and the simulations to log-normal distributions xseem to justify their use. Based on these assumptions, it is seen that the predicted radar cross section distribution is log-normal.

The empirical distributions are found to be very well characterized by log-normal distributions and the parameters of the log-normal fits can be used to parameterize the empirical data, accounting for an average of 98 % of the power in the empirical distributions with a standard deviation of 0.18. The simulation data appeared to agree with the empirical data qualitatively, although the simulated variance showed more wind speed dependence than is evident in the empirical data. It is shown that a decrease in the coherence area can account for this lack of wind speed dependence.

The composite model accurately predicts the incidence angle dependence of the distribution variance, as well as the differences between the H-pol and the V-pol distributions. It also showed that the model qualitatively agrees with the shape of the empirical distributions. In particular, the region from 30 to 50 degrees incidence angle seems to be in good agreement with the composite model. The simulation also revealed that the upper tail of the observed distribution is explained within the composite model. The regions up to 20 degrees incidence and from 60 degrees up are transitions regions which are not adequately explained by the composite model. Quasi-specular scattering seems to be very important at 20 degrees and wave breaking contributions are evident at 60 degrees.

Chapter 5

THE AVERAGE POWER SCATTERED BY OCEAN SCATTERERS AS A FUNCTION OF VELOCITY

5.1 Introduction

The velocity of scatterers involved in ocean scattering can be determined from the Doppler shift of the radar return. Since the different categories of scatterers (Bragg, non–Bragg) are expected to have different velocities, it is useful to look at the velocity statistics of the radar return when studying different scattering mechanisms. This chapter outlines the theory relevant to this subject and develops a simple model, based on the developments of the previous chapter, which can be used to predict the velocity statistics of the radar return based on the composite model. Then the technique used to determine the empirical velocity distributions is described and the results are compared to the model predictions. Various statistics are compared in light of the composite model and conclusions are made on its range of validity.

5.2 Scatterer Velocity Theory

Despite intense scientific interest in ocean scattering, there is still some uncertainty about what physical mechanisms are involved in ocean scattering. Mechanisms which have been proposed include Bragg scattering, wedge scattering, and wave breaking.

When categorized by velocity, these mechanisms fall into two classes: combination capillary-gravity waves and gravity waves. Bragg scatterers fall into the first

type and wedge scattering and wave breaking in the second. Figure 5.1 shows velocities of typical Bragg scatterers and typical breaking waves. From this plot it is apparent that the two categories of scatterers have distinctly different velocities when observed by the radar. Based on this distinction, we can investigate the mechanisms involved in the scattering by looking at the velocity statistics of the radar return.

5.2.1 Bragg Scatterers

Bragg waves are the small capillary-gravity waves generated by the wind on the water's surface. These are the waves involved in the Bragg resonant scattering given in Eq. (4.6). In an undisturbed medium, these waves will propagate with a phase velocity, c_p, given by:

$$c_p = \sqrt{\frac{g}{k} + Tk} \tag{5.1}$$

where g is the acceleration of gravity, T is the ratio of the surface tension to the water density, and k is the wavenumber of the water wave. This relationship is shown in Fig. 5.1. The relationship in Eq. (5.1) has been shown to hold very well in the controlled environment of a wave tank (Donelan and Pierson, 1987). In a more natural environment such as a wind driven sea, Eq. (5.1) fails to hold. There are two main causes for the break down of the dispersion relation in Eq. (5.1). First, the water's surface tends to be dragged along with the wind causing an effect called "wind drift." Second, the orbital velocity of longer waves present on the surface affects the phase velocity of the small waves.

When the wind blows over the sea surface, the upper surface of the water is dragged along with the wind because of the friction between the two fluids at the air-water boundary. Because this drift layer tends to be very thin (1-2 cm) and rather

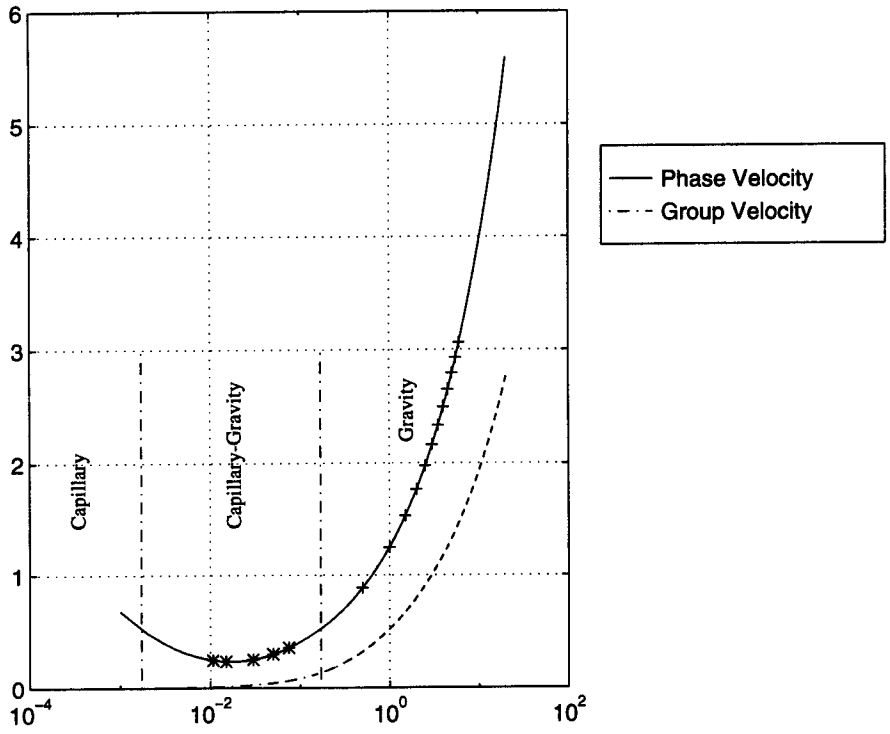

Figure 5.1: Phase velocity versus wavelength. Asterisks mark the wavelengths associated with 2, 3, 5, 10, and 14 Ghz microwave radiation. The upper line corresponds to phase velocity. The vertical lines demark the regions where the gravity term is 100 times the tension term and vice versa. This is used to define the regions into capillary, capillary-gravity, and gravity waves. Plus marks indicate typical breaking wave velocity for 1-10 m/s winds.

turbulent, the effect of this moving layer of water on the phase velocity of the small waves is not a simple addition of velocities. Theoretical models for the effect of this shear flow on the phase velocities of capillary waves can be derived from the equations of hydro-dynamics but are extremely complicated and difficult to apply in practical situations (Plant and Keller, 1980). By fitting wave tank data (Plant and Keller, 1980) with theoretical models, a rather simplified dispersion relation which accounts for wind drift is given by:

$$C_p = C_i + 0.6u_* - 0.084u_* \log(1 + \frac{z}{0.003}) \tag{5.2}$$

where C_i is the intrinsic phase velocity, u_* is the friction velocity, and z is 0.044 times the water wavelength (Plant, 1986). Equation (5.2) clearly indicates that the phase velocity increases linearly with friction velocity.

The friction velocity is a measure of how hard the wind is pulling on the water, which may change with environmental conditions even at constant wind speed. Actually measuring the friction velocity is a difficult endeavor, requiring both vertical and horizontal wind speed measurements. In general, one may use a bulk formula based on previous friction velocity measurements. For Lake Ontario, the wind speed is related to the friction velocity by (Colton, 1989):

$$u_*^2 = C_d U_W^2 \tag{5.3}$$

where C_d is a drag coefficient given by

$$C_d = 0.001(0.37 + 0.137U_W), \tag{5.4}$$

and U_W is the wind speed measured at 10 meters above the surface. This is depicted graphically in Fig. 5.2. This additional velocity is constant for constant environmen-

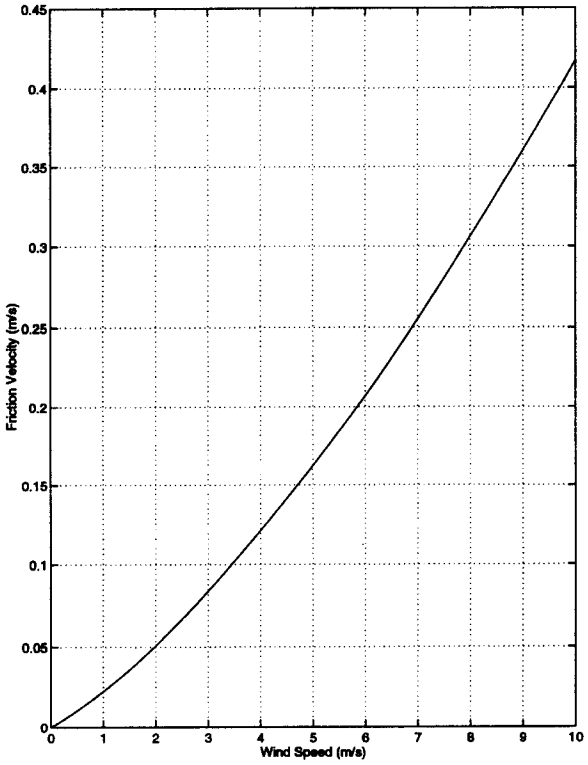

Figure 5.2: Plot of friction velocity verses wind speed. This plot was generated using the bulk formula derived in Colton (1984) for Lake Ontario

.

tal conditions and results in a net shift in the average phase velocity of the small capillary waves of about 1-4 percent of the local wind speed.

When a long wave propagates through a field of much smaller capillary waves, the water particles are accelerated both vertically and horizontally. Since the scale of the long wave is much larger than that of the capillary waves, the capillary wave propagates at its intrinsic velocity given by Eq. (5.1) where c_p is measured in the rest frame of the water particles. Since this is an oscillatory motion, the net effect on the phase velocity of the capillary waves has an average value of zero.

The line of sight (LOS) velocity of the water surface as a long wave propagates by is given by deep water wave theory (Plant and Keller, 1983) as

$$V(t) = \omega A(\omega)(\sin\theta \sin(\omega t) + \cos\theta \cos(\omega t)) \tag{5.5}$$

where θ is the incidence angle, $A(\omega)$ is the amplitude of the long wave, and ω is the intrinsic long wave frequency. From Eq. (5.5) it is clear that the time average contribution to the small wave velocity is zero; however, the instantaneous contribution to the small wave velocity can be significant, depending on ω and $A(\omega)$.

The magnitude of the instantaneous velocity shift and its phase relative to the underlying long wave depends on the incidence angle. Figure 5.3 shows how the LOS velocity changes with incidence angle and local phase of the long wave. The net result of the superposition of the long waves on the small wave field is that a Bragg wave of a particular wavelength no longer has a single phase velocity but now is associated with range of velocities. This range depends on the amplitude and local phase of the underlying long wave. The current model used to include these effects on the small waves is the composite model.

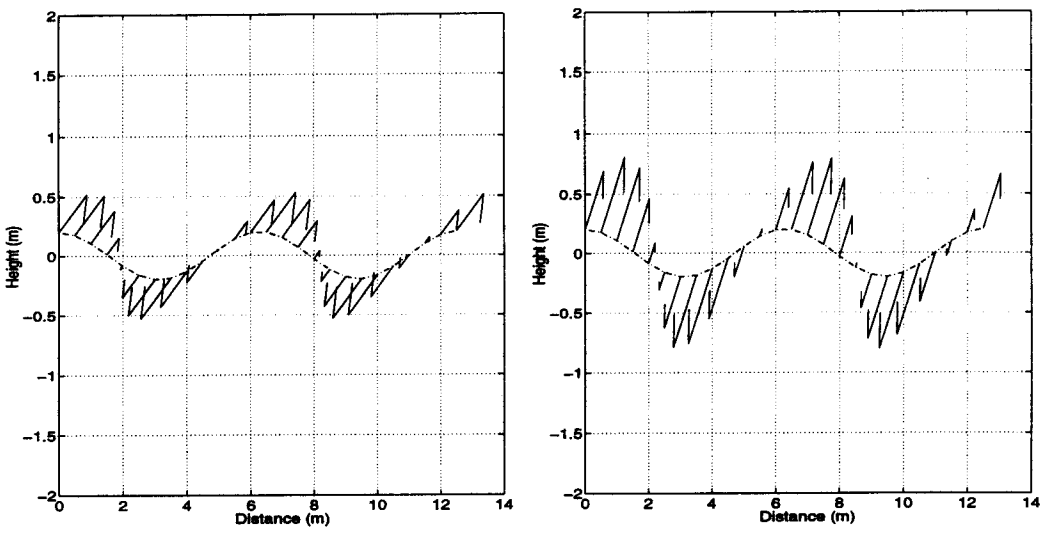

(a) 20 degrees

(b) 40 degrees

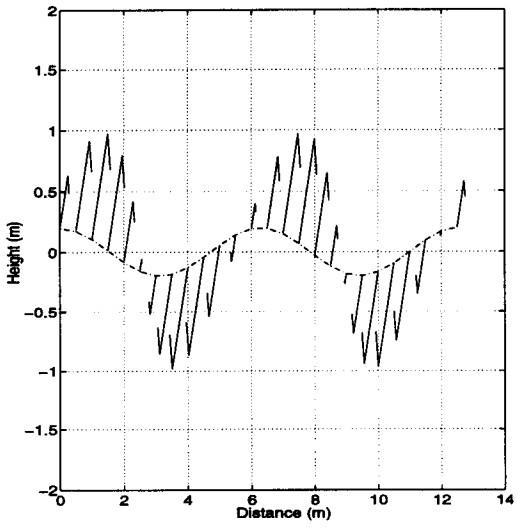

(c) 60 degrees

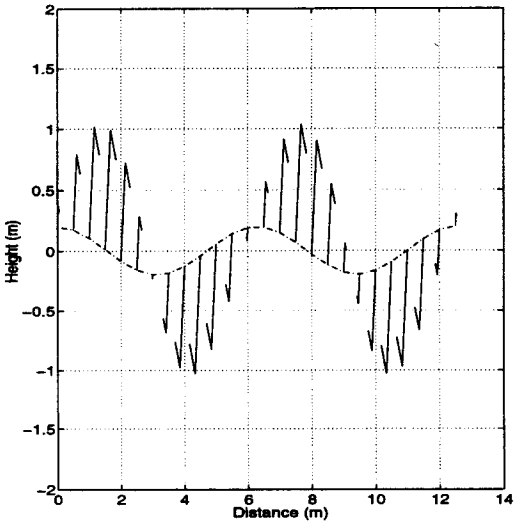

(d) 80 degrees

Figure 5.3: Line of sight velocity plot of the wave surface for various incidence angles. The arrows show magnitude of LOS velocity in the direction of observation. This plot assumes the surface is illuminated from infinitely far away. The arrows point to the direction of illumination.

5.2.2 Composite Model

The composite model separates the effect of these two processes (Bragg waves, long gravity waves) on the scattering cross section. This was developed in the previous chapter in relation to determining how the radar cross section was modulated in amplitude by the passing of the long waves.

Figure 5.3 in conjunction with Eq. (4.6) implies that there will also be a relationship between the phase of the underlying wave (and therefore the cross section) and the LOS velocity. This can be illustrated by assuming a idealized wave with a sinusoidally varying slope of rms value 10° propagating through an otherwise undisturbed medium. Using Eqs. (4.6) and (5.5) we can plot the observed cross section as a function of velocity.

Figure 5.4 shows the cross section as a function of velocity as the wave propagates past the radar. The change in cross section corresponds to the change in local incidence angle and Bragg wavelength as long wave passes by.

The principles presented above can be incorporated into a simulation fairly easily. In a natural wind driven sea, the surface contains many different wavelengths superposed on on another to form a continuous spectrum. In this case there is no longer a deterministic relationship between slope and velocity like that in Fig. 5.4, but rather a stochastic one.

This relationship can be determine using the model presented in the previous chapter by applying Eq. (5.5) to the wave height spectrum. The LOS velocity of a point can be determined by integrating Eq. (5.5) over the range of frequencies that are thought to contribute to the velocity of the patch. In this case we will use the same region as used to determine the slope, i.e. wave lengths 1 meter and longer.

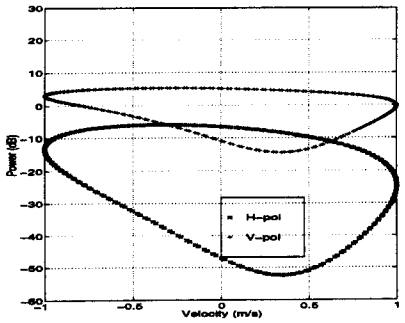

(a) 20 degrees

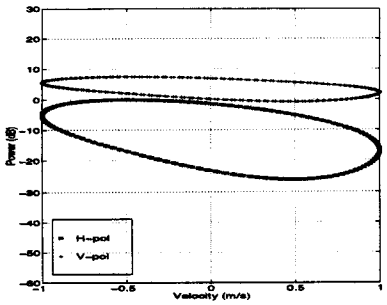

(b) 30 degrees

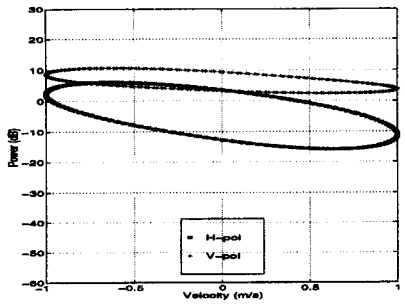

(c) 40 degrees

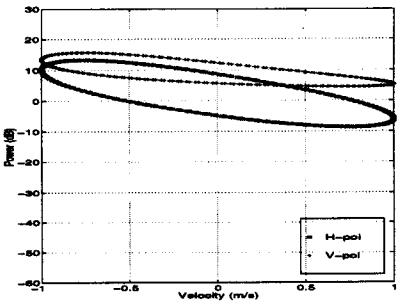

(d) 50 degrees

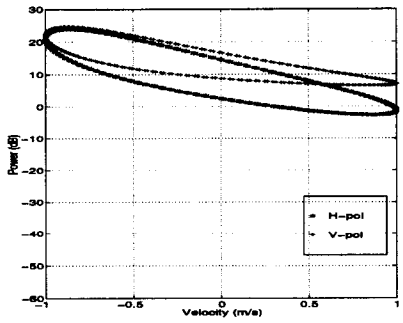

(e) 60 degrees

Figure 5.4: This plot shows the relationship between velocity and cross section for various average incidence angles. The plot assumes a single sinusoidally varying slope with 15 degree maximum slope. The solid line is V-pol and the dotted line is H-pol. The horizontal axis is velocity in m/s and the vertical axis is cross section in dB. One loop corresponds to a single wavelength passing through the observation region. The anomalies at 10 and 80 degrees incidence are caused by singularities in the reflection coefficients.

The velocity of the patch can be found by integrating the point velocities over the entire patch. This assumes that the entire patch is at the same apparent incidence angle. The results of the previous chapter support making this assumption.

Once the LOS velocity of the patch is determined, the intrinsic velocity of the Bragg scatterers must be added to the LOS velocity of the patch. At this point it is important to note that for small waves, the upwind component of the wave-height spectrum, which is negligible for gravity waves, can be significant. Although detailed measurements have not been done, an empirical result found using L-band data revealed that the amplitude of the upwind component can be as much as 1/2 the amplitude of the downwind component (Plant and Keller, 1990). Since the radar senses both upwind and downwind traveling waves equally, the net centroid measured by a scatterometer will be 1/2 the magnitude of the intrinsic phase velocity of the small waves.

The cross section associated with the velocity calculation can be determined by finding the local incidence angle and applying Eq. (4.6). This technique is performed as described in the power distribution simulations section to generate data files similar to those collected by Yscat during the Yscat94 experiment. The resulting simulated data may be processed in the same way as the real data to compare with empirical statistics.

5.2.3 Breaking Waves and Wedges

Breaking waves are one of the most visible features on the water's surface. Despite this, very little theoretical work has been done on wave breaking. The conditions that result in wave breaking are very difficult to apply a random, wind–driven sea. The velocity of a breaking wave is fairly easy to predict as the dispersion relation

in Eq. (5.1) holds very well for the longer waves which tend to be associated with wave breaking. The problem is to determine which wavelengths are the most likely to break and what the distribution of the breaking is.

Comprehensive simulations show that the vertical acceleration of the water surface is a reasonable criteria to determine whether or not a particular wave is "about to break" (Snyder and Kennedy, 1983). The average surface velocity of a breaking wave was found to be approximately one half the phase velocity of the peak wavelength. This corresponds to the group velocity of the peak wave, however, this relationship is thought to be coincidental (Snyder and Kennedy, 1983).

This result is supported with empirical evidence collected using Doppler hydrophones (Ding and Farmer, 1994). Using acoustic methods, breaking wave velocities were measured to have means that are near the value of 1/2 the phase speed of the dominant wave. Figure (5.5) shows the velocity distributions observed. The wind speed values of 6.1, 10.0, and 12.4 m/s correspond to peak phase velocities of 8.3, 10.9, and 12.3 m/s, respectively. These values were calculated using the Donelan spectrum with a fetch of 640 km.

Using the JONSWAP spectrum with parameters fit for the Lake Ontario experiment site, the theoretical peak phase velocity is given by

$$c_p = \frac{U_W}{11.6}\left(\frac{xg}{U_W^2}\right)^{0.23} \tag{5.6}$$

where x is the local fetch (Donelan et al., 1985). One half this value ($C_p/2$) corresponds to the predicted average white cap velocity. This clearly shows that the velocity of the breaking waves should increase with wind speed.

Previous researchers (Lyzenga et al., 1983) have shown that although the velocity of wedge scatterers may be higher than Bragg waves, the contribution to

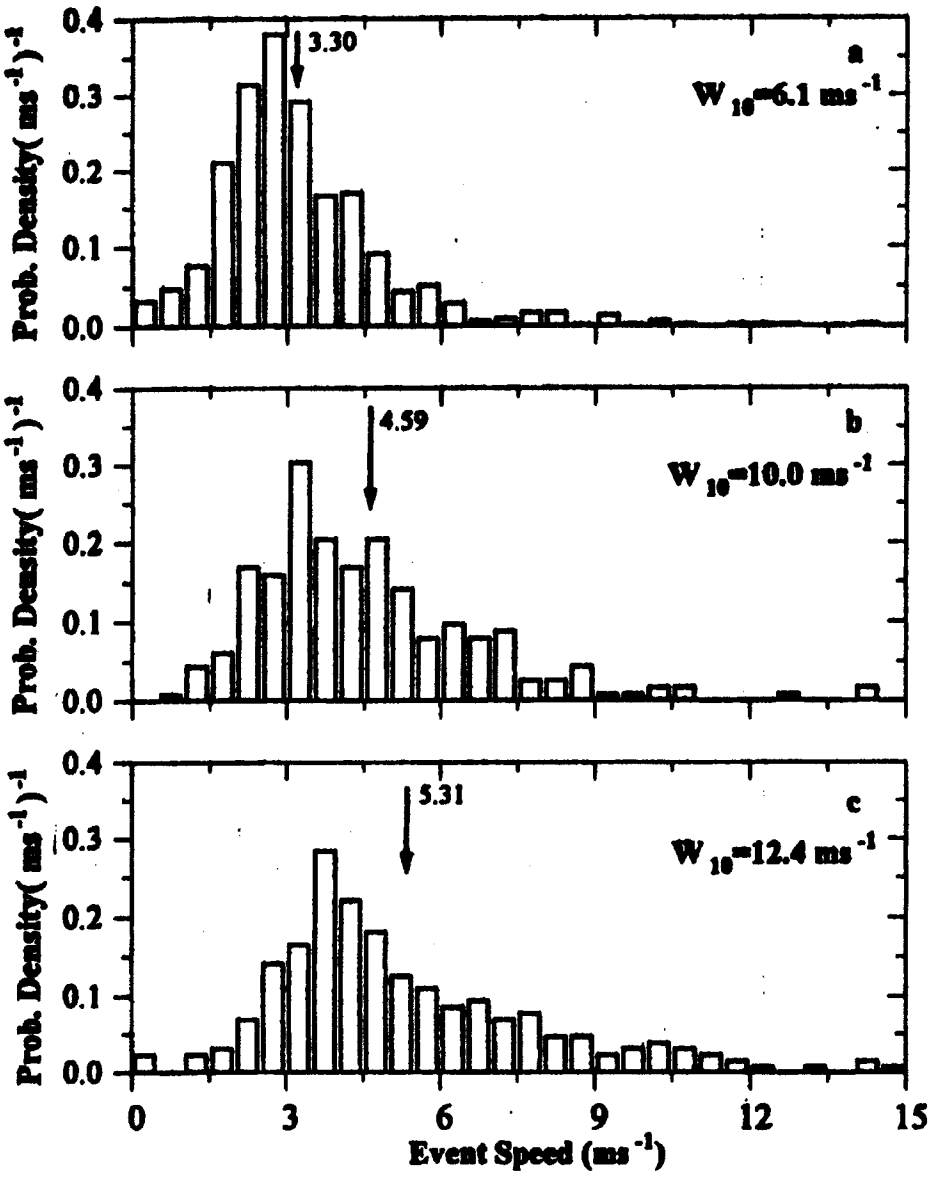

Figure 5.5: Breaking wave velocity profiles taken from Ding (1994). Predicted breaker velocities using 1/2 C_p gives 4.15, 5.45, and 6.14 m/s, respectively.

the total radar cross section probably does not become significant until the incidence angle exceeds 70 degrees. However, any contribution will be similar in velocity to that of breaking waves.

For simplicity, we can assume that wedge scatterers are closely related to breaking waves and follow the similar statistics. This assumption will hold if wedges are just breaking waves that do not quite break, or just have not broken yet. Figure 5.6 shows the relationship between the predicted mean breaker velocity and the Bragg velocity for a typical 14 Ghz measurement. Note that the breaker velocity increases very rapidly with wind speed compared to the mean Bragg velocity. This is because breaking waves tend to be associated with much longer waves than Bragg waves. It is this marked difference in velocity which makes the velocity statistics of the radar return a good place to look to determine the contribution of breaking waves to the total radar cross section.

5.3 Empirical Results

This section presents the velocity statistics as estimated from the Yscat94 data. First, the techniques used to estimate and quantify the velocity distributions are outlined. Typical results are presented and compared to results obtained using the simulation techniques described in the previous section. Finally, several specific statistics are examined to determine the degree of agreement with the composite model.

The distribution of the radar return as a function of frequency gives a measure of the range of velocities under illumination by the radar. As discussed in the previous section, the shape and properties can be examined to determine the validity of the composite model in regards to the velocity profile of the scatterers.

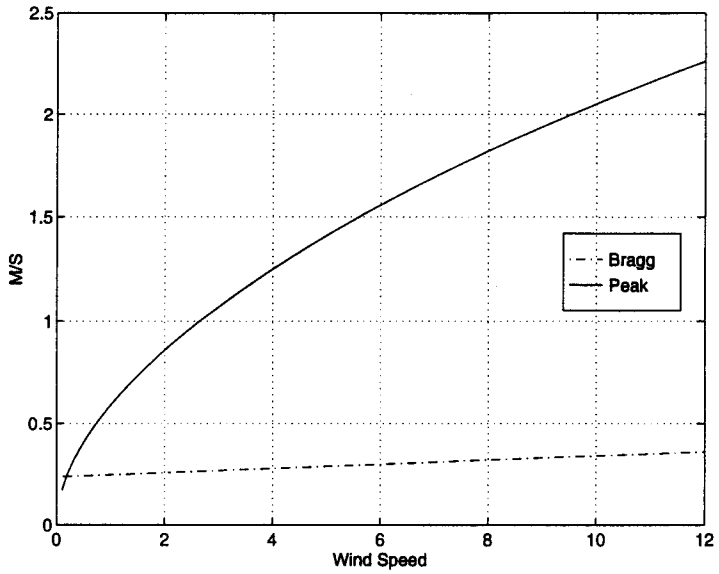

Figure 5.6: This plot shows the velocity of the Bragg waves for k = 400 rad/m (which corresponds to the Bragg wavenumber of 14 GHz at 45 degrees incidence angle) and the predicted wave breaking velocity as given by the group velocity of the peak wavelength.

The Doppler distributions are analogous to the Doppler spectrum of the radar return. In essence, they give a summary of how much power is scattered at what velocities. To compute the Doppler distributions the discrete power measurements are binned according to the velocity estimated for that measurement. A complete measurement set consists of 600 measurements corresponding to 1/10 second averages of power and velocity. Figure 5.7 shows a typical histogram calculated from a single measurement.

All of the histograms calculated for the same measurement type are averaged together to give an average histogram. The average histogram for the measurement above is shown in Fig 5.8. The evolution of the histograms with wind speed can be seen by plotting the histograms for the same radar parameters verses wind speed in a waterfall plot, as shown in Fig. 5.9. However, it is difficult to extract data from this type of plot.

As was the case in the previous chapter, it is desirable to develop a meaningful way to parameterize the empirical histograms. Figure 5.10 shows a representative group of Doppler distributions taken from the data set. Although the distribution is slightly skewed at high wind speeds, it appears that a normal distribution may be a good characterization of the shape of the distribution. To test this hypothesis, we can calculate the normal distribution that minimizes the L2 error (as defined in the previous chapter) and compare the total power accounted for by the normal compared to the power in the real signal. The results of this are summarized in Fig. 5.11. The outliers in the upper tail of this histogram correspond to cases where relatively few measurements were made. We can also check the mean of the true distribution to the mean of the fitted normal.

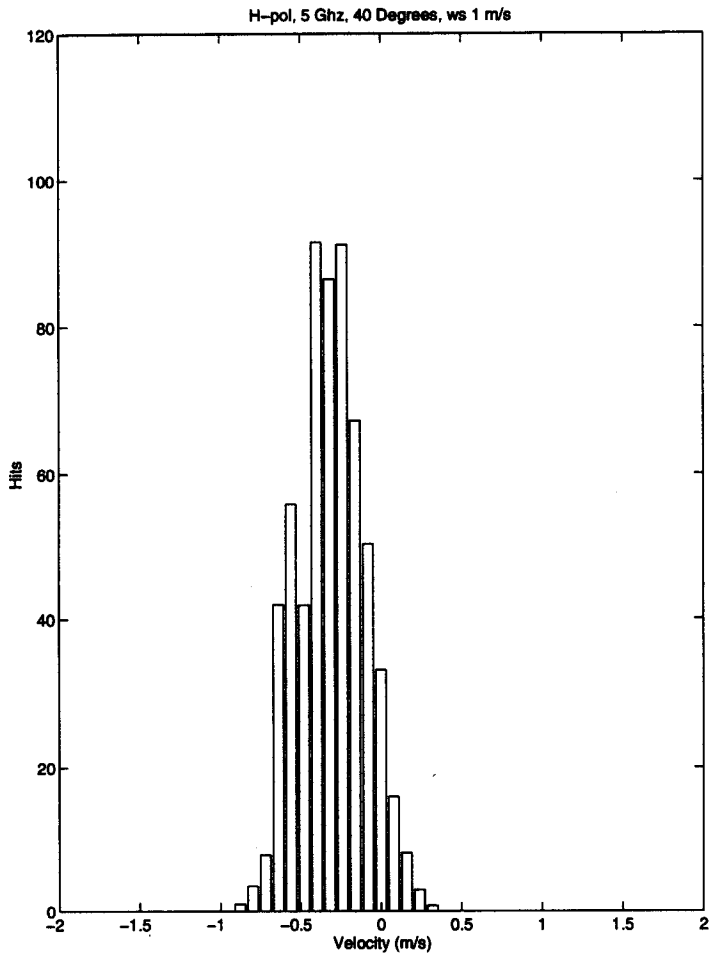

Figure 5.7: Single histogram calculated for H-pol, 5 Ghz, 40 degrees, low wind speeds.

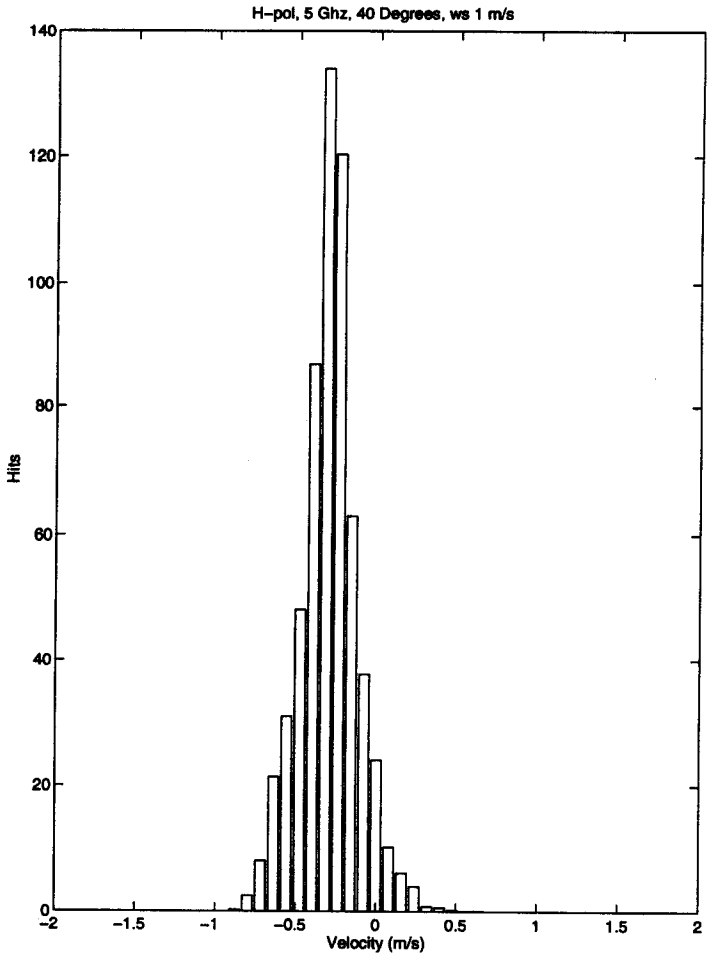

Figure 5.8: Sample average histogram calculated by averaging the bins in all the histograms with the same parameters.

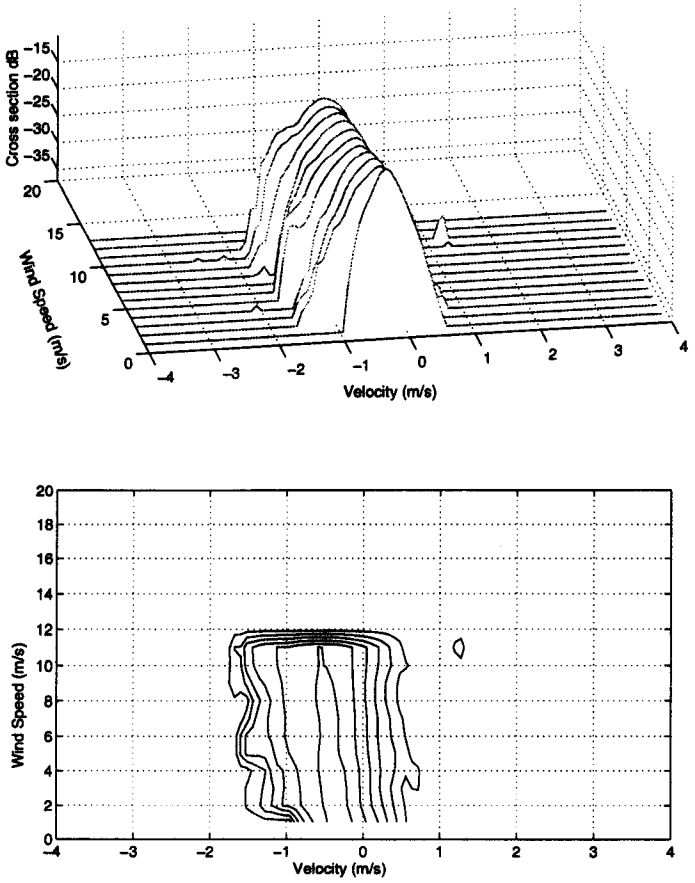

Figure 5.9: Average histograms plotted to show the wind speed evolution of the data. For these measurements frequency is 5 Ghz, H-pol, 40 degrees incidence angle.

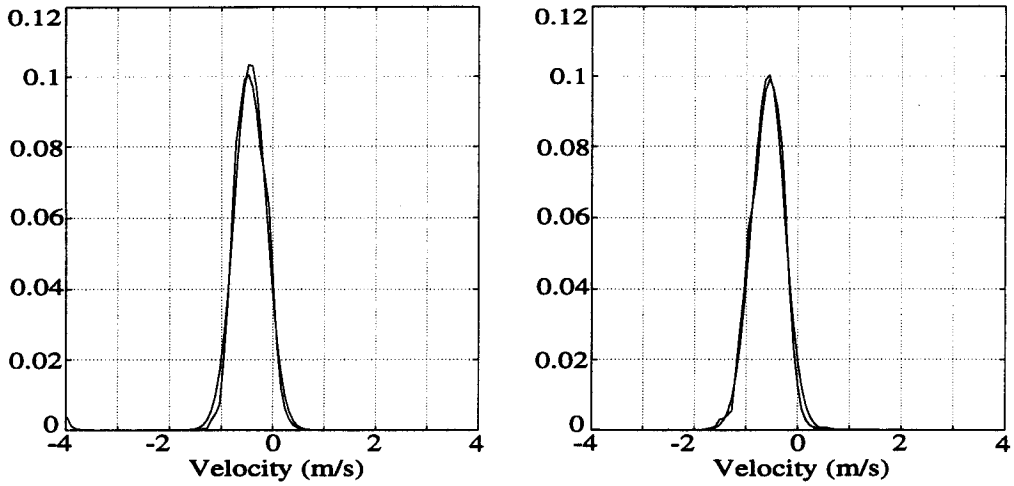

(a) 2 m/s

(b) 5 m/s

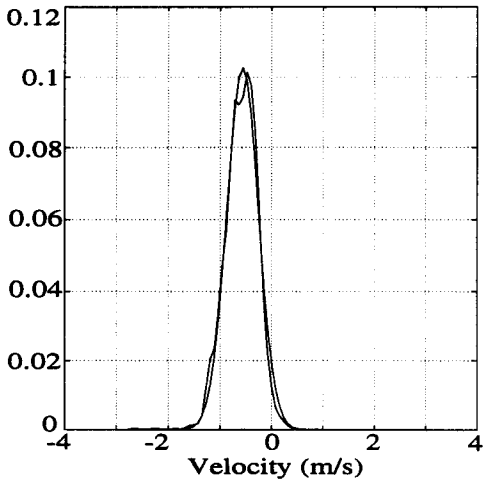

(c) 7 m/s

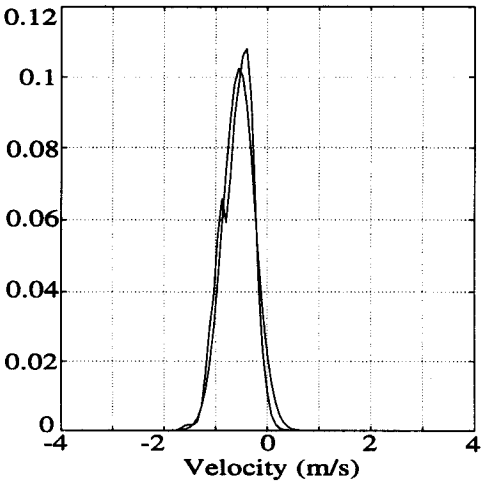

(d) 10 m/s

Figure 5.10: Typical set of Doppler distributions. These measurements are for 10 GHz, H-pol, 50 degrees incidence angle.

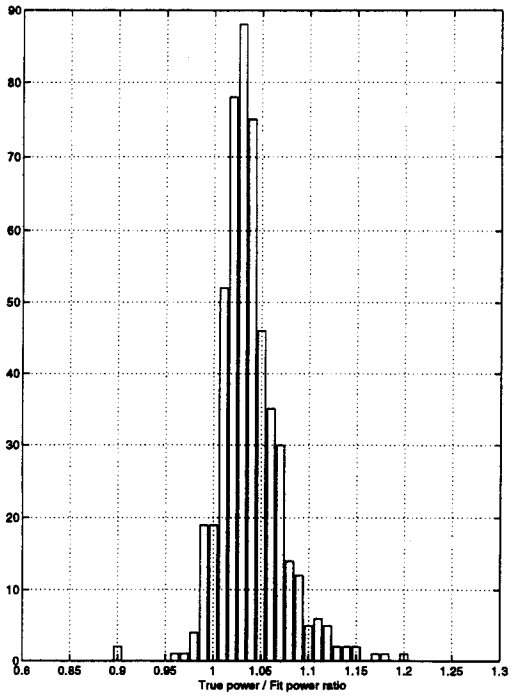

Figure 5.11: This plot shows a histogram of the ratio of the total power to the fitted power in the Doppler distributions for all cases. The average is 1.03 and the standard deviation is 0.07.

Figure 5.12 shows a histogram of the ratio of the mean of the empirical distributions to the fitted distributions for all cases. We can see that the fitted distributions accurately parameterize the power in the Doppler distribution and the mean of the Doppler distributions to within a few percent.

5.4 Comparison with Simulations

The main advantage to performing the simulations are in being able to identify the causes of some of the effects observed in the empirical data because of our knowledge of the properties of the simulation model. With this in mind, this

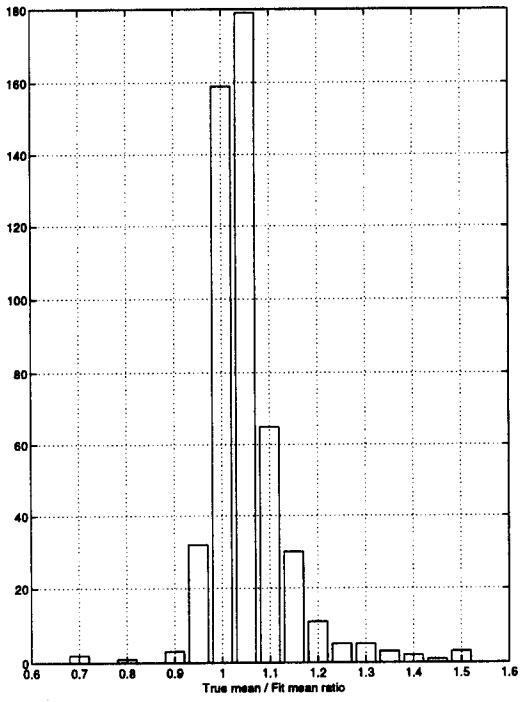

Figure 5.12: This plot shows a histogram of the ratio of the true means to the fitted means for all cases. The average value is 1.05 and the standard deviation is 0.09.

section compares the simulated distributions using the same parameterizations for the simulated data as was used for the empirical data.

5.4.1 Doppler Centroid and Variance

An important statistic of the Doppler spectrum is the Doppler centroid. The Doppler centroid is a measure of the velocity of the surface scatterers in an average sense. It is defined as the first moment of the Doppler spectrum and is given by

$$f_c = \int \nu D(\nu) d\nu \tag{5.7}$$

where $D(\nu)$ is the Doppler spectrum of the radar return and ν is frequency. This centroid frequency can be converted to line of sight (LOS) velocity by noting that

$$\Delta f = \frac{2v}{\lambda} \tag{5.8}$$

where Δf is the Doppler shift, v is the velocity, and λ is the EM wavelength.

The Yscat radar data contains Doppler centroid estimates collected at 10 Hz in 1 minute measurements. The average Doppler centroid (f_d) is calculated using the received power as the weighting function. That is,

$$f_d = \frac{\sum_i f_i p_i}{\sum p_i} \tag{5.9}$$

where the p_i's are the 10 Hz power measurements and the f_i's are the 10 Hz centroid measurements.

The centroid of the Doppler spectrum is a measure of the effective LOS velocity of the surface as seen by the radar. The LOS velocity predicted by the model is easily determined via the simulation and sheds some light on the qualities of the

composite model. Figures 5.13 and 5.14 show data which are typical of the results of the simulation-empirical comparison.

At 20 and 30 degrees incidence the model predicts the Doppler centroid velocities quite well for both V-pol and H-pol. Both the magnitude and the measured wind drift are in quite good agreement between the model and the empirical data. At 40 and 50 degrees incidence the model significantly under-predicts the Doppler centroids at low wind speeds but the difference decreases with increasing wind speed. Correspondingly, the wind drift predicted by the model is slightly high. At 60 degrees incidence the model significantly under predicts the Doppler centroids for all wind speeds by about 50 %. This behavior is typical of all the frequencies under consideration.

This case points out a significant deficiency in the model presented here. Several assumptions have been made which affect the centroid calculation. First of all, the assumption made about the upwind traveling Bragg waves is not well supported by either theoretical or experimental data. Upwind traveling waves will tend to weight the centroid calculation towards zero. Therefore, knowledge of this parameter is essential to predicting the velocity that will be perceived by the radar.

Another simplification of this model is that it assumes linear superposition holds in relating the wave height spectrum to the wave surface. It is a known condition that the waves tend to be more peaked at the top than is explained by linear superposition. This "Stokes" effect is responsible for the breaking of the waves as they become to steep.

Finally, the hydrodynamic modulation of the small wave spectrum has been completely ignored in the model. Hydrodynamic modulation has been proposed

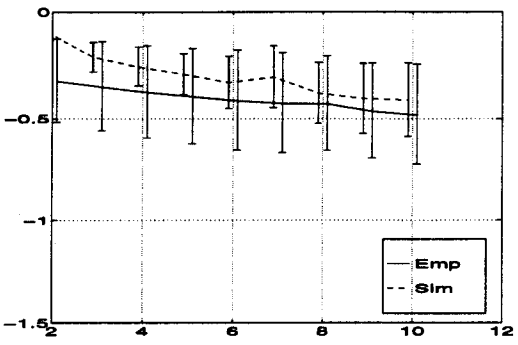

(a) 20 degrees

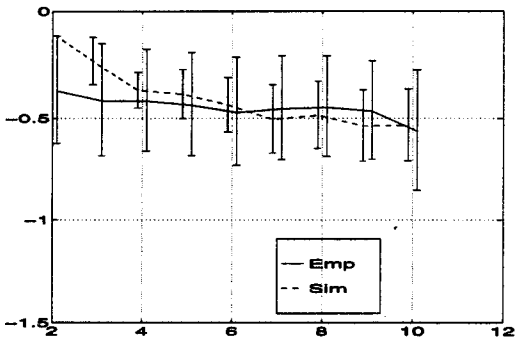

(b) 30 degrees

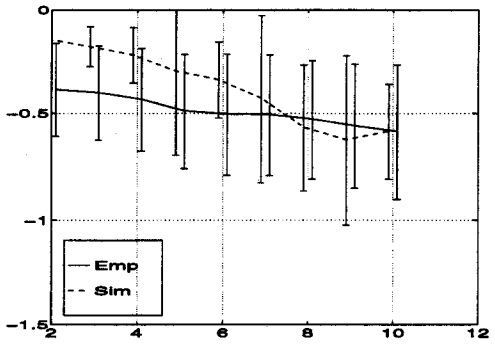

(c) 40 degrees

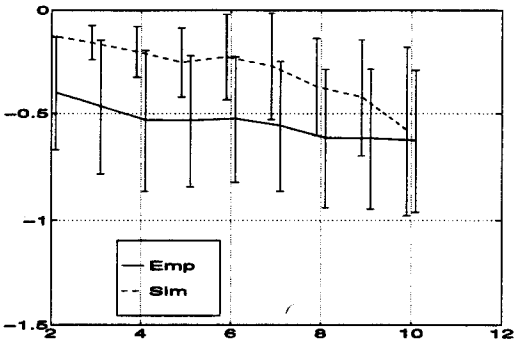

(d) 50 degrees

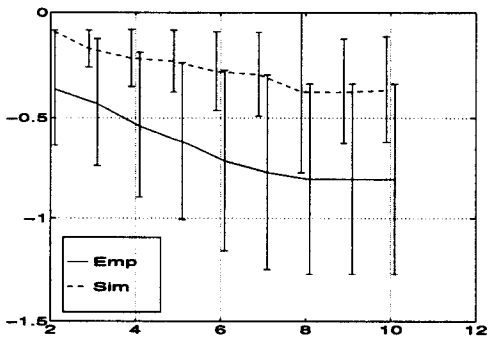

(e) 60 degrees

Figure 5.13: Doppler centroid and variance plots. Velocity simulations compared with empirical results. Error bars denote 1 standard deviation of the centroid distributions. These results show H-pol, 5 Ghz, upwind data.

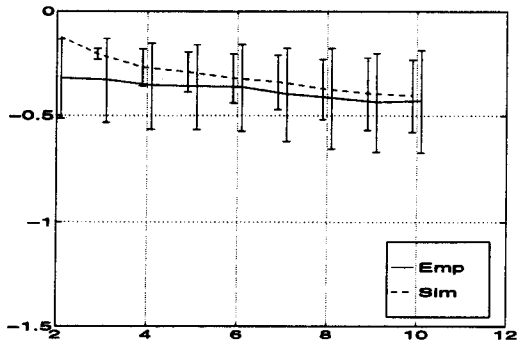

(a) 20 degrees

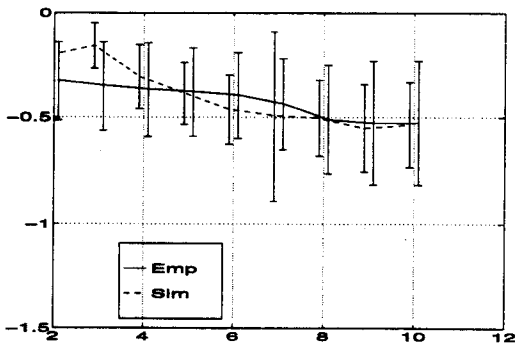

(b) 30 degrees

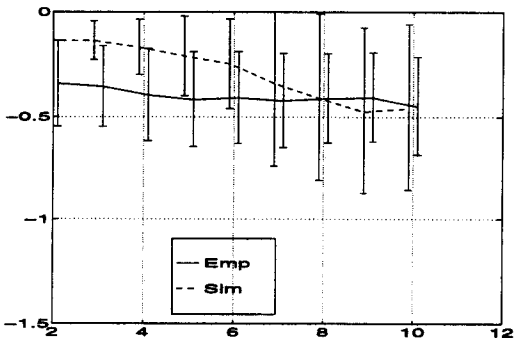

(c) 40 degrees

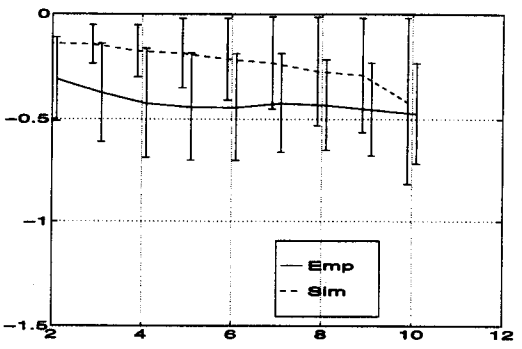

(d) 50 degrees

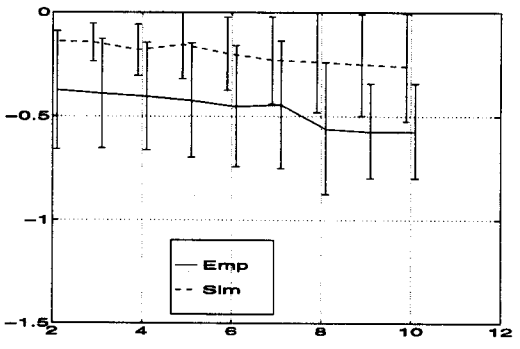

(e) 60 degrees

Figure 5.14: Doppler centroid and variance plots. Velocity simulations compared with empirical results. Error bars denote 1 standard deviation of the centroid distributions. These results show V-pol, 5 GHz, upwind data.

as a part of the composite model by several researchers (Keller et al., 1994; Jeynes, 1989; Durden, 1989; Plant, 1986). The effect is that the underlying wave "stresses" the small Bragg waves as it passes. The effect is a modulation of the amplitude of the Bragg waves which is coherent with the underlying long waves.

The hydrodynamic modulation transfer function (MTF) can be modeled as a periodic fluctuation of the Bragg spectrum. The standard equation for the composite Bragg scattering is given by Eq. (4.6). This equation can be modified to include a MTF by allowing the spectral density to be amplitude modulated by the swell. This is expressed as

$$\sigma_o(x,t) = 16\pi k_m^4 |G_{ii}(\theta)|^2 \Psi(2k_m \sin\theta) M \cos(\Omega t - Kx + \varphi) \tag{5.10}$$

where the M is the magnitude of the modulation, Ω is the long wave frequency and K is the long wave wavenumber. Note that the cross section is now dependent on the relative phase, φ, of the underlying dominant wave.

Adding this to the model allows one to move the peak cross section on the phase of the underlying waves and, hence, change the measured Doppler centroid. By moving the peak Bragg spectral amplitude to a faster portion of the wave, the discrepancy between the model and the empirical data might be explained. Studies of the MTF reveal that the hydrodynamic modulation leads the crest of the wave slightly (Hara and Plant, 1994). This would tend to shift the peak cross section towards the peak of the wave, thus slightly reducing the measured velocity. Therefore, it is unlikely that the MTF would account for this discrepancy. In any case, the current state of knowledge on the hydrodynamic MTF is insufficient to include adequately in the model and it is considered beyond the scope of this dissertation.

The model presented in this dissertation is purposefully simplified in order to aid in recognizing the effect of various scattering mechanisms. Therefore, these other properties of waves, which are likely to have effects on the velocity statistics and which are unmodeled here, are noted and omitted from the model. It is sufficient for the purposes of this model to note that there is no evidence of high speed scatterers in the Doppler centroid data. Although the empirical measurements can be significantly higher than those predicted by the simulation, they are still lower than the predicted velocities of breaking waves or of scattering wedges.

5.4.2 Variance

The variance of the empirical data gives a measure of the range of the velocities of the various scatterers involved in the scattering. The model presented in this chapter suggests that as the mean squared wave slope increases with wind speed, the variance of the Doppler distribution should increase quite strongly; however, as shown in Figure 5.15, the empirical distributions show only a small increase in variance as wind speed increases.

Comparing the simulation variances with the empirical variances immediately reveals that the observed variances are significantly higher than those predicted by the simulation. According to the model, parameters which significantly affect the variance of the Doppler distributions the most are wind speed and fetch. Increasing either fetch or wind speed also increases the wave-height spectrum and, hence, the observed variance. Presumably, the wind speed measured by the anemometers is correct since it is checked between three independent anemometers. Fetch is much more difficult to verify since it varies from 1 to 300 km at the Lake Ontario site. In light of the simplifications already acknowledged in the model, it is sufficient to present an

example of increasing the fetch from 6 to 9 km. Figure 5.16 shows the resulting variances plotted with the empirical data. Prevailing fetch for upwind measurements is between 3 and 6 km (see Fig. 4.2), although longer fetches certainly occur. Therefore, it is not likely that the fetch is the sole reason for the under prediction of the widths of the Doppler distributions. However, Fig. 5.16 illustrates the relative sensitivity of the model to this parameter.

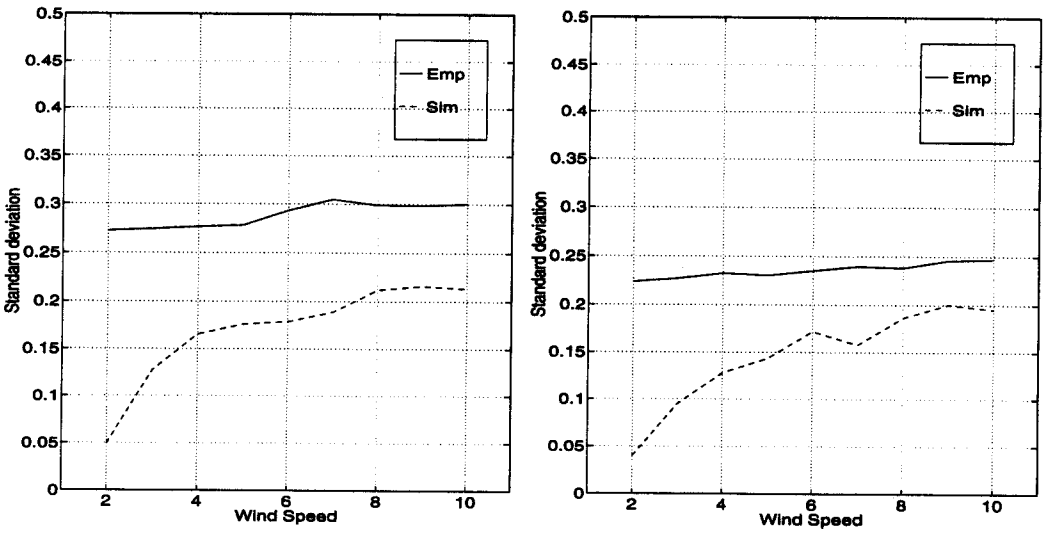

(a) H-pol (b) V-pol

Figure 5.15: Standard deviation of the Doppler distributions averaged over incidence angle and frequency for (a) H-pol and (b) V-pol.

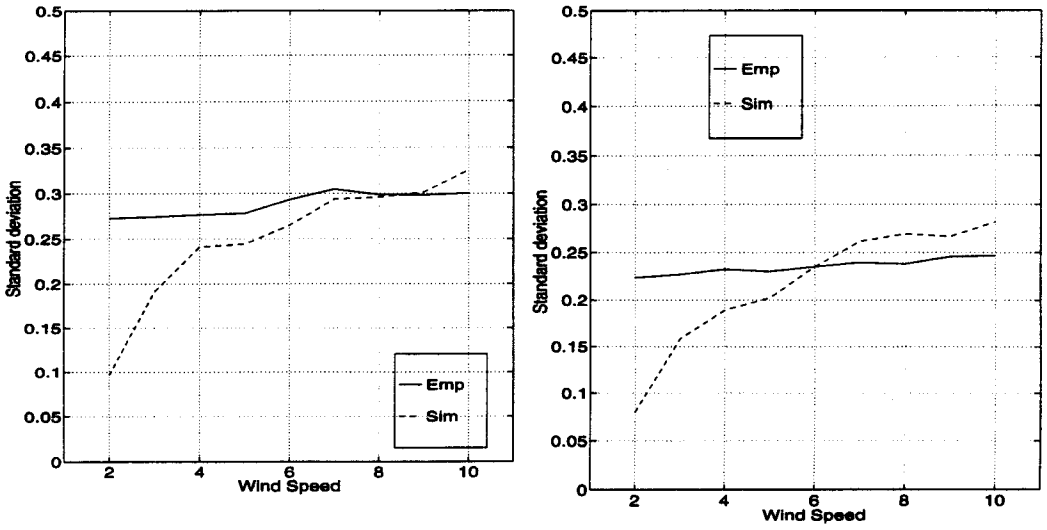

(a) H-pol (b) V-pol

Figure 5.16: Standard deviations of the Doppler distributions with extended fetch. For these simulations, the fetch was 9 km instead of 6km (Note the better fit than that in Fig. 5.15).

At longer fetches the simulation variances also show more wind speed dependence than the empirical data, especially at low to moderate wind speeds. At high wind speeds, however, the wind speed dependence of the simulation data appears to moderate somewhat.

Although not clear in Fig. 5.15, the variance of both the empirical and simulated data seems to be rather small considering the range of velocities seen on a typical sea surface. Looking at the simulation Doppler distributions overlaid with the velocity pdf of the surface, the reasons become clear. The velocity pdf is the normalized histogram of all of the velocity measurements of the surface.

Figure 5.17 shows the Doppler distributions and the velocity pdf together on the same plot. The velocity pdfs show the expected behavior as the range of

observed velocities increases dramatically with wind speed. The Doppler distributions show a much reduced wind speed dependence because the majority of the power is scattered from a relatively narrow portion of the waves.

5.4.3 Average Cross Section Velocity

In addition to the Doppler distributions, the average scatterer cross section can yield useful insights into the composite model. This calculation is closely related to the Doppler distribution. The power of each individual measurement is binned according to its estimated velocity. The total power in each bin is totaled up and averaged according to how many measurements were collected at that velocity.

This measurement allows finer analysis of the model because it allows us to see where the model fails and where it is valid as a function of velocity. In general, the agreement between the model and the empirical data is quite remarkable. Aside from the obvious offset between the peaks, the slope of the slow speed dependence, and the general shape of the velocity profile is in very good agreement for a large portion of the measurements. This supports the idea that the general composite model of Bragg scattering is in fact valid over much of the range observed by the Yscat radar. Figure 5.18 shows some typical comparisons of the simulated data and the empirical data. The plots have been normalized so that both distributions have a peak value of 0 dB.

There are some notable exceptions to the general agreement in the shape of the average cross sections. At 60 degrees incidence angle, the upwind, V-pol empirical distributions are much narrower than the predicted distributions. This is also visible in the 50 degree data, but to much less extent. Figure 5.19 shows an example of this effect. Through subjective examination, other cases which strongly disagree with the

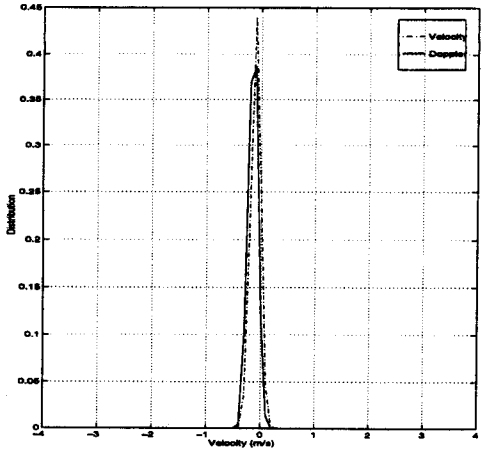

(a) 3 m/s

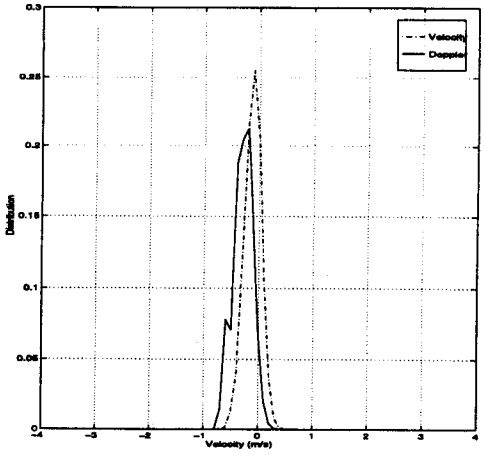

(b) 5 m/s

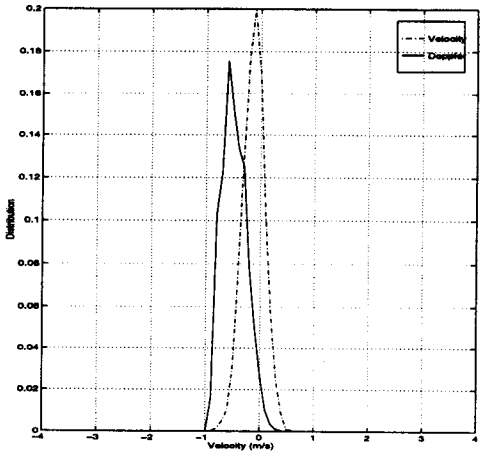

(c) 7 m/s

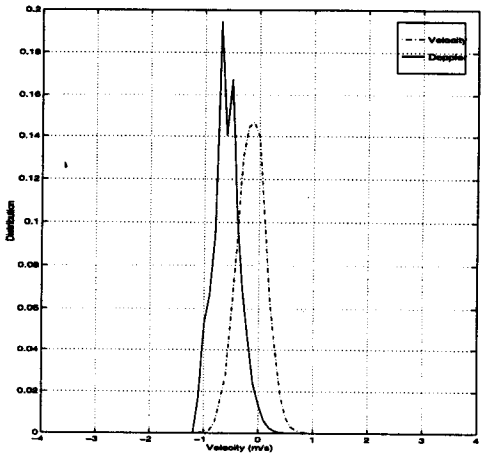

(d) 9 m/s

Figure 5.17: Doppler distributions and velocity profiles for 10 GHz, 40 degrees incidence angle, H-pol simulations.

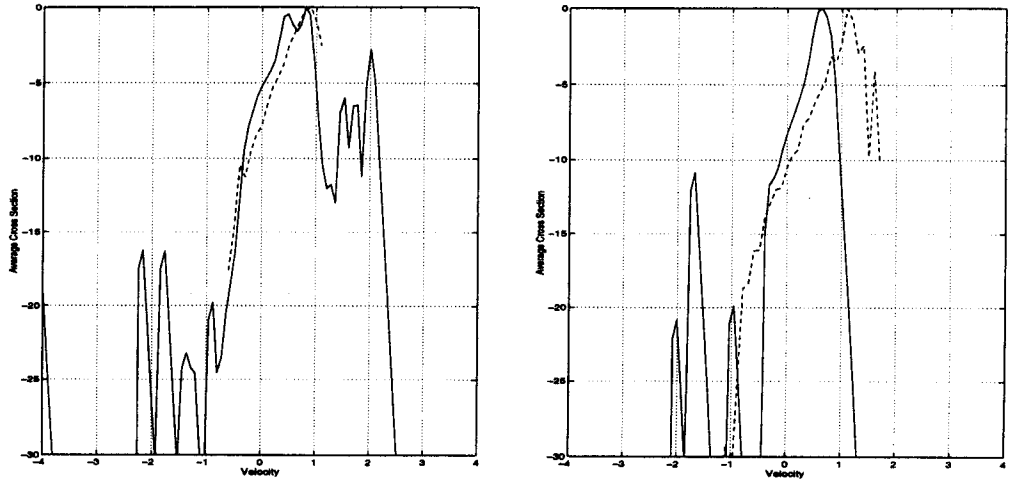

(a) 3 m/s

(b) 5 m/s

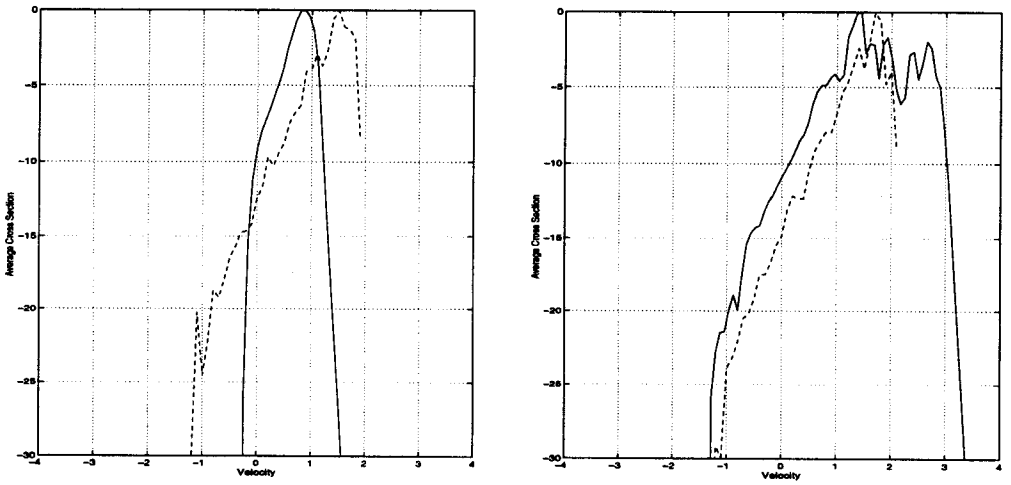

(c) 7 m/s

(d) 9 m/s

Figure 5.18: Comparison of velocity modulation of empirical and simulation data. These measurements are for 14 GHz, 50 degrees incidence angle, H-pol simulation (dotted line) and empirical data (solid line).

	20°	30°	40°	50°	60°
2 GHz					
3 GHz					V
5 GHz					V
10 GHz			V	V	V
14 GHz			V	V	V

Table 5.1: Results of the comparison of the average cross section predictions of the simulation to the empirical data. Upwind data. Letter designations denote which polarization, if any, exhibited the disagreement between simulation and empirical data.

	20°	30°	40°	50°	60°
2 GHz					V
3 GHz				V/H	V/H
5 GHz			V	V/H	V/H
10 GHz			V	V/H	V/H
14 GHz				V/H	V/H

Table 5.2: Results of the comparison of the average cross section predictions of the simulation to the empirical data. Downwind data.

simulation data can be identified. This type of disagreement is also apparent in the downwind data for some of the V-pol 40, 50, and 60 degree incidence angle data and some of the 50 and 60 degree incidence angle H-pol data. This is summarized in Tables 5.1 and 5.2.

5.4.4 Polarization Velocity Ratio

The composite model suggests that the scattering mechanism for both V-pol and H-pol is the same. Because of this, one might assume that the velocities measured by the radar would be the same for each polarization. However, one must recall that in the previous section, it was shown the majority of the power is scattered from a rather narrow region of the wave velocity profile. Because this region may be different between V-pol and H-pol, there may be some velocity difference between

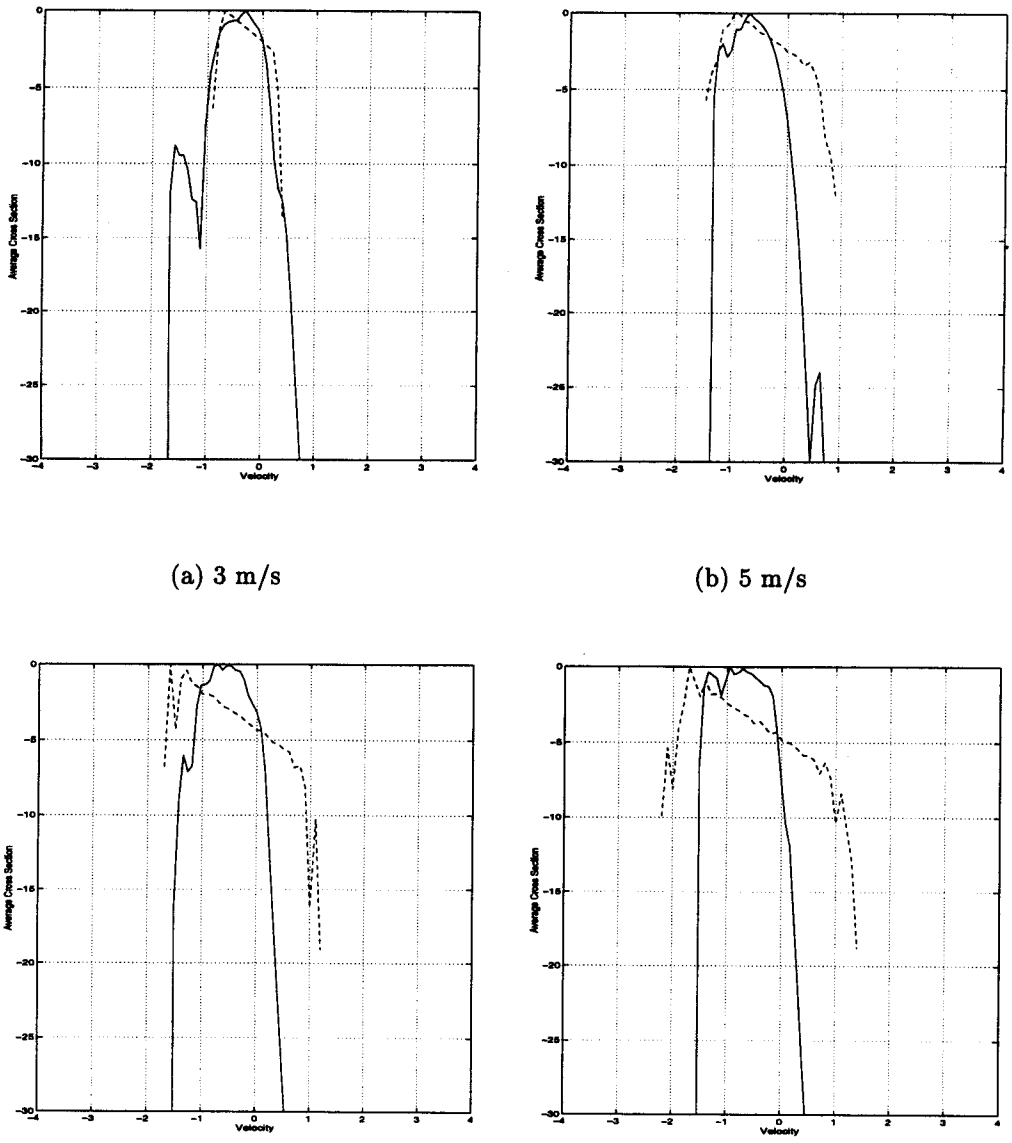

(a) 3 m/s

(b) 5 m/s

(c) 7 m/s

(d) 9 m/s

Figure 5.19: Comparison of velocity modulation of empirical and simulation data for upwind, V-pol data. Note that the scattering in this case is coming from a much narrower distribution than predicted by the model. These measurements are for 14 GHz, 50 degrees incidence angle, H-pol simulation (dotted line) and empirical data (solid line).

the polarizations. Figure 5.20 show the average velocities of H-pol plotted against the velocities of V-pol for increasing incidence angle.

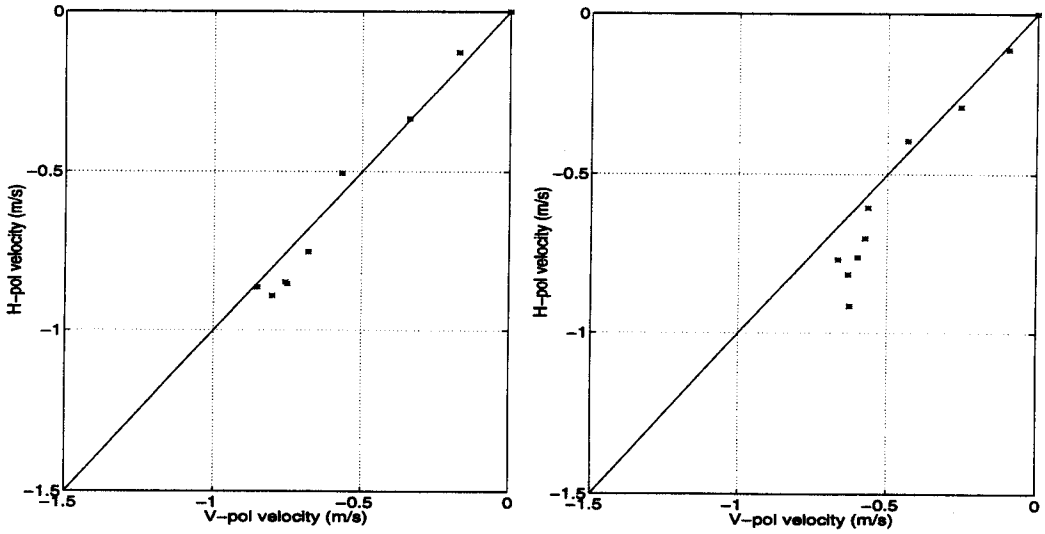

(a) 30 degrees

(b) 40 degrees

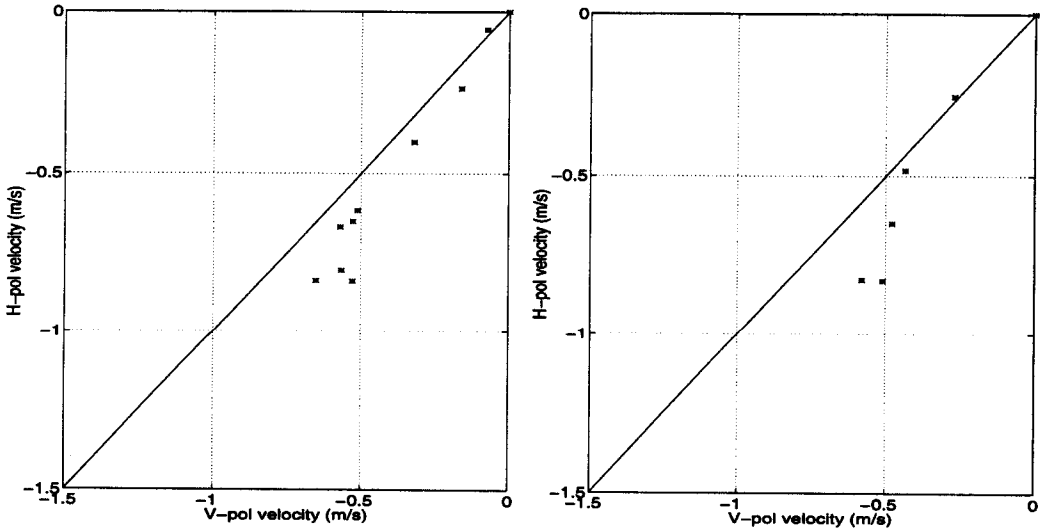

(c) 50 degrees

(d) 60 degrees

Figure 5.20: H-pol velocity plotted verses V-pol for 5 Ghz, upwind empirical data.

The unusual fact that the radar measures different velocities for the same surface at different polarizations may be interpreted as an indication of different scattering mechanisms between H-pol and V-pol. However, as Fig. 5.20 illustrates, this is explained by the composite model. Looking at the simulation, we can see that this effect is due to the differences in the slope verses cross section relationship.

The results in this section seem to indicate that the composite scattering model accounts for the majority of the characteristics of the velocity statistics. Based on the theoretical velocity of breaking waves, one would expect any contributions from these events to increase the width of the Doppler distributions. However, if these events occur very infrequently, it may not show up in the average Doppler histogram.

Perhaps a measure of width is available that would be more sensitive to detecting an increase in low probability but high velocity scatterers. A first thought is to use a simple max-min detector, i. e., simple taking the measurement with the highest and lowest velocity in each 1 minute record. Unfortunately this is a very noisy sample since a single unusual event can dominate the entire file. Because of this a robust regression technique is used to try to eliminate outlying points.

Figure 5.22 shows a typical set of maximum measurements. Each point corresponds to the 1/10 second sample in each 1 minute measurement that has the highest Doppler shift. It is interesting to note that the data is noisiest at low wind speeds. This could be an indication of the instability of the wind direction and the relatively low radar cross section typically associated with low wind speeds. More important, though, is the lack of high velocity events at high wind speeds. This

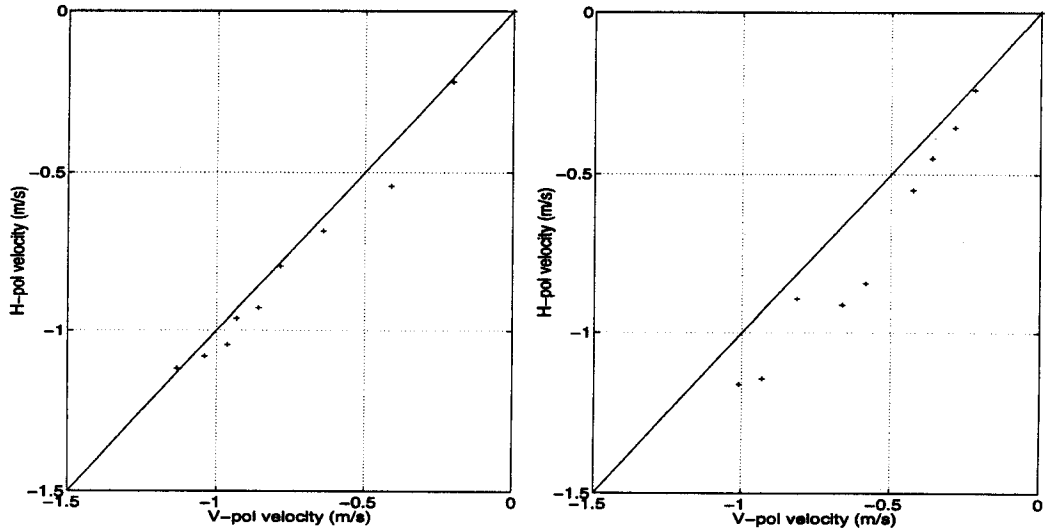

(a) 30 degrees

(b) 40 degrees

(c) 50 degrees

(d) 60 degrees

Figure 5.21: H-pol velocity plotted verses V-pol for 5 Ghz, upwind simulated data.

indicates that under the conditions when it is most likely, high velocity events are rare.

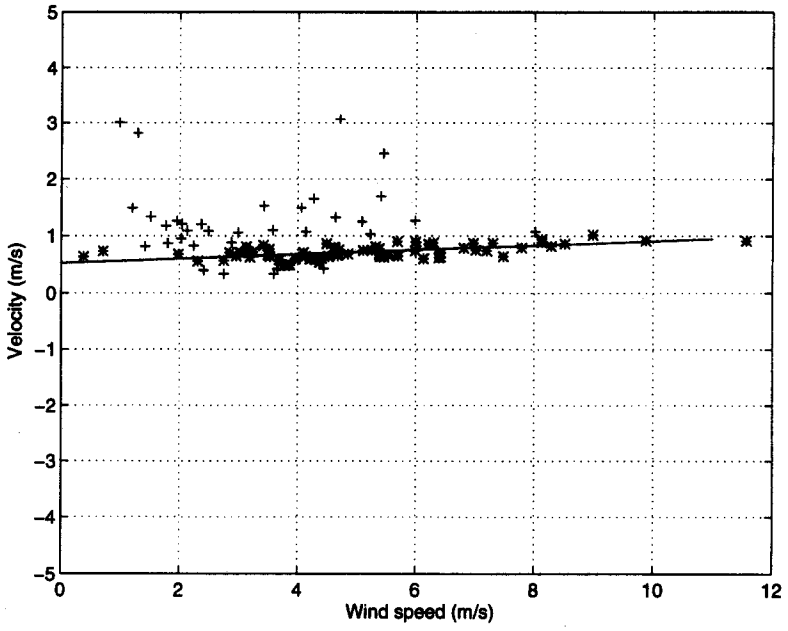

Figure 5.22: This plot shows how the variance processing described in the text emphasises tight groupings of data and ignores large scattered data.

Figure 5.23 shows the resulting robust regression fits to the data. The 30 degree incidence data shows some anomalous behavior probably due to the noisiness of the measurement. The rest of the data appears to be rather tightly grouped with the exception of the 60 degree incidence data which consistently shows higher maximum velocity at mid to high wind speeds. The results are similar for V-pol data. We see

that the high wind speed, high frequency data shows some signs of small contributions by high velocity scatterers, an observation consistent with the results of the previous section and theory. Combining this result with the 60 degree incidence angle power distributions in the last chapter, indicates that these high velocity scatterers might be associated with wedge scattering.

5.5 Conclusions

The velocity statistics predicted by the composite model were determined using the modeling and simulation techniques described in the previous chapter. It was shown that the velocities predicted by the composite model and those predicted for breaking waves and wedge scatterers are significantly different.

The velocity statistics of the empirical data were parameterized by fitting normal distributions to the Doppler distributions. These normal fits were shown to accurately characterize both the variance and the mean of the Doppler distributions. The simulation data was parameterized in the same way and compared to the empirical data. It was found that for 20, 30, and 40 degree incidence angle measurements, the simulation accurately predicted the observed Doppler centroids. At 50 and 60 degrees incidence angle the simulation significantly under-estimated the Doppler centroids. It was shown that this might be due to the hydrodynamic MTF.

The shape and slope of the average cross section profiles were compared to those derived in the simulations and found to agree quite well in both shape and width for most measurements. At high incidence angles, the empirical data show significantly narrower spread in observed velocities than were predicted by the simulation.

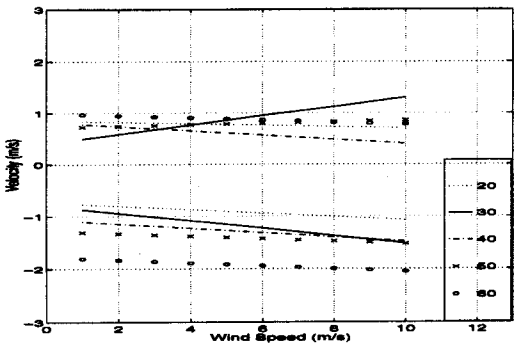

(a) 2 Ghz

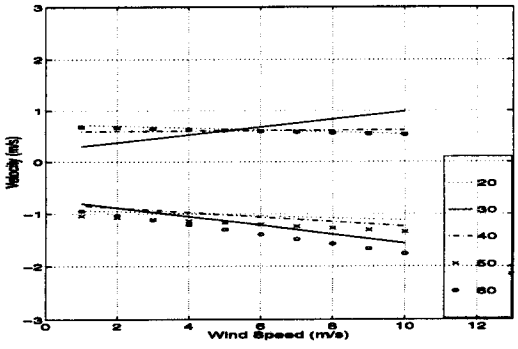

(b) 3 Ghz

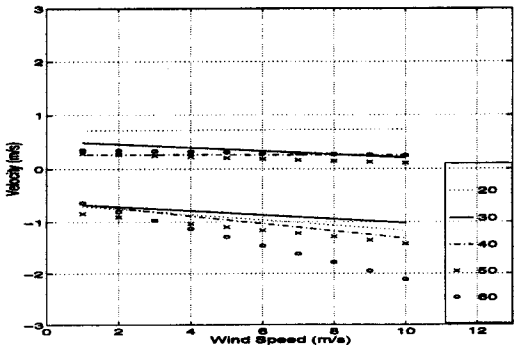

(c) 5 Ghz

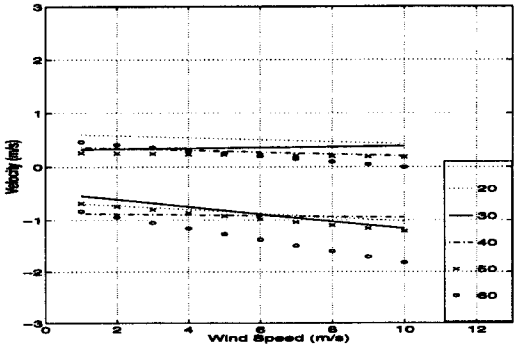

(d) 10 Ghz

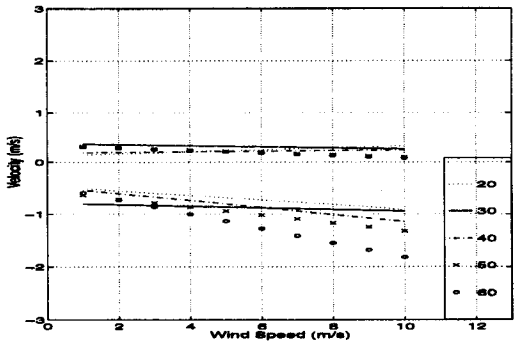

(e) 14 Ghz

Figure 5.23: Minimum and maximum velocities observed for different frequencies. All data is H-pol, upwind.

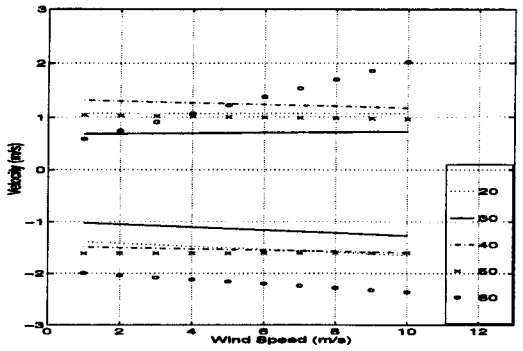

(a) 2 Ghz

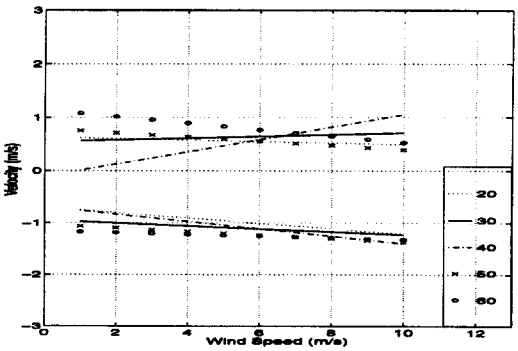

(b) 3 Ghz

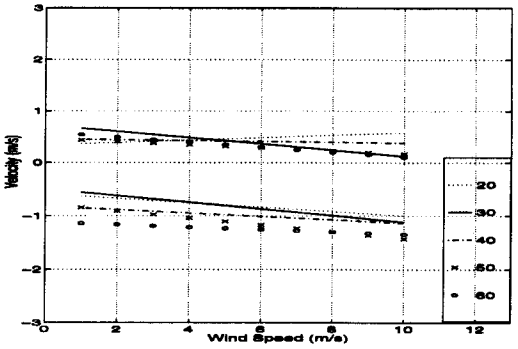

(c) 5 Ghz

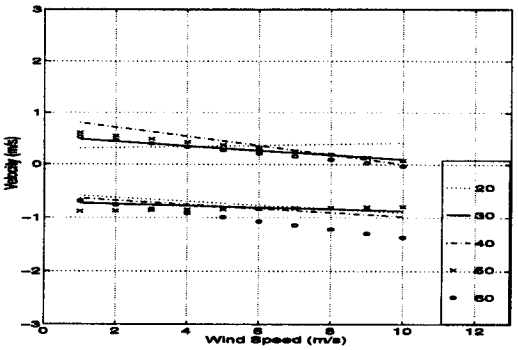

(d) 10 Ghz

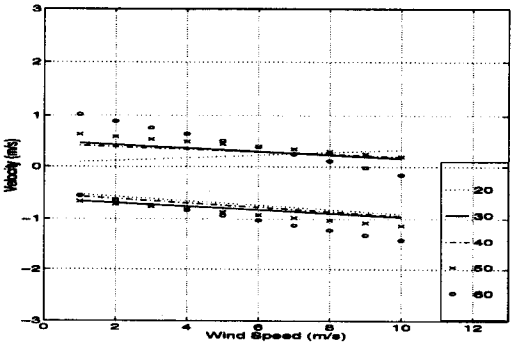

(e) 14 Ghz

Figure 5.24: Minimum and maximum velocities observed for different frequencies. All data is V-pol, upwind.

It was shown that the composite model predicts that the radar system will measure a slight difference in the Doppler centroids of the H-pol and V-pol data. This difference was also found in the empirical data, strengthening confidence of the simulation to predict even the finer points of the velocity statistics. In particular, no evidence for a significant contribution from fast scatterers is found for incidence angles less than 60 degrees. The minimum and maximum velocity statistics showed that the 60 degree incidence angle data definitely shows higher velocities than the rest of the data. This is possibly due to an increasing importance of additional fast scatterers.

Chapter 6

SUMMARY AND CONCLUSIONS

This purpose of this dissertation is to present a study of the statistics of the radar return scattered from the sea surface. The statistics of the sea scattered radar return are intimately connected to the scattering mechanisms involved in the radar-surface interaction. Statistics measured during the Yscat94 experiment were compared to predicted statistics obtained using a simple model and simulation technique to determine if the current composite model is in qualitative agreement with the observed statistics and to determine if evidence of additional scatterers contributing to the radar cross section is visible in the data.

The data used to calculate these statistics were gathered by the Yscat radar system in during an extended deployment on Lake Ontario conducted from May to November, 1994. The experiment location was the Canada Centre for Inland Waters (CCIW) research tower located 1 km east of Hamilton, Ontario, Canada. The water depth is about 12 m at this location. The prevailing winds are westerly and generally produce fetches of 1-9 km. Wave heights during the experiment were generally less than 0.5 m rms wave height except under unusual wind conditions.

The radar measurements were made using the Yscat radar, a coherent, CW, frequency agile scatterometer which operated at center frequencies of 2, 3.05, 5.3, 10.02, and 14 GHz. Transmit power for this experiment was approximately 3 dBm. The radar transmitted either V- or H-pol and received both like and cross polarization returns. The return signals were split into in-phase and quadrature signals, mixed

down to baseband, and digitally sampled at 2 kHz per channel. The resulting data was pre-processed to compute Doppler centroid, bandwidth, and average power at 10 Hz and stored on 4 mm tape.

The incidence angles of the measurements were varied from 20 to 60 degrees by the AZ-EL positioning system. The azimuth angle relative to the wind direction was varied both by moving the radar relative to the wind, and allowing the wind to vary direction while holding the radar still. Environmental data were collected by two anemometers, a rain gauge, a bi-vane anemometer, and a wave gauge. Approximately 6 months worth of data were collected and edited to remove rain contaminated data, data collected during equipment failures, and data considered ruined for other reasons.

The model and the associated simulations were derived from previously published results for the Bragg coefficients, small perturbation theory, wave slope statistics, and wave height spectra. These were combined to show that for small incidence angle deviations and a Gaussian slope distribution, the predicted power distribution should be approximately log-normal. A simulation technique was presented which utilized the Donelan wave height spectrum to model the surface waves of the lake. The slope parameter needed for the composite model application was defined to be the linear fit of a 2/3 m surface composed of wavelengths 1 m and longer. This was shown to give a good estimate of the true slopes by finding that the coefficient of correlation (R^2) was above 0.8 for wind speeds above 3 m/s. The wave slopes of the Donelan spectrum were shown to produce an approximately normal slope distribution, which validates the use of this distribution in the model. The simulations also showed that the conditions when this model holds are only true for lower wind speeds and moderate incidence angles.

The empirical data were fit to both Weibull and log-normal distributions and were found to fit the log-normal much better with approximately a 10 dB advantage in the L2 error over the Weibull. The log-normal fit accounted for 98 % of the power in the empirical distribution with a standard deviation of 0.18 in the ratio of *true power/fit power*. Based on this result, the parameters of the log-normal distribution, the "log-variance" and the "log-mean" were used to parameterize the empirical distributions.

The simulation data were subjected to the same processing as the empirical data to allow a qualitative comparison of the simulated distributions to the true distributions. The variance of the simulated distributions showed quite a bit more wind speed dependence than the empirical data. A postulated cause is a decrease in the coherence of the surface which results in averaging over more independent areas at higher wind speeds. It was shown by example that a decrease in the correlation length by 1/2 would account for the decreased wind speed dependence.

The shape of the simulated and empirical distributions were compared and showed that the model presented in this dissertation does not adequately explain the specular contribution to the total radar cross section, which is important at 20 degrees incidence, and visible at 30 degrees. At moderate incidence angles (40 and 50 degrees), the model accurately predicted both the incidence angle dependence of the variance and the polarization dependence of the power distributions. At 60 degrees, however, the empirical distributions show signs of additional scattering mechanisms, possibly wedge scatterers, which cause it to deviate from the model shape. These results emphasize the transitional nature of the scattering at 20 and 60 degrees incidence.

The model and simulation were then used to predict the velocity statistics of the radar return. The velocity statistics were extracted from the scattered signal via the Doppler shift of the radar return. It was shown theoretically that the Bragg type scatterers and the proposed additional scatterers (wedge scatterers and breaking waves) would have very different velocity characteristics.

The Doppler distributions of the empirical data were calculated by binning the power according to the measurement estimated velocity. It was found that these distributions were well approximated by Gaussian distributions. When the Gaussian that minimized the L2 error between the empirical distribution and the fit was compared to the true distributions, the Gaussian was found to account for an average of 97 % of the total power in the distribution with a standard deviation of 0.07 in the ratio of *true power/fit power*. The Gaussian fit under predicted the mean on average, but this value was only 5 % and had a standard deviation of 0.09 in the ratio of true mean to fitted mean. Based on this it was determined that using the Gaussian fits to parameterize the Doppler distributions was justified.

The simulation data was found to predict the 20 - 40 degree incidence angle centroids fairly well, but under-predicted the 50 and 60 degree incidence angle data significantly. The source of this error is not apparent but is likely due to the simplicity of the model (which does not include hydrodynamic modulation or other higher order effects in order aid in recognizing the effects of various scattering mechanisms). The variance of the simulated Doppler distributions is found to be significantly less than the empirical distributions for fetches comparable to those encountered during the experiment.

Better agreement with the simulation was found when the average velocity cross sections of the model were compared to the empirical data. These distributions were found to agree quite well in shape and slope, although all seemed to be slightly offset towards higher velocities. The agreement in shape and slope, however, supports the simple model in principle. The conditions for which the simulated data did not support the empirical data were at high incidence angle, upwind, V-pol data and H- and V-pol downwind data.

The polarization velocity ratios showed that the simple model even predicts some of the finer velocity statistics for certain cases. Finally, the minimum-maximum velocity statistics showed that all of the frequency and incidence angle ranges observed the same velocity of scatterers, in an average sense, and so all observed the same scatterers. Exceptions to this observation are the 60 degree incidence angle data for all frequencies which showed higher maximum velocities. This agrees with the results of the previous section which indicated that high speed wedge scattering may be becoming significant at this incidence angle.

In conclusion this research has shown that the composite model correctly predicts observed characteristics of the sea scattered radar return at moderate incidence angles. Even without resorting to the more complicated models available, which are derived to explain the difference between the observed and predicted mean radar cross section, the simple model presented here predicts the qualitative behavior of the power and velocity distribution of the sea scattered radar return. For mid range incidence angles, no evidence is seen for significant contributions of additional scatterers. At the extremes of the incidence angle range (20 and 60 degrees), the empirical distributions begin diverge significantly from the composite model. The implication

of this research is that the postulated "missing" scatterers (scattering mechanisms not included in the current composite model) do not contribute significantly to the average radar cross section the wind roughened water surface.

Further Research

There are several directions for future work that are indicate by this research. Future experiments to analyze detect additional scatterers should concentrate on the transition region above 50 degrees incidence angle where this study shows indications of additional scatterers. Further insight may be gathered by performing a real-time analysis of the Doppler spectrum of the radar return rather than the centroid method used here. Clearly, this would allow for a more detailed analysis of the distributions of the radar return and contributions from other mechanisms. Since it appears that contributions from non-Bragg type scatterers are small, this technique would prevent them from being washed out by the centroid estimation technique. However, it is also clear that collecting a comparable amount of data in this manner will be very costly from a data storage point of view. Also, a similar analysis of data collected in an open ocean setting would aid in understanding the effects of very long waves.

Further research also needs to be done on understanding the small wavelength spectrum and its dependence on environmental conditions such as temperature and atmospheric stability. Since it appears that Bragg scattering accounts for almost all of the observed scatter, the reason for the failure of the physically based model functions must be due to an misunderstanding of the hydro-dynamical processes which occur in generating the wave field under stress from the wind. In addition, the simple model presented here may be improved by the inclusion of more complicated

effects such as hydrodynamic modulation. Therefore, studies of the hydrodynamical modulation of the small wave spectrum are necessary. Such research will almost certainly depend on emerging wave spectra measurement techniques such as laser slope gauges and optical techniques to provide *in situ* measurements of the small wavelength portion of the spectrum.

BIBLIOGRAPHY

Banner, M. L. and O. M. Phillips, "On the Incipient Breaking of Small Scale Waves." *Journal of Fluid Mechanics*, vol. 65, no. 4, pp. 647–656, 1974.

Chen, K. S., A. K. Fung, and F. Amar, "An Emprical Bispectrum Model for Sea Surface Scattering." *IEEE Journal of Geoscience and Remote Sensing*, vol. 31, no. 4, pp. 830–834, 1993.

Collyer, R. S., *Wind Speed Dependence of the Normalized Radar Cross Section*. Master's thesis, Brigham Young University, Provo, UT, 1994.

Colton, M. C., *Dependence of Radar Backscatter on the Energetics of the Air Sea Interface*. Dissertation, Naval Postgraduate School, Monterey, CA, 1989.

Ding, L. and D. M. Farmer, "Observations of Breaking Surface Wave Statistics." *Journal of Physical Oceanography*, vol. 24, pp. 1368–1387, 1994.

Donelan, M. A., J. Hamilton, and W. H. Hui, "Directional Spectra of Wind-Generated Waves." *Philosophical Transactions of the Royal Society of London*, vol. 315, no. A, pp. 509–562, 1985.

Donelan, M. A. and W. J. Pierson, "Radar Scattering and Equilibrium Ranges in Wind Generated Waves with Application to Scatterometry." *IEEE Journal of Geoscience and Remote Sensing*, vol. 92, no. C5, pp. 4971–5029, 1987.

Doviak, R. J. and D. S. Zrnic, *Doppler Radar and Weather Observations*. Academic Press, 1984.

Durden, S. L., "Microwave Scattering From the Oceans Surface." Internal Report.

Durden, S. L. and J. F. Vesecky, "A Physical Radar Cross-Section Model for a Wind-Driven Sea with Swell." *IEEE Journal of Oceanic Engineering*, vol. 10, no. 4, pp. 445–452, 1985.

Gotwols, B. L. and D. R. Thompson, "Ocean Microwave Backscatter Distributions." *Journal of Geophysical Research*, vol. c5, no. 99, pp. 9741–9750, 1994.

Hara, T. and W. J. Plant, "Hydrodynamic Modulation of Short Wind-Wave Spectra by Long Waves and Its Measurement Using Microwave Backscatter." *jgr*, vol. 99, no. C5, pp. 9767–9784, 1994.

Hasselmann, K. R., R. K. Raney, W. J. Plant, W. Alpers, R. A. Shuchman, D. R. L. C. L. Rufenach, and M. J. Tucker, "Theory of SAR Ocean Wave Imaging." *Journal of Geophysical Research*, vol. 90, pp. 4659–4686, 1985.

Jakeman, E. and P. N. Pusey, "A Model for Non-Rayleigh Sea Echo." *IEEE Transactions on Antennas and Propagation*, vol. AP-24, pp. 806–814, 1976.

Jessup, A. T., *Detection and Characterization of Deep Water Wave Breaking Using Moderate Incidence Angle Microwave Backscatter from the Sea Surface*. Ph.D. thesis, Massachusetts Institute of Technology, Cambridge, MA, 1990.

Jessup, A. T., W. C. Keller, and W. K. Melville, "Measurements of Sea Spikes in Microwave Backscatter at Moderate Incidence." *IEEE Journal of Geoscience and Remote Sensing*, vol. 95, no. C6, pp. 9679–9688, 1990.

Jeynes, P. L. C., "Limitations of the Two-Scale Theory for Microwave Backscatter From the Ocean." In G. Komen and W. A. Oost, eds., *Radar Scattering From Modulated Wind Waves*, pp. 41–47, Kluwer Acedemic Publishers, 1989.

Keller, J. B., "Geometrical Theory of Diffraction." *The Optical Society of America*, vol. 52, no. 2, pp. 116–130, 1962.

Keller, W. C., W. J. Plant, R. A. Petitt, and E. A. Terray, "Microwave Backscatter From the Sea: Modulation of Recieved Power and Doppler Bandwidth by Long Waves." *Journal of Geophysical Research*, vol. 99, no. C5, pp. 9751–9766, 1994.

Long, D. G., "Current Progress in KU Band Model Functions." NSCAT Science Team Report.

Longuet-Higgins, M. S. and J. S. Turner, "An Entraining Plume Model of a spilling Breaker." *Journal of Fluid Mechanics*, vol. 12, no. 63, pp. 1–20, 1974.

Lyzenga, D. R., A. L. Maffet, and R. A. Schuman, "The Contribution of Wedge Scattering to the Radar Cross Section of the Ocean Surface." *IEEE Transactions on Geoscience and Remote Sensing*, vol. GE-21, no. 4, pp. 502–505, 1983.

Melville, W. K., "Air Entrainment and Dissipation in Breaking Waves." *Nature*, vol. 351, no. 72, pp. 469–472, 1991.

Papoulis, A., *Probability, Random Variables, and Stochastic Processes*. McGraw–Hill, 3rd edn., 1991.

Phillips, O. M., *The Dynamics of the Upper Ocean*. Cambridge University Press, 2nd edn., 1977.

Phillips, O. M., "Spectral and Statistical Properties of the Equilibrium Range in Wind Generated Gravity Waves." *Journal of Fluid Mechanics*, vol. 156, pp. 505–531, 1985.

Plant, W. J., "A Relationship Between Wind Stress and Wave Slope." *Journal of Geophysical Research*, vol. 87, no. C3, pp. 1961–1967, 1982.

Plant, W. J., "A Two Scale Model of Short Wind-Generated Waves and Scatterometery." *IEEE Journal of Geoscience and Remote Sensing*, vol. 91, no. 9, pp. 10735–10749, 1986.

Plant, W. J. and J. W. Keller, "Phase Speeds of Upwind and Downwind Traveling Short Gravity Waves." *Journal of Geophysical Research*, vol. 85, no. C6, pp. 3304–3310, 1980.

Plant, W. J. and W. C. Keller, "Parameteric Dependance of Ocean Wave-Radar Modulation Transfer Functions." *IEEE Journal of Geoscience and Remote Sensing*, vol. 88, no. C14, pp. 9747–9756, 1983.

Plant, W. J. and W. C. Keller, "Evidence of Bragg Scattering in Microwave Doppler Spectra of Sea Return." *Journal of Geophysical Research*, vol. 95, no. C9, pp. 16299–16310, 1990.

Plant, W. J., E. A. Terray, and J. R. A. Petit, "The Dependance of Microwave Backscatter from the Sea on Illuminated Area: Correlation Times and Lengths." *Journal of Geophysical Research*, vol. 99, no. C5, pp. 9705–9723, 1994.

Proakis, J. G., C. M. Rader, F. Ling, and C. L. Nikias, *Advanced Digital Signal Processing*. Macmillan, New York, 1992.

Smith, H. and H. H. Jensen, *Transport Phenomena*. Oxford Science Publications, Oxford, 1989.

Snyder, R. L. and R. M. Kennedy, "On the Formation of Whitecaps by a Threshold Mechanism." *Journal of Physical Oceanography*, vol. 13, pp. 1482–1518, 1983.

Trizna, D. B., "Statistics of Low Grazing Angle Radar Sea Scatter for Moderate and Fully Developed Ocean Waves." *IEEE Transactions on Antennas and Propagation*, vol. 39, no. 12, pp. 1681–1690, 1991.

Trunk, G. V., "Radar Properties of Non-Rayleigh Sea Clutter." *IEEE Transactions on Aerospace and Electronic Systems*, vol. AES-8, no. 2, pp. 196–204, 1972.

Ulaby, F. T., *Microwave Remote Sensing*, vol. 2. Artech House, 1983.

Wright, J. W., "Backscattering from capillary waves with application to sea clutter." *IEEE Transactions on Antennas and Propagation*, vol. 14, no. 6, pp. 749–754, 1966.